OXIDES ON SEMICONDUCTORS FOR NOVEL DEVICE APPLICATIONS

by

Javad Rezanezhad Gatabi

A dissertation submitted to the Graduate Council of

Texas State University in partial fulfillment

of the requirements for the degree of

Doctor of Philosophy

with a Major in Materials Science, Engineering, and Commercialization

May 2016

Committee Members:

Ravi Droopad, Chair

Wilhelmus J. Geerts

Clois E Powell

David Irvin

Yihong Chen

FAIR USE AND AUTHOR'S PERMISSION STATEMENT

Fair Use

Duplication Permission

For dad and mom

ACKNOWLEDGEMENTS

The work reported in this dissertation was supported by the Air Force Office of Scientific Research under Grant # FA9550-10-1-0133 and the Graduate College, Doctoral Research Support Fellowship. In addition, I would like to thank the College of Science and MSEC program for financial support to attend MRS meeting.

A special thanks to my advisor Dr. Ravi Droopad, who provided me with the opportunity to work in his research group and for his encouragement during past three years. I would also like to thank my committee members, Dr. Powell, Dr. Geerts, Dr. Chen, and Dr. Irvin for their wonderful advice.

The TEM measurements and analysis reported in this dissertation were carried out by Dr. Robert F. Klie's research group in the University of Illinois at Chicago with special appreciation to Liang Hong for his contribution.

I would like to thank the postdoctoral fellows of Dr. Droopad's group, Dr. Juan Salvador Rojas-Ramirez, Dr. Rocio Guerrero, and Dr. Manuel Caro for their wonderful help and support during my research. I also want to acknowledge Mr. Nate England, for his technical help and support to our research group. A special thanks to graduate and undergraduate students of Dr. Droopad's group who contributed to this research and helped me in experimental and analysis procedures: Shafiq Rahman, Susmita Ghose, Kevin Lion, Anna Amaro, Taylor Nash, and Hanu Arava. A special thanks to Dr.

Sayantan Das and Dr. Martin for their great help and support in the department of Chemistry.

Finally, I am indebted to my wife, Maedeh, my brother, Iman, and my parents for their support and encouragement.

TABLE OF CONTENTS

Page

LIST OF FIGURES

Figure **Page**

ABSTRACT

Oxide materials possess unique functionalities which when combined with semiconductors will enable a variety of novel device applications. They have properties that include high dielectric constant, ferromagnetism, and ferroelectricity. This research will focus on two major topics: (a) Materials/structure optimization of $CaCu_3Ti_4O_{12}/LiNbO_3$ (CCTO/LNO-Dielectric/Ferroelectric) based Voltage Controlled Capacitors (varicaps) and (b) deposition of ferroelectrics on III-V semiconductors or compound semiconductor based devices. Varicaps are electronic components with a capacitance that is tunable using a DC bias signal. The DC tunable dielectric constant of ferroelectric materials makes them a potential candidate for varicap applications. The frequency-dependent dielectric constant is a drawback for ferroelectric varicaps. This research investigates the frequency dependence of ferroelectric-based varicaps in combination with a large dielectric constant capacitor through the optimization of film deposition process and/or structures. Integration of ferroelectric oxide materials with high mobility III-V semiconductors is an attractive research topic albeit challenging due to the dissimilarity of the systems. The deposition and characterization of $Pb(Zr_xTi_{1-x})O_3$ (PZT) ferroelectrics on GaAs substrates is addressed in this research. The issue of gallium and arsenic diffusion and their reaction with lead atoms is mitigated using a buffer layer and employing a novel modified pulsed laser deposition technique to deposit the PZT films directly on GaAs/STO substrate.

CHAPTER I. INTRODUCTION

1.1. Background and Motivation

Modern technologies on semiconductor electronics is mainly based on silicon and compound semiconductors for high frequency application. The global market size for semiconductor industries was $333.2 billion in 2014 with an annual growth rate forecasted to be about 9% for 2014, 3.4% for 2015, and 3.1% for 2016 [1]. Semiconductor structures, because of their high electron mobility properties, provide a platform for novel electronic devices. Oxide materials possess functionalities when combined with semiconductors enable many novel device applications. One functionality is ferroelectricity.

Since the discovery of Ferroelectricity in 1921 [2], there has been tremendous progress in composition, properties, deposition and fabrication techniques, characterization methods, and applications of ferroelectric-based devices. Ferroelectrics are used in memories [3-6], transistors [7-9], sensors [10-12], actuators [13-15], microwave devices [16-18], optical switches [19-21], waveguides [22-24], optical modulators [25-27], and energy conversion [28-30].

Ferroelectric materials have a spontaneous electric polarization (dipole moment) which is switchable by an applied external electric field. In ferroelectric materials, the mechanical stress applied in the spontaneous polarization direction, induces a secondary polarization and surface charge due to the piezoelectric effect. The spontaneous electric polarization is temperature dependent. Net electric polarization of a ferroelectric material

depends on the temperature changes due to the pyroelectric effect. Ferroelectric materials have both pyroelectric and piezoelectric effects.

The dipoles that are all aligned in the same direction make different regions of a ferroelectric material, ferroelectric domains. Ferroelectric domains are separated by domain boundaries. Above the Curie temperature, ferroelectric materials lose their spontaneous electric polarization and enter paraelectric phase. Cooling the material below the Curie temperature forms domains that minimizes the total energy of the system, Figure 1.1.a.

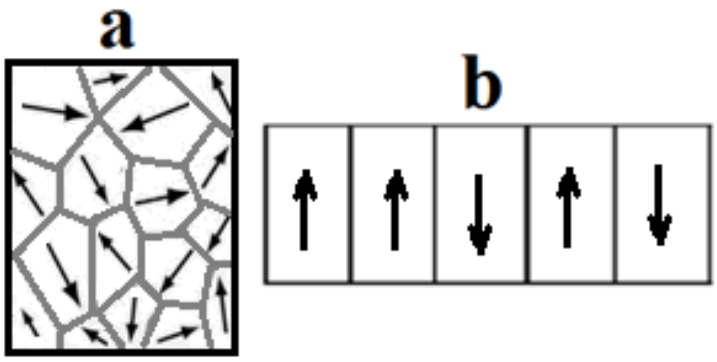

Figure 1.1: a: Ferroelectric domains and domain boundaries; domains are formed in an orientation that minimizes the total surface energy, b: Periodic domain in LNO

Electrical polarization of a ferroelectric material is switchable by applying an external electric field. The polarization switching loop is dependent on the current external electric field and its history. This history effect is called the hysteresis loop. In figure 1.2, a polycrystalline ferroelectric material has zero net polarization (A). Zero net polarization at zero electric field is the result of the ferroelectric domains oriented in

random directions. The external electric field switches the domains that are aligned parallel to the electric field direction (B). Alignment of all domains in the electric field direction saturates the net polarization (C). Decreasing the external electric field to zero, does not return the polarization to zero (D). Polarization at this point is called remnant polarization. Applying a negative external electric field switch the domains in the opposite direction. In the presence of a strong negative field, negative saturation occurs (F). Decreasing the magnitude of the negative field to zero, reduces the net polarization to the negative remnant polarization value (G). A positive electric field is required to reduce the net polarization to zero (H).

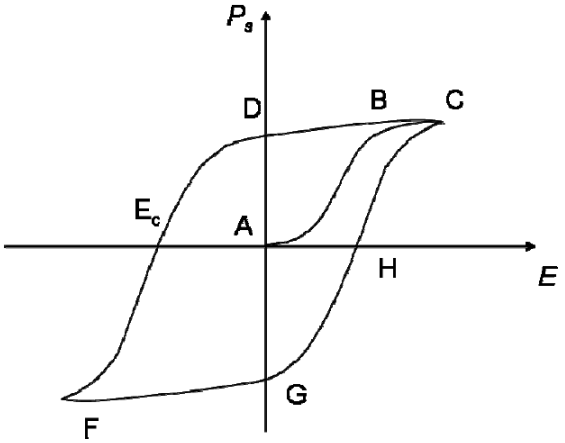

Figure 1.2: Ferroelectric polarization hysteresis loop

The existence of hysteresis in the P-E curve is proof of the ferroelectric effect. Polarization hysteresis loop measurements (P-E measurements) are one of the most useful characterization techniques to evaluate the quality of a ferroelectric material. An ideal ferroelectric material will have large remnant polarization.

This research is focused on two ferroelectric materials: $LiNbO_3$, Lithium Niobate (LNO), and $Pb(Zr_xTi_{1-x})O_3$, Lead Zirconate Titanate (PZT). Lithium Niobate, the silicon of optics, was discovered as a ferroelectric material in 1949 [31]. It has a trigonal lattice structure. It is a ferroelectric, piezoelectric, electro-optic and nonlinear optical material. LNO is an artificial material that does not exist in nature [32]. As a ferroelectric, LNO has two possible electrical polarization orientations. LNO has only 180-degree domain boundaries (see Figure 1.1.b). Utilizing the piezoelectric properties of LNO, this material is used for surface acoustic wave (SAW) devices [33- 35]. Its high Curie temperature provide for its use in high-temperature ultrasonic transducer applications [36]. LNO is a key material for optical systems. These include electro-optical modulators [19, 20], waveguides [22-24], and optical frequency converters [37, 38].

Lead Zirconate Titanates (PZT) are one of the most used ferroelectric materials in research and industrial applications. PZT exhibits a cubic structure at temperatures above Curie temperature (Tc). The material has no electric dipole moment (a paraelectric phase). The curie temperature of PZT depends on its composition. It is typically in the range of 230-480°C. The ferroelectric behavior of PZT at temperatures below Tc depends on its Zr/Zr+Ti ratio. In figure 1.3 [39], when the Zr/Zr+Ti ratio is below 0.53, PZT shows a tetragonal structure. Tetragonal PZT has polarization along the (001) direction. Increasing the Zr content where $x>0.53$, PZT transforms to rhombohedral phase with polarization along (111) direction. PZT with $x=0.53$ has its highest piezoelectric coefficient. PZT with low Zr content is used in memory applications because of its high

T_c value. Ferroelectric materials with the tetragonal structure similar to PZT have 90 degree and 180-degree domain boundaries.

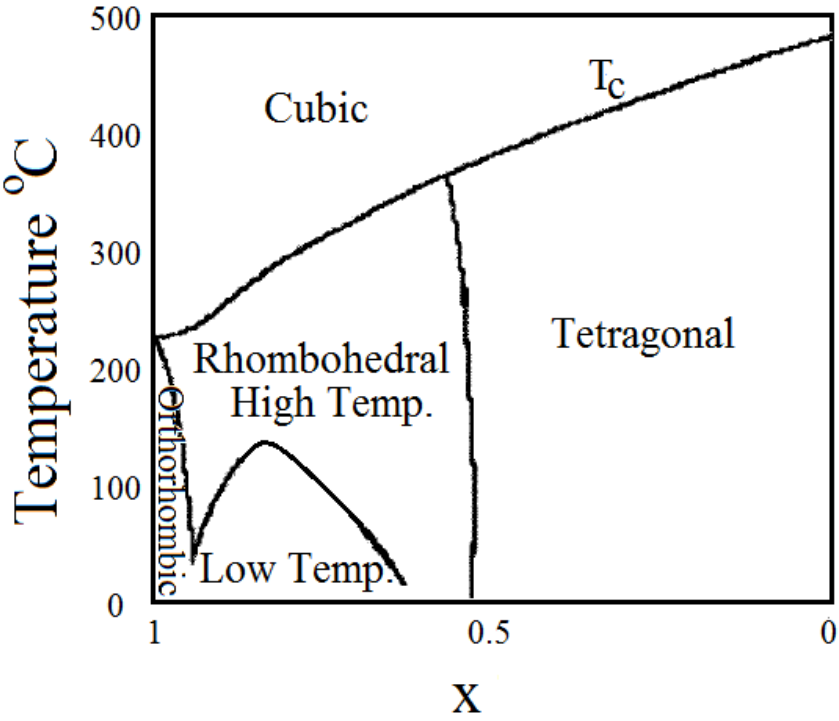

Figure 1.3: The phase diagram of PZT as a function of its composition factor (x) and temperature

The excellent piezoelectric properties of PZT makes this material a potential candidate for MEMS application [40]. High remnant polarization [41] and dielectric constant [42], electro-optical [43] and pyroelectricity [44] effects, enable variety of applications for PZT based materials. PZT films have attracted attention in device applications when integrated with semiconductors [45]. It requires the deposition of high-quality PZT films.

1.2 Dissertation Overview and Research Objectives

This research will be focused on two major parts: CCTO/LNO based varicaps and deposition of ferroelectrics on III-V semiconductors.

Chapter I, includes the introductory topics, following the motivations for this research. The importance of the ferroelectric materials and their application is also emphasized in this chapter. The dissertation overview and research objectives are also detailed in Chapter I.

In **chapter II**, the deposition techniques employed to fabricate the ferroelectric-based devices and the characterization techniques used are explained. This chapter introduces two oxide deposition techniques used during this research. Sol-Gel spin coating and thermal annealing for deposition of oxide thin films is described at the beginning of this chapter. This cost-effective deposition technique is employed for the fabrication of frequency-stabled varicaps. Pulsed Laser Deposition (PLD), as a precise deposition technique for oxide materials, is explained. PLD is employed for fabrication of high-quality thin films used for optical applications.

In **chapter III**, CCTO/LNO hetero-structures used for fabrication of stable frequency varicaps is introduced. Varicaps are electronic components with the capacitance that is tunable using a DC bias signal. The DC tunable dielectric constant of ferroelectric materials makes them a potential candidate for varicap applications such as frequency multipliers, tunable filters, and RF matching networks. The frequency-dependent dielectric constant is a drawback for ferroelectric varicaps. This chapter

investigates the frequency dependence of ferroelectric varicaps through the optimization of the film deposition process and/or structures. A discussion follows on the improvement of the electrical properties of a CCTO capacitor using a combination of a ferroelectric/dielectric; CCTO/LNO heterostructures.

Variation in dielectric constant of polycrystalline CCTO under exposure of UV light makes this material a potential candidate for fabrication of dynamic UV tunable capacitors or UV detectors. The use of CCTO material as a UV tunable capacitor or UV detector has two drawbacks: temperature dependence and frequency dependence of its dielectric constant will limit the applications of the fabricated device. **Chapter IV** explains a mechanism to reduce the frequency and temperature dependence of the CCTO-based UV tunable capacitor employing an LNO layer. The idea started from the observation of two interesting behaviors in CCTO capacitors. Above room temperature, increasing the frequency from 100kHz to 1MHz results in an increase in the dielectric constant of the CCTO. This behavior is totally different for lower frequencies. For frequencies above 100kHz, the sensitivity of CCTO capacitor to UV light is different than its behavior at lower frequencies. Below 100kHz the dielectric constant increases with UV illumination and above 100kHz the dielectric constant decreased with UV illumination. These two behaviors for CCTO at frequencies higher than 100kHz are different from the behavior of LNO which is opposite to those observed with CCTO. A combination of LNO and CCTO capacitors if selected with proper thickness ratio can compensate the frequency dependence of the CCTO. Close to the room temperature, the dielectric constant of the LNO shows a very low dependence on the temperature,

especially at higher frequencies. This fact can also be used to compensate for a large temperature dependence of CCTO dielectric constant at high frequencies. Fabrication of CCTO/LNO for optical applications requires the deposition of high-quality films with precise thickness. To achieve a single crystalline CCTO/LNO hetero-structure pulsed laser deposition technique is employed.

Challenging subjects behind the deposition of PZT ferroelectrics using PLD technique is the main focus of chapter V. PLD, as a versatile deposition technique, allows for a cost-effective, high quality film deposition of a variety of complex compounds including PZT. PLD deposition is based on the assumption of target material vaporization in a plasma plume and its stoichiometric transfer to the substrate. This is more challenging when depositing materials including volatile elements such as lead. This chapter reports the issue of Pb depletion in PLD deposition of PZT under a wide range of oxygen background pressure. The chapter shows a mechanism to control the Zr/Ti ratio of the PZT film using the pressure of the oxygen during the deposition. Zr/Ti or Zr/Zr+Ti ratio is important parameters affecting the electrical properties of PZT. The lattice parameters and electrical properties of PZT films deposited using the oxygen pressure as a control parameter for Zr/Zr+Ti ratio are compared in this chapter.

Chapter VI is focused on the integration of ferroelectric oxide materials with high mobility III-V semiconductors. The deposition and characterization of PZT ferroelectrics on GaAs substrates is addressed in this chapter. The issue of gallium and arsenic diffusion and their reaction with lead atoms mitigated with a buffer layer is developed. A novel modified pulsed laser deposition technique to deposit the PZT films

directly on a GaAs substrate with a thin buffer layer of STO is identified. A rapid thermal annealing process was developed to enable the deposition of high quality PZT films on GaAs/STO substrate using a sol-gel technique.

Chapter VII is the conclusion of the performed research, results, and suggestions for future work on this topic.

CHAPTER II. DEPOSITION AND CHARACTERIZATION TECHNIQUES

This chapter introduces the techniques for oxide thin film deposition and characterization.

2.1 Deposition Techniques

This section introduces two oxide deposition techniques used during the present research. Sol-Gel spin coating and thermal annealing for deposition of oxide thin films is described at the beginning of this chapter. This cost-effective deposition technique is employed for the fabrication of frequency-stabled varicaps. Pulsed Laser Deposition (PLD), as a precise deposition technique for oxide materials, is then explained. PLD is employed for fabrication of high-quality thin films used for optical applications.

2.1.1 Spin Coating and Thermal Annealing

A spin coating process utilizes a small amount of coating material (in a solvent at a certain temperature) applied to the center of the wafer. Spinning the sample at high speed spreads the material on the wafer surface due to the centrifugal force. Neglecting the evaporation of the solution, when the fluid flow is small enough to neglect the Coriolis Effect and the film layer is thin enough to make a uniform gravitational normal force, spin coating results in a uniform film coating. Evaporation significantly affects the spin coating process [46-48]. Most of the ferroelectric spin coating solutions in the market are composed of the nano-particles of oxide materials dissolved in alcohol. The

high evaporation rate of the alcohol affects the uniformity of the deposited film. The variety of oxide solutions used in the present research requires minimization of the evaporation rate. Evaporation rate is reduced by lowering the temperature. Pure argon gas is cooled using a Peltier cooling element and introduced into the process environment. This modified spin coating setup is shown in figure 2.1 The process temperature can be reduced to 3˚C. This new setup results in significantly improved coatings of PZT solution comparing with the room temperature spin coating of the same solution.

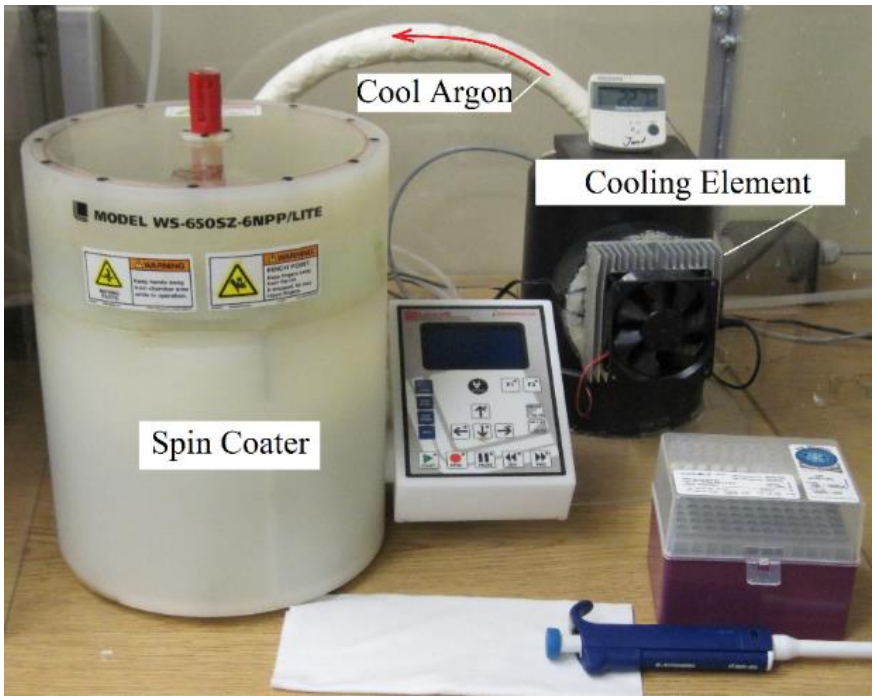

Figure 2.1: Spin coater with temperature controlled argon atmosphere

Deposition of oxide thin films using the spin coating process requires three annealing steps: solvent evaporation, pyrolysis, and post annealing. The first annealing

step dries the film after spin coating. Depends on the oxide material and its solvent, a temperature in the range of 80°C-250°C is a function of the oxide material and the solvent. The film shrinks due to the elimination of the excess solvent.

In the second step, pyrolysis, a higher temperature removes the organic compounds. Pyrolysis temperature is often below the oxide material's crystallization temperature. A temperature in the range of 300°C-500°C is a function of the oxide material employed. Pyrolysis eliminates the organic compounds by evaporation or decomposition. This chemical process often needs to be carried out in a controlled atmosphere of an inert gas.

The sample is then annealed at a higher temperature for crystallization of oxide material. This step determines the property of the oxide films. The temperature ramp rate, maximum temperature value, and annealing duration are the key parameters that determine the quality of the deposited material.

A tube furnace with controlled argon and oxygen feeds (figure 2.2.a), a small box furnace (figure 2.2.b), and a box furnace with controlled argon and oxygen feeds (figure 2.2.c) were used. The employed single zone tube furnace provides a controlled ambient for annealing small samples up to 850°C. The small box furnace is not ambient controlled. It allows for faster temperature ramps up to 1050°C. The larger box furnace has a controlled ambient for annealing the large-size samples up to 1200°C.

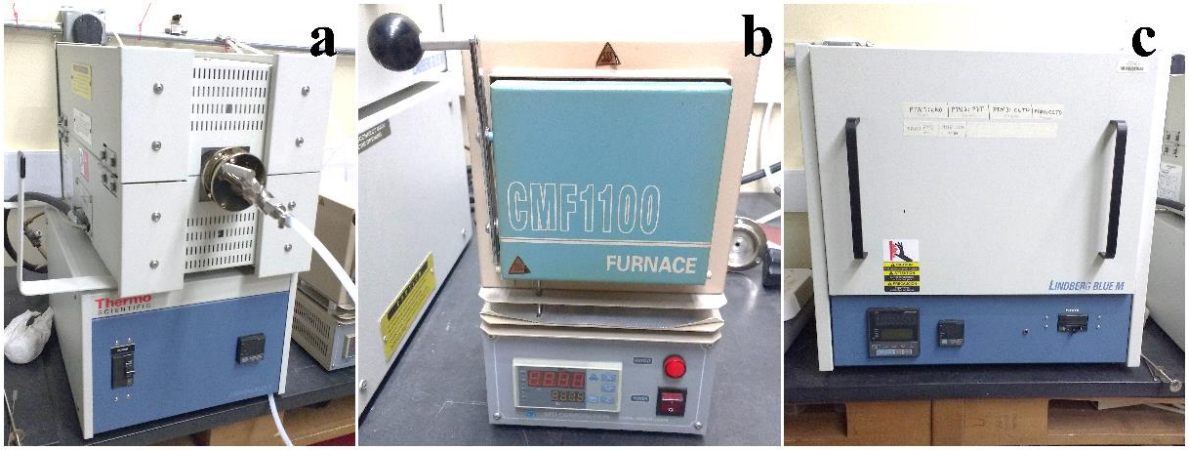

Figure 2.2: a. Tube furnace with controlled argon and oxygen ambient, b. Small box furnace, c. Box furnace with controlled argon and oxygen ambient

2.1.2 Pulsed Laser Deposition

Pulsed Laser Deposition (PLD) is a vapor deposition technique where a high-powered UV laser pulse ablates the target material that is being deposited. A UV laser with the wavelength of 200nm-400nm is normally employed for PLD systems because of the high absorption of different materials. The focused nanosecond pulse laser beam penetrates into the target material. The electric field generated by the high power laser accelerates the electrons in the penetrated region, then removes them from the bulk material. The free electrons oscillate under the effect of the electromagnetic field of the UV laser. The collision between the oscillating free electrons and the atoms of the target material results in the conversion of the energy into the thermal, chemical and mechanical forms. This process results in the evaporation of the material, ablation, and formation of plasma [49]. The main reason for using a short laser pulse for PLD process is to minimize

the dissipation of energy beyond the ablated region, resulting in less damage to the remained target material.

The temperature of the PLD chamber is close to room temperature. The plasma plume comprises high energy electrons, ions, atoms, and molecules with the temperature in the order of several thousand Celsius. The vaporized material in the plasma plume is deposited as a thin film on a heated substrate located in front of the target. This process may occur in an ultra-high vacuum chamber or in the presence of a background gas. For many oxide materials, to prevent the oxygen loss, the process is done in the presence of the oxygen gas.

In PLD system, the nucleation and growth of the deposited film on the substrate are affected by the laser flux, substrate temperature, substrate surface parameters, background gas, and pressure. A simplified diagram of the pulsed laser deposition system is shown in figure 2.3. The laser emitter is located outside the chamber. It provides significant flexibility in the design of the PLD system. The laser beam is focused on the target surface using a system of optical lens. The formed plume is directed perpendicular to the target surface. The substrate is located parallel to the target plane. The mechanical design of the PLD systems allows for adjusting the distance between the substrate and the target.

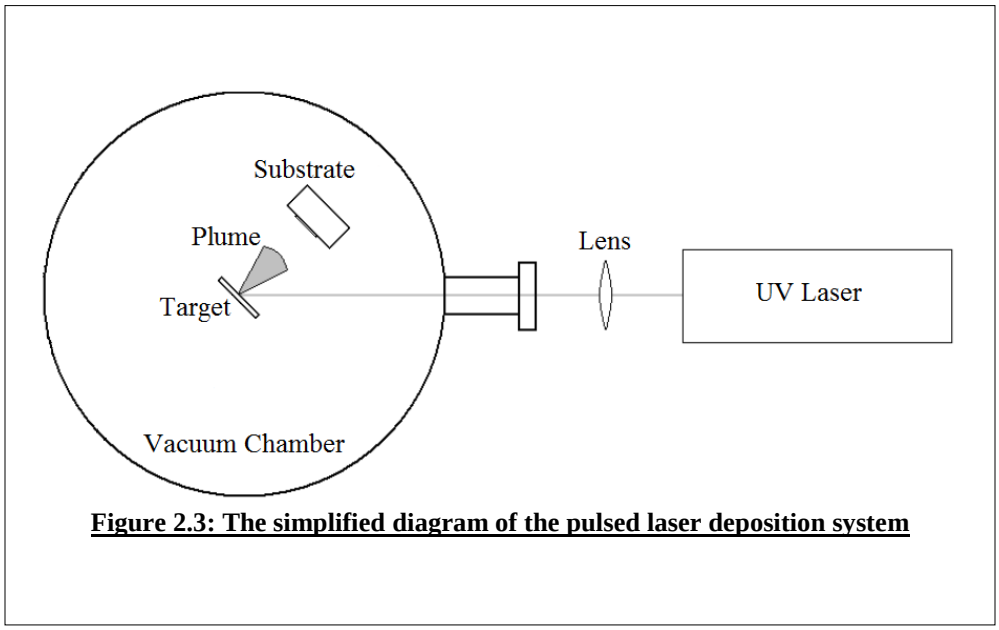

Figure 2.3: The simplified diagram of the pulsed laser deposition system

The target, normally built in a disk shape, is often rotated during the laser exposure period. It allows for a uniform illumination over the entire surface of the target, resulting in less roughening of the target surface. The physical and chemical stability of the target material is an important factor in PLD technique. Ball milling, hot press, and sintering of the oxide material is the most common method to prepare a target for the PLD system. The density of the ceramic targets is as high as possible because of the high absorption rate of the dense materials and their low thermal conductivity due to the grain boundaries.

Laser flux; The laser energy per surface area in a PLD process should be high enough to cause the ablation of the target material. The use of laser flux more than required causes ejection of particles. The laser flux can be used as an effective parameter to control the stoichiometry of the deposited material.

Laser Frequency; The laser frequency is an important parameter affecting the deposition rate of PLD system. Higher deposition rate, resulting in faster growth, is ideally desired. The formation of defects during the rapid PLD growth is counterproductive. A proper time between laser pulses allows for the crystallization process to occur, minimizes defect formation and improves the crystal quality.

Target-substrate distance; The distance between the target and the substrate is an effective parameter determining the kinetic energy of the arriving species to the surface of the substrate in the presence of a background gas, influencing the nucleation and growth of the deposited film. A proper distance can prevent species segregation while traveling to the substrate.

Substrate temperature; The quality of the deposited film in pulsed laser deposition system is dependent on the temperature of the substrate during the deposition and the temperature of the post-annealing process.

Background gas and pressure; to avoid oxygen depletion during the growth of oxide thin films, the presence of oxygen in the vacuum chamber is necessary. The gas pressure is an effective parameter determining the kinetic energy of the arriving species to the surface of the substrate. The background pressure significantly affects the expansion of the plume. Higher background pressure concentrates the plume into a smaller area.

The pulsed laser deposition system employed for this research is located in Electroceramics lab at Texas State University It is manufactured by NBM Systems. A

COHERENT 248nm KrF laser with the maximum energy of 600 mJ and the maximum frequency of 10Hz is coupled with an ultra-high vacuum chamber. The optical setup for guiding the laser beam into the chamber window is shown in figure 2.4. The aperture passes the highest energy area of the laser spatial profile. The first 45° mirror guides the laser beam to a vertical path. The laser lens converges the laser beam and the second mirror guides the focused beam on the surface of the target through a fused silica window.

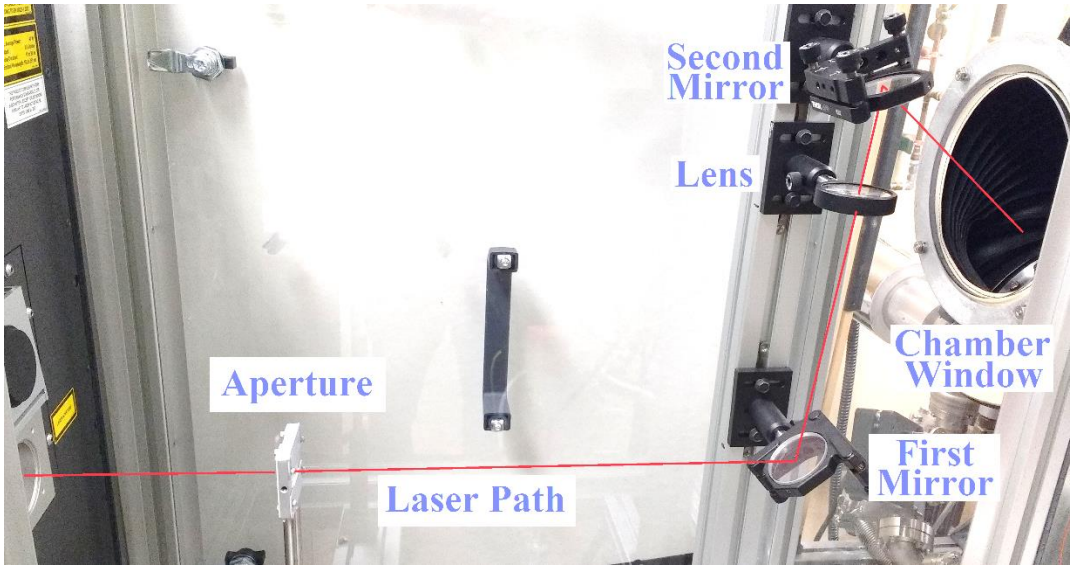

Figure 2.4: The optical setup for guiding the laser beam into the PLD chamber

The PLD chamber consists an ultra-high vacuum chamber coupled with an isolated load-lock unit. The main chamber is evacuated using a speed-controlled turbo pump with a backing rough pump resulting in a base pressure of 2.7×10^{-9} Torr. The chamber can also be isolated from the pump path using a mechanical valve. The main chamber is normally isolated from the load lock unit using a pneumatic gate valve. The

load lock unit is evacuated using a small turbo pump with a backing rough pump resulting in a base pressure of 4.8×10^{-8} Torr.

The design of this PLD chamber allows for the mounting of the target and substrate in the level plane. The substrate, oriented in the horizontal plane, is loaded in a manipulator mounted on top of the chamber. The mechanism allows for adjusting the target-substrate distance using a flexible bellows. Speed controlled DC motor rotates the substrate during the deposition period to achieve a uniform deposited film. A heating element located behind the substrate can heat up the substrate during the PLD process. The temperature is monitored and controlled via a thermocouple located in the proximity of the substrate surface. The setup allows for a maximum temperature of 850°C on the surface of the substrate in the presence of the background gas.

The target holder has the capacity for six 1" targets. A DC motor coupled with an absolute encoder mechanism was designed and built to switch the targets. The PLD setup can be used for deposition of oxide hetero-structures without the need for venting the chamber to the atmosphere to change the targets. The background pressure in the PLD chamber can be increased with oxygen and argon gas. A mass flow meter is employed to adjust the pressure of the chamber through controlling the flow of the gas. The pressure of the chamber can also be adjusted by changing the speed of the turbo pump. This setup allows for increasing the pressure up to 300mT. Figure 2.5 illustrates the PLD instrument located in Electroceramics lab at Texas State University. The chamber is equipped with a Reflection High Energy Electron Diffraction (RHEED) instrument for *in-situ* film growth

monitoring. A differential turbo pump is employed to maintain a pressure lower than the chamber pressure in the RHEED gun.

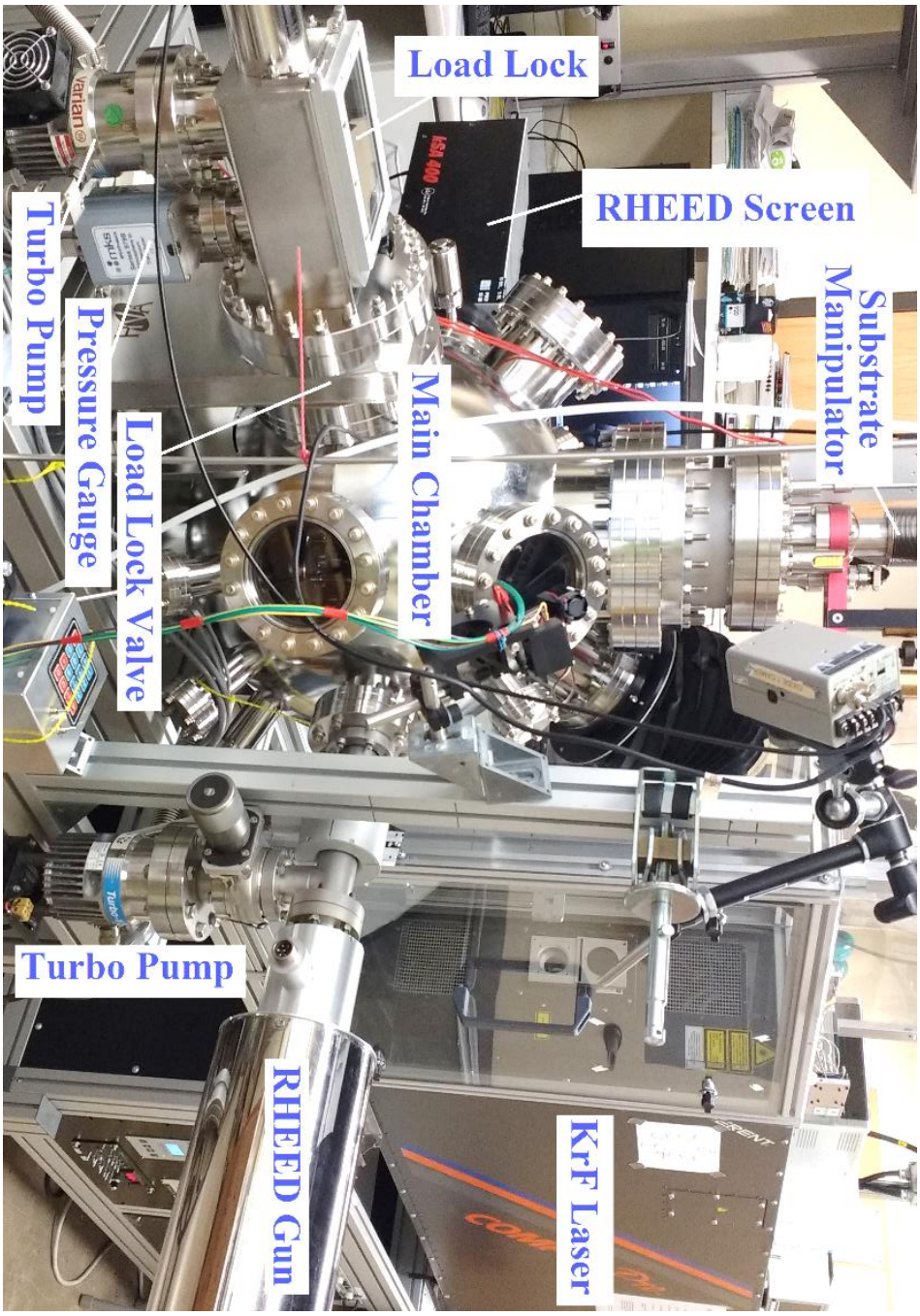

Figure 2.5: the PLD instrument located in Electro-ceramics lab at Texas State University

2.2 Characterization Techniques

This section introduces the implemented characterization techniques and instruments during the present research.

2.2.1 X-RAY Diffraction (XRD)

The short wavelengths of X-Ray that is in the same order of magnitude as the lattice constant of the functional oxides, make this electromagnetic waves a potential candidate to study the lattice structure of oxide crystals. Atoms scatter X-Ray waves, producing the secondary spherical waves that make interference patterns in different directions. There are a few directions in which an array of scattered patterns from an array of atoms makes a constructive interference determined by Bragg's law:

$$2d\ Sin(\theta) = n\lambda$$

Where d is the lattice spacing, Θ is the grazing angle, n is an integer number, and λ is the wavelength of the X-Ray beam. Employing an X-Ray detector to measure the X-Ray intensity in different angles, yields unique X-Ray intensity peaks representing the lattice spacing of the under-test material. The position of the intensity peaks can be translated to the relative lattice spacing using the Bragg's law.

Considering the high penetration rate of the X-Ray, XRD is a powerful instrument to characterize the crystal structure of different film layers in a hetrostructure. BRUKER D8 ADVANCE (figure 2.6.a) and BEDE D1 System (figure 2.6.b) XRD instruments are employed during this research.

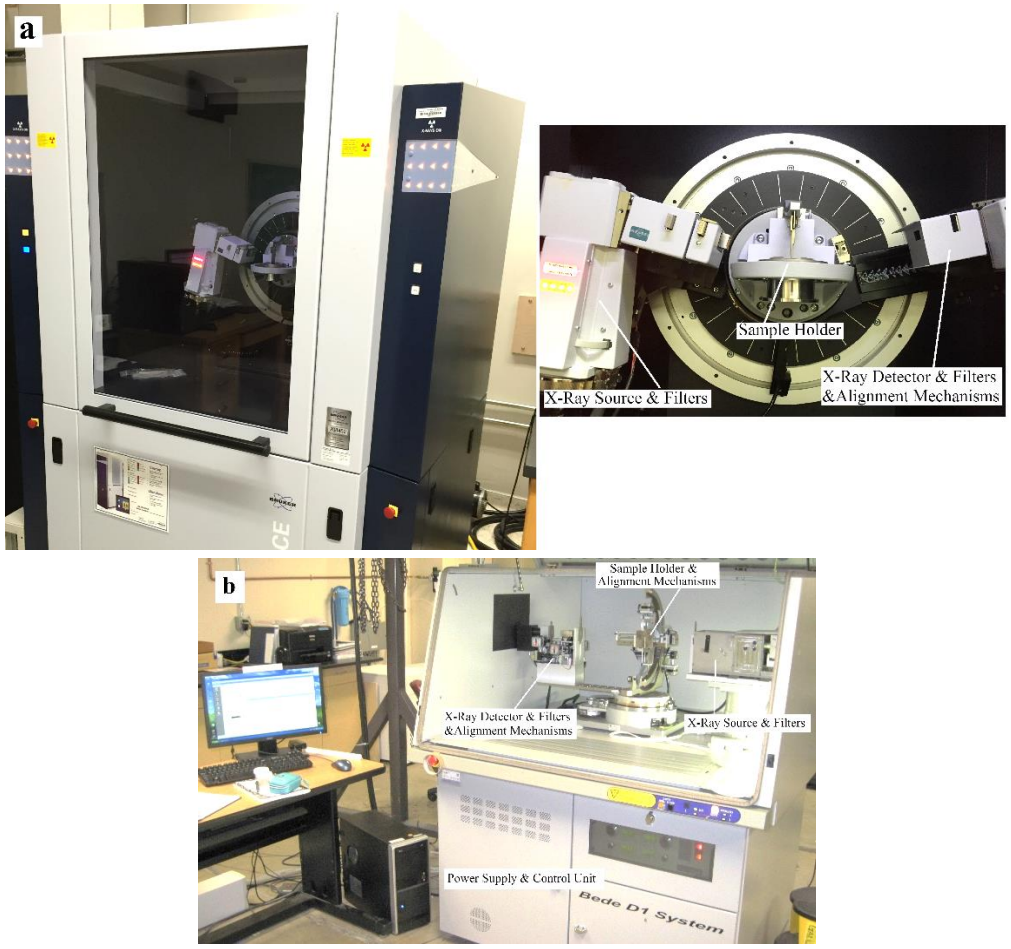

Figure 2.6: a. BRUKER D8 ADVANCE, b. BEDE D1 System XRD instruments employed during this research

2.2.2. Scanning Electron Microscopy (SEM)

SEM is a high resolution imaging technique using electron beams focused by an array of electromagnetic lenses in a vacuum chamber. The narrow electron beam is scanned on the sample surface using scanning coils. High energy electrons emitted from the sample after scattering are captured using an electron detector. The intensity of the

detected electrons represents the brightness for SEM image. This way, the topography of the surface can be measured. FEI Helos Lab 400 scanning electron microscope, as shown in figure 2.7, was implemented in this research. The system also has the capability for Energy Dispersive X-Ray Spectroscopy (EDX). EDX is a powerful technique for elemental analysis of samples. In this characterization technique, a focused beam of charged particles such as electrons or X-Ray targets the surface of the sample. The beam excites the electrons of the atoms which are normally in the ground state, resulting the ejection of electron and formation of an electron hole. An electron from the higher energy state fills the electron hole and releases an X-ray ray. Knowing the fact that electrons of an atom may take unique discrete energy levels, the energy and the numbers of emitted X-Rays, if measured by an energy dispersive spectrometer, can be employed for elemental analysis.

Figure 2.7: FEI Helos Lab 400 scanning electron microscope instrument employed during this research

2.2.3. Atomic Force Microscopy (AFM)

Atomic force microscope is a type of scanning probe microscopes with sub-nanometer resolution used for topography measurement, and nano-scale manipulation. In AFM, a sharp tip cantilever that is oscillating by a piezoelectric element is loaded on a precision XYZ stage. When the cantilever tip is in the proximity of the sample surface, its deflection, amplitude, or oscillation frequency may be affected by the atomic scale force. A variety of optical or electro-mechanical techniques may be used to monitor the situation of AFM tip. Scanning the sample surface using the AFM tip, while controlling a constant force between the tip and the sample, provides the sample topography measurement. PARK Systems XE7 AFM instrument, as shown in figure 2.8, was implemented during this research. The system also has the capability for Piezoresponse

Force Microscopy (PFM) allowing for ferroelectric domain manipulating and imaging. In PFM, an ac current is applied to the sample through a conductive tip. The ac signal excites the piezoelectric sample. The deformation in the sample is extracted from the cantilever deflection using a lock-in amplifier. In result, the ferroelectric domains can be imaged. The ferroelectric domains of the under test sample can also be switched by applying a dc signal during the PFM measurement.

Figure 2.8: PARK Systems XE7 AFM instrument employed during this research

2.2.4. Ferroelectricity measurement (P-E measurement)

P-E hysteresis loop measurement as explained in Chapter 1 is an important evidence for ferroelectricity behavior of materials. Remnant polarization, as an important factor to compare the ferroelectricity quality of the materials is also extracted from P-E

hysteresis loop. The RADIANT ferroelectric analyzer, as shown in figure 2.9, was employed for ferroelectricity measurements during the present research. The analyzer is capable of carrying out P-E measurements up to ±9V. The system is also coupled with a high-voltage (H. V.) power supply and amplifier that enables ferroelectricity measurement on thick ceramic samples up to 2.5kV.

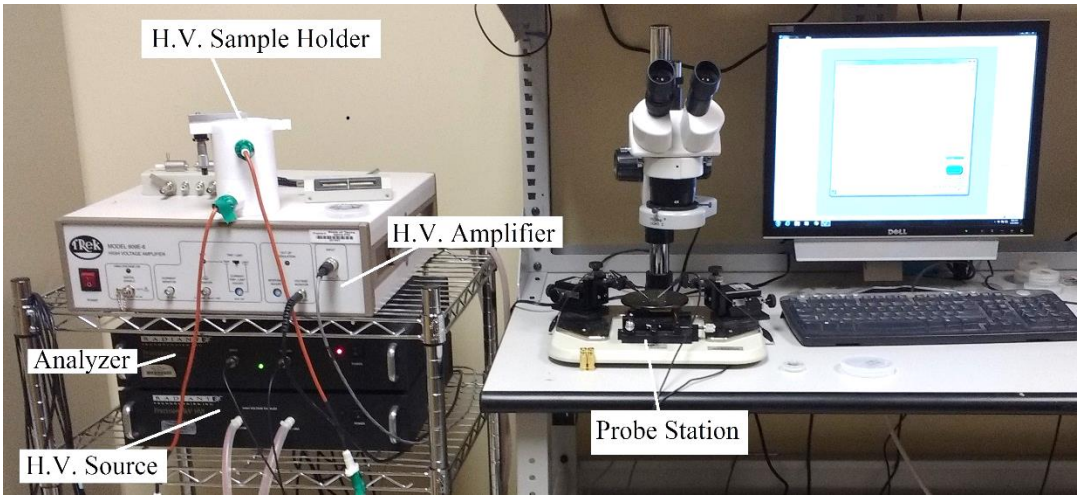

Figure 2.9: RADIANT ferroelectric analyzer instrument employed during this research

2.2.5. LCR Measurements

Impedance analyzers and LCR meters often work by applying a known ac voltage to the under test component while measuring the amplitude and phase of the current passing through the component. Knowing the amplitude and phase of the voltage and current, the complex impedance can be calculated. The complex impedance measured at different frequencies can be used for calculating the unknown resistance, capacitance, and inductance if the electric model and equivalent circuit of the component is known. A

WAYNE KERR 6500B precision impedance analyzer, as shown in figure 2.10, was employed for LCR measurements during this research.

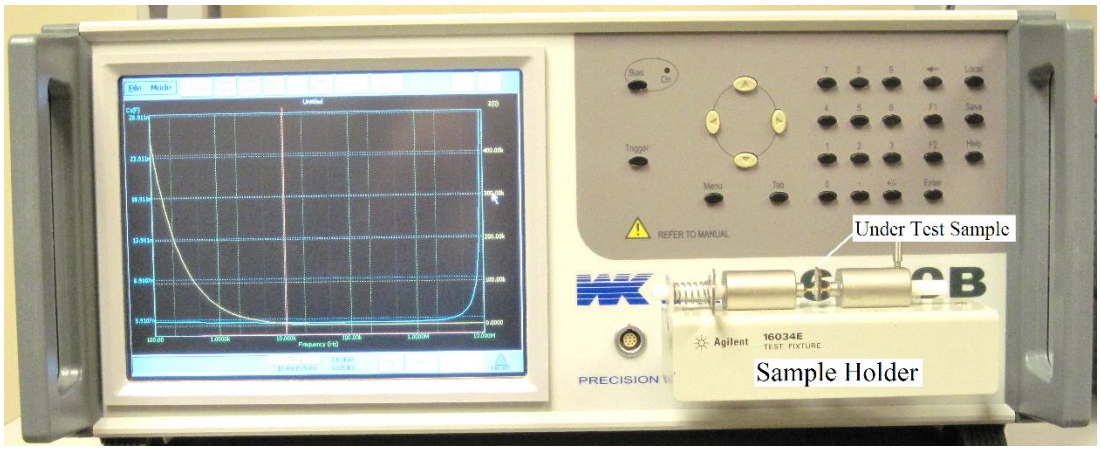

Figure 2.10: WAYNE KERR 6500B precision impedance analyzer employed during this research

CHAPTER III. CCTO/LNO VARICAPS

3.1 Introduction

Varicaps (Varactors) are voltage controlled capacitors. These are electronic components with the feature that their capacitance is tunable employing a DC voltage. Varicaps are used in variety of applications including frequency multipliers [50], Voltage Controlled Oscillators (VCO) [51, 52], tunable amplifiers [53, 54], Tunable filters [55-57], tunable phase shifter [58, 59], Tunable antennas [60, 61], and RF matching networks [62, 63]. Ferroelectric materials, because of their DC tunable dielectric constant, are widely used in varicap applications. The influence of frequency on the dielectric constant of ferroelectric materials affects the functionality of ferroelectric-based varicaps. In this study, $LiNbO_3$ (LNO) ferroelectrics are used for varicap application.

The electrical behavior of a ceramic capacitor can be modeled as a series combination of a resistor, capacitor, and inductor. The capacitor is represented by the dielectric properties of the ceramic material; the resistor is represented by the resistive behavior of the materials, and the inductor is represented by the parasitic inductance [64]. The impedance of a series RLC circuit is calculated as:

$$Z = R + j\left(\omega \mathrm{L} - \frac{1}{\omega \mathrm{C}}\right) \qquad (3.1)$$

Any series RLC circuit has a resonance frequency of ω_0 where:

$$\omega_0 = \frac{1}{\sqrt{LC}} \qquad (3.2)$$

Considering a very small value for frequency, ω, in equation (3.1), the impedance is dominated by the capacitor. At high frequencies, impedance is dominated by the inductor. Figure 3.1 illustrates the magnitude and phase components of the impedance for the series RLC circuit.

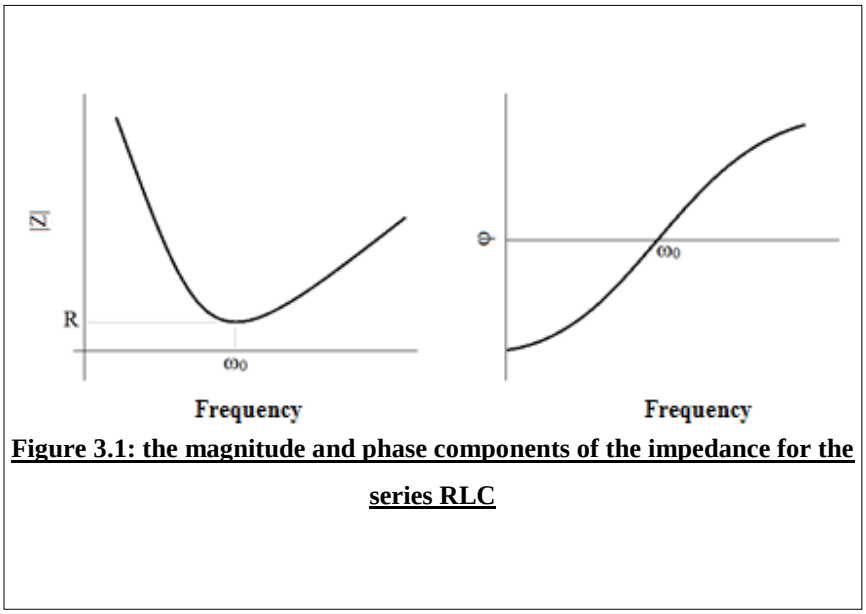

Figure 3.1: the magnitude and phase components of the impedance for the series RLC

An LCR meter to measure the capacitance of a ceramic capacitor results in an interesting result as shown in figure 3.2. The negative value measured by LCR meter at frequencies above the resonance frequency may be confusing. This result can be explained by the inductive behavior of the series RLC circuit.

The LCR meter calculates the amplitude and angle of the impedance by measuring the phase and angle of the voltage and current. When LCR meter measures the capacitance, while experiencing an inductive component, it calculates a negative value for the impedance phase of the under-test component. It calculates and shows a negative capacitance value.

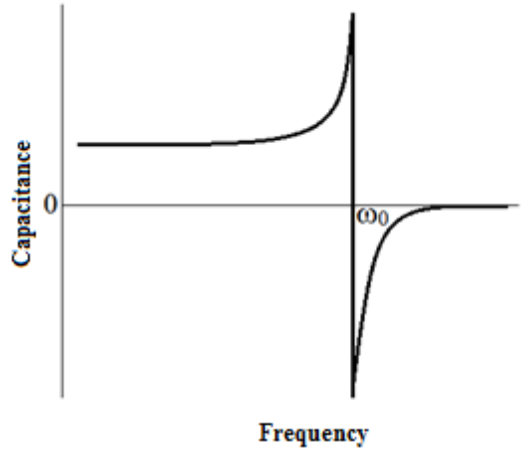

Figure 3.2: Frequency dependence of the dielectric constant of a ceramic capacitor

The dielectric constant depends on the measurement frequency. The dielectric constant of the ferroelectric materials decreases with the increase of the frequency. The capacitance measurement of a ferroelectric capacitor looks like the image below. Approaching the resonance frequency from low frequencies, the capacitance measured by the LCR meter decreases. In the proximity of the resonance frequency, the measured capacitance increases.

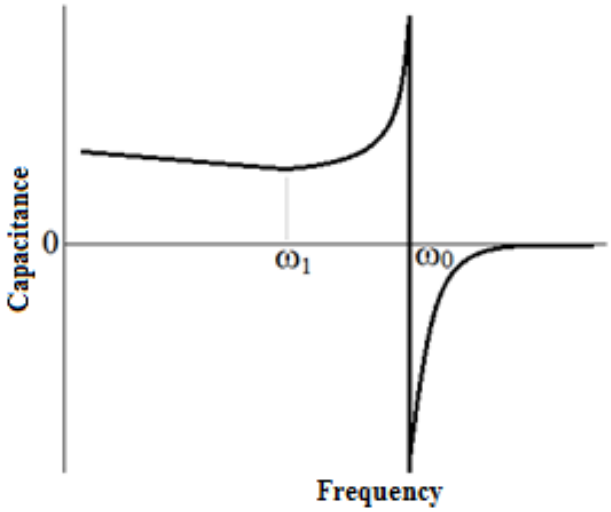

Figure 3.3: Measured capacitance using an LCR meter

The performance of a ceramic capacitor may be limited because of the variation of its dielectric constant with frequency. The issue is more serious when using a capacitor for wideband circuits. The simplest solution for this problem is choosing a working frequency in which the component has the smallest variation in capacitance with respect to frequency (dC/dF). ω_1, as shown in the image above, is a good candidate for smallest dC/dF value. Three parameters determine the value of ω_1, the frequency dependent dielectric constant, the total capacitance, and the parasitic inductance. Neglecting the parasitic effects, any dielectric material has an identical ω_1 which depends on its capacitance value. Using the dC/dF minima is limited to very specific capacitance-frequency points.

Adding another capacitor with a different dielectric material provides more freedom in tuning the position of dC/dF minima. In this research, a ferroelectric/ dielectric heterostructure is employed to build a series of two capacitors. The position of

ω_1 in this ferroelectric/ dielectric heterostructure can be tuned changing the ratio of the ferroelectric/dielectric capacitors or changing the total capacitance.

Fabrication of miniaturized capacitors for wideband electronic systems requires the use of materials with high dielectric constants. $CaCu_3Ti_4O_{12}$ (CCTO) has a high dielectric constant and temperature stability. In this study, a cost-effective procedure is employed to fabricate frequency stabled CCTO/LNO hetero-structure varicaps. CCTO and LNO films are deposited on HF terminated Si wafer using chemical solution deposition.

3.2 LNO/CCTO hetro-structure

Focus was on the fabrication of Si/LNO/CCTO structure. To fabricate the Si/LNO/CCTO structure, the Si (100) wafer was cleaned in 5% HF acid for 7 minutes and rinsed. This removed the oxide layer. The wafer was moved to the spin coater chamber. After HF treatment, SiO_2 will grow on the wafer with the rate of 0.06Å/min at room temperature [65]. The transfer time was minimal. The spin coater chamber was filled with pure Argon gas.

The Chemat LNO solution has 2-Methoxyethanol as the solvent. It was employed for spin coating of LNO thin film. The optimized spin coating recipe experimentally determined for deposition of this solution is illustrated in figure 3.4. The spin coating recipe comprises a two-step process. The wafer is rotated at 500 RPM for 6 seconds to coat the entire surface of the wafer with the solution. In the second step, the wafer rotated

at higher speed (3000 RPM) for 30-seconds. This smooths out the surface with a thin film of LNO solution on the wafer's surface.

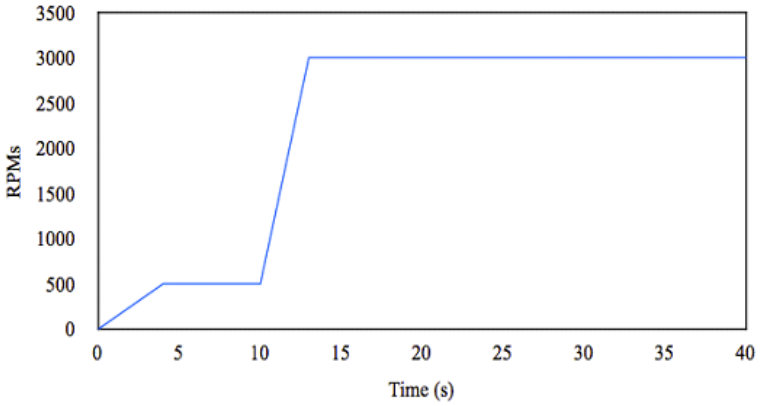

Figure 3.4: LNO spin coating recipe

The spin coated wafer was transferred to a tube furnace with a controlled atmosphere. After a pyrolysis step at 300°C for 30 min in a pure argon atmosphere, the sample was annealed at 500°C in a 5%-oxygen/95%-argon environment for 60 minutes. The LNO crystallization occurs at this annealing temperature [66-68]. The LNO annealing recipe is illustrated in figure 3.5.

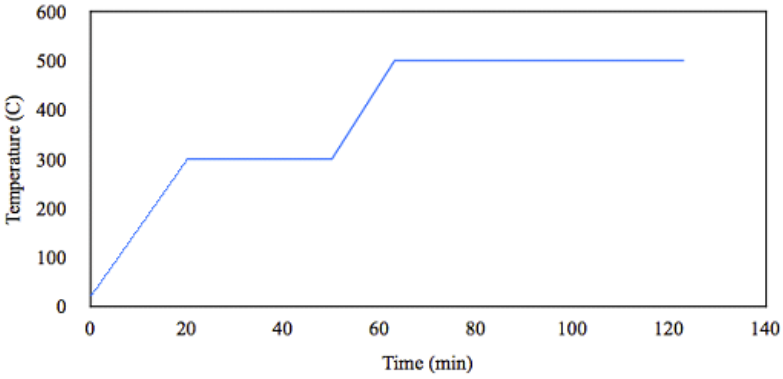

Figure 3.5: LNO annealing recipe

The thickness of the films was measured with Woollam M2000 Ellipsometer. Measurements were performed from 200nm to 1000nm at 65°, 70°, and 75° angles. Complete Ease software was used to determine the film thickness. The ellipsometry indicates a 20.78nm LNO film on the wafer. Capacitance-Voltage (C-V) measurements of the coated wafer are illustrated in figure 3.6. A Metal/Ferroelectric/Semiconductor (MFS) behavior is observed [69]. In this experiment, 6mm diameter gold electrodes (with the thickness of 10nm) are form the capacitor plates. Two important properties of MFS hetero-structures are observed in this measurement. The DC tunable dielectric constant of the ferroelectric material (LNO), and band bending in Ferroelectric/ Semiconductor interface due to semiconductor modulation using ferroelectric polarization charge are observed.

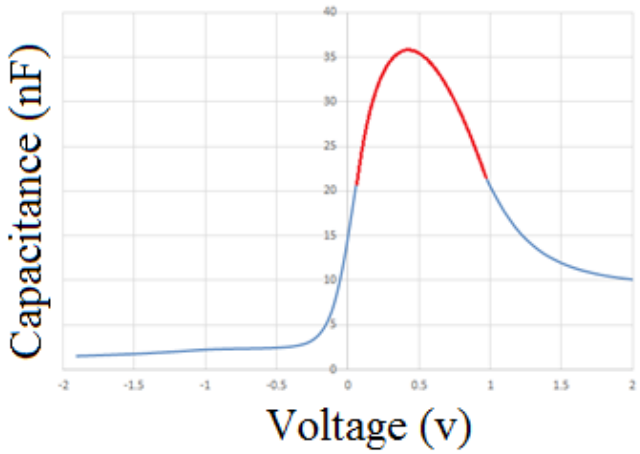

Figure 3.6: C-V measurement on Au/Si/LNO/Au sample

The values above 20 nF are out of the measurement range of the employed C-V measurement instrument; So, it is indirectly measured using a series reference capacitor

This MFS structure can be used as a voltage controlled capacitor in the linear region of the C-V curve. The frequency dependence of the structure compromises the utility of this component. Figure 3.7 shows the capacitance and the dielectric loss factor of the fabricated Si/LNO structure in the range of 1kHz-10MHz. Capacitance decreases by increasing the frequency. At the resonance frequency (≈8.5MHz), the capacitance starts to increase rapidly. The capacitor at frequencies higher than the resonance frequency shows an inductive behavior.

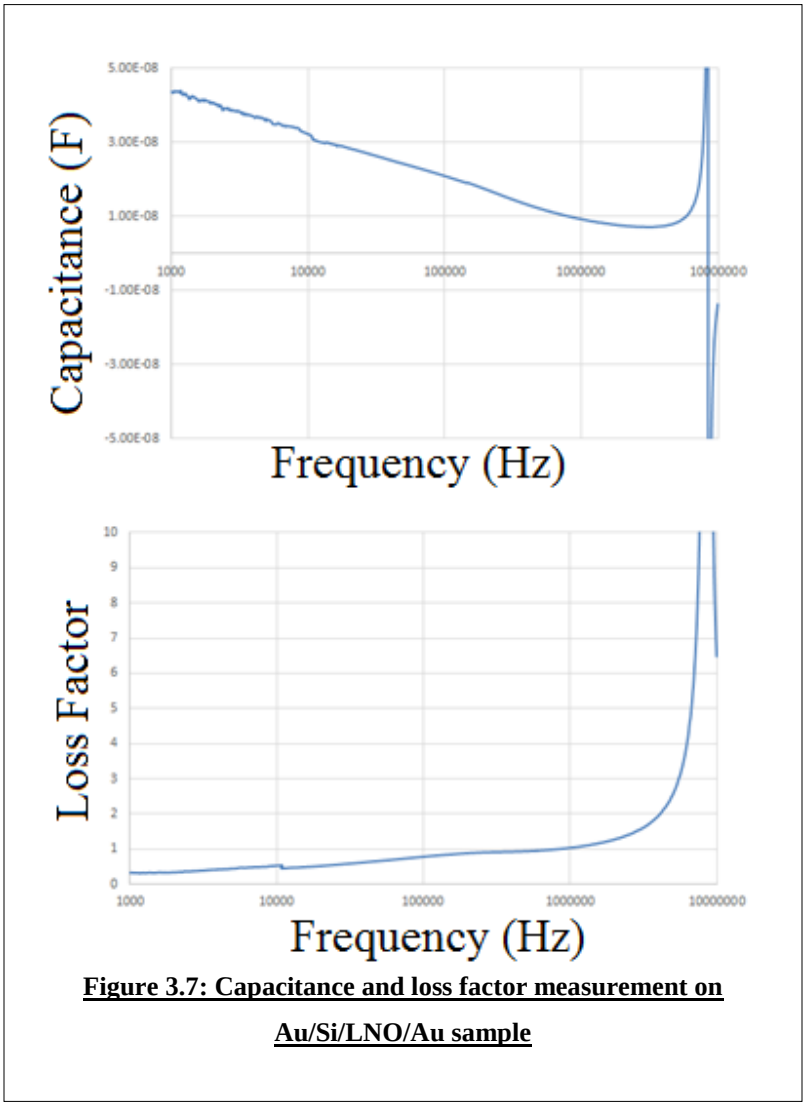

Figure 3.7: Capacitance and loss factor measurement on Au/Si/LNO/Au sample

The Chemat CCTO solution, composed of source material in 2-Methoxyethanol, was employed for spin coating of CCTO thin film. The optimized spin coating recipe, experimentally determined for deposition of this solution, is illustrated in figure 3.8. The spin coating recipe comprises a one-step process. Rotation the wafer at 3000 RPM for 20 seconds results in a thin film of CCTO solution on the wafer.

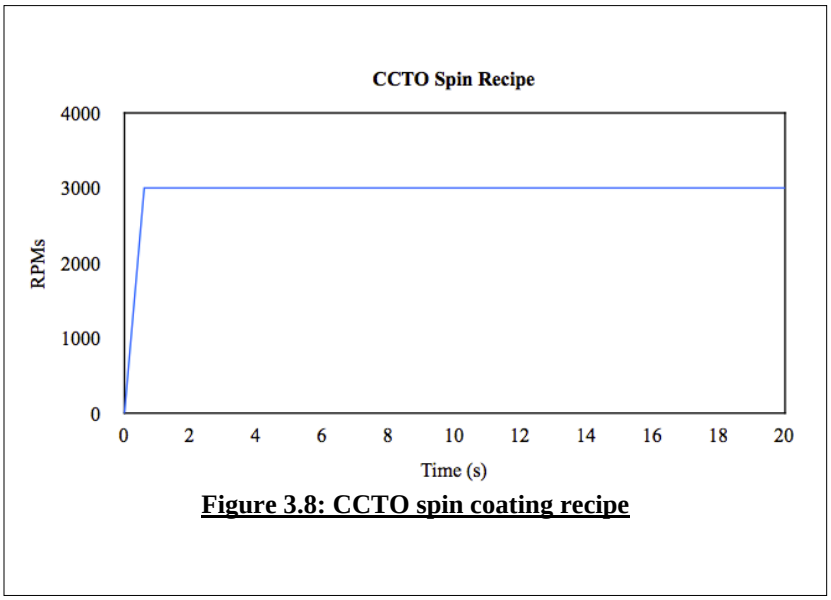

Figure 3.8: CCTO spin coating recipe

The wafer after spin coating process was transferred to a tube furnace with a controlled atmosphere. After a pyrolysis step at 300°C for 30 min in a pure argon atmosphere, the sample was annealed at 500°C in a 5%-oxygen/95%-argon environment for 60 minutes.

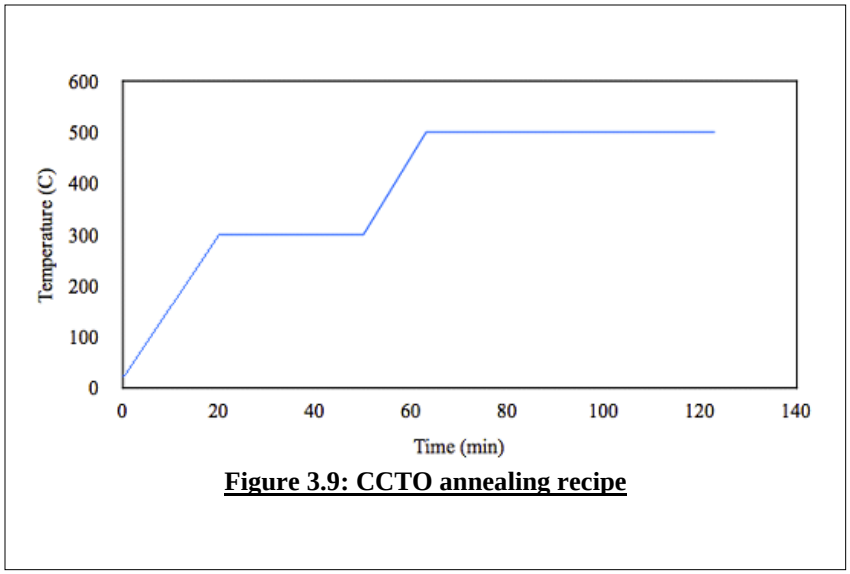

Figure 3.9: CCTO annealing recipe

The ellipsometry measurement shows 24.16nm CCTO film on the wafer. The summary of Si/LNO/CCTO fabrication process is illustrated in figure 3.10.

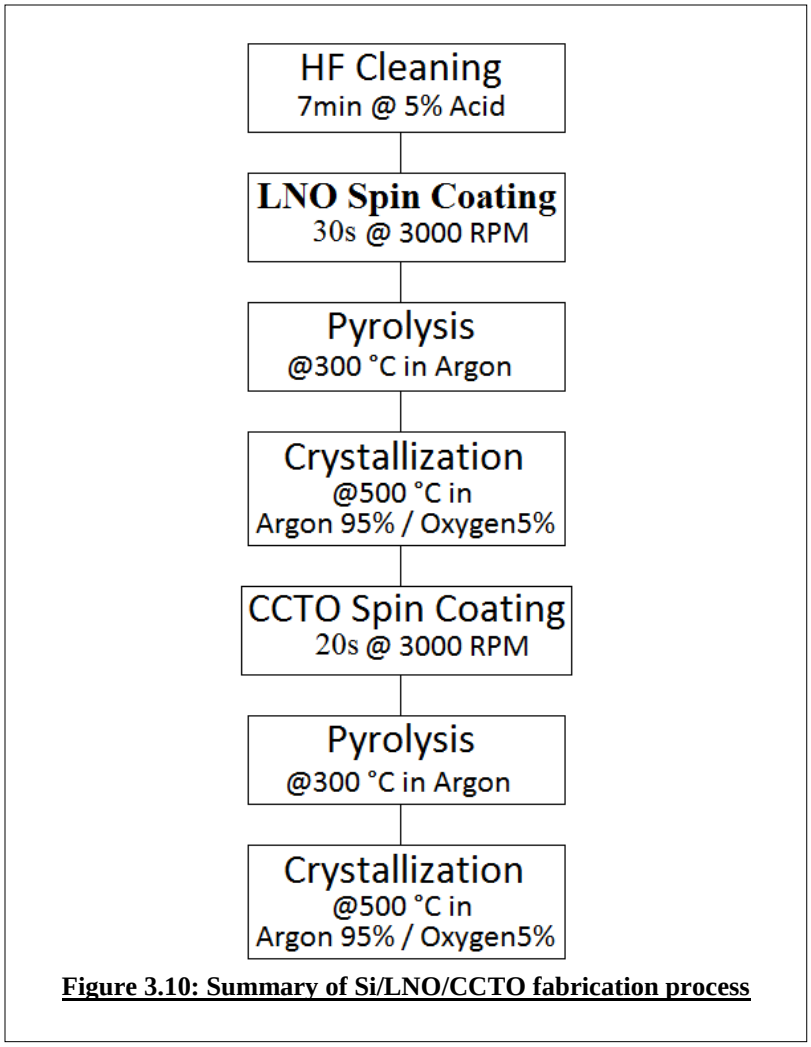

Figure 3.10: Summary of Si/LNO/CCTO fabrication process

C-V measurement result is illustrated in figure 3.11.

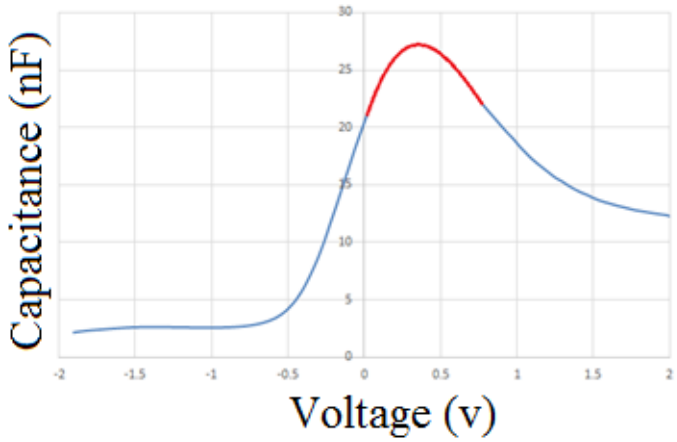

Figure 3.11: C-V measurement on Au/Si/LNO/CCTO/Au sample

The values above 20 nf are out of the measurement range of the employed C-V measurement instrument; So, it is indirectly measured using a series reference capacitor

The frequency stability results are compared as capacitance measurements of Si/LNO/CCTO and Si/CCTO/LNO coated samples in figure 3.12. This figure shows the capacitance variation range with the average value of the capacitance. The results show a high-frequency stability for Si/LNO/CCTO heterostructures at 3.25-3.5MHz.

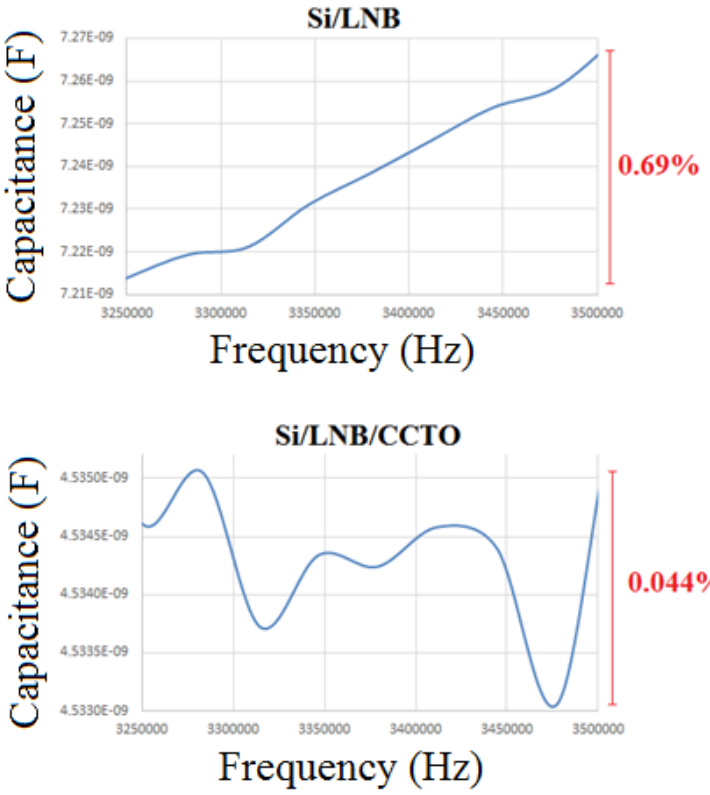

Figure 3.12: Si/LNO and Si/LNO/CCTO frequency dependent capacitance response

3.3 CCTO/LNO hetro-structure

The results show an improvement in the capacitance stability in a wide range of frequency Existing literature show that the dielectric properties of CCTO film can be improved when crystallized at temperatures far more than 500°C [70]. Annealing the Si/LNO/CCTO structure at temperatures above 500°C damages the structure with the presence of surface cracking. The issue is probably due to the differences in the coefficients of thermal expansion of the different materials. To solve this issue, the

CCTO films were deposited on the HF-treated wafer, crystallized at much higher temperature before deposition of the LNO film.

In the Si/CCTO/LNO structure, the CCTO film was deposited on the HF-cleaned substrate using spin coating recipe explained above. The sample, after the pyrolysis step, is annealed for 30 minutes at various temperatures from 700°C to 1000°C to identify the best crystal quality. In figure 3.13, the best XRD measurement result was processed at 900°C.

To verify the conditions for the best crystal quality, annealing was performed from 10 minutes to 2 hours. The results are shown in figure 3.14. The best CCTO growth was observed for 1hour annealing at 900°C. At this condition, XRD measurement results show polycrystalline CCTO formation with preferred (220) and (400) orientations. The reaction of oxygen with interfacial Si when annealing the sample at 900°C can be prevented by annealing the sample in the pure argon atmosphere or a using thicker layer of CCTO (over 100nm).

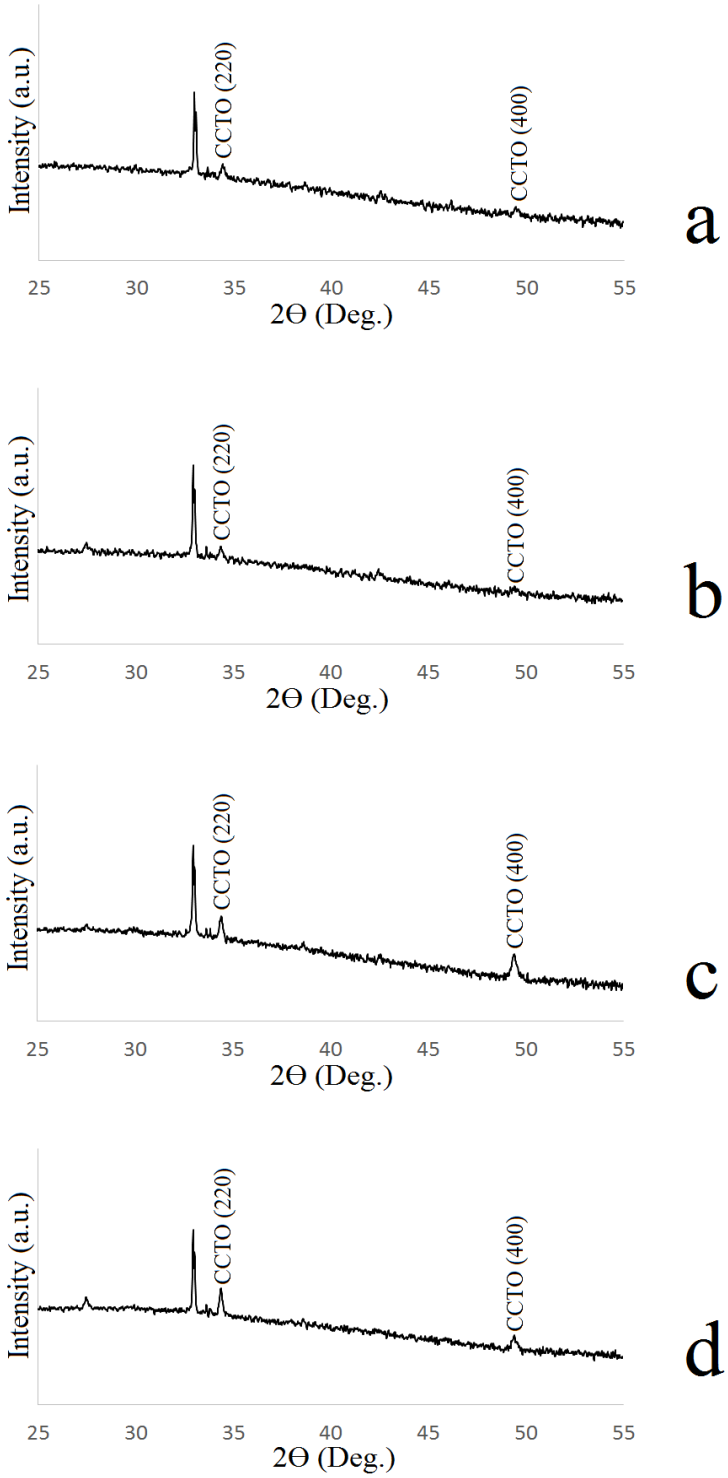

Figure 3.13: XRD measurement on Si/CCTO samples annealed at: a. 700°C, b. 800°C, c. 900°C, d. 1000°C

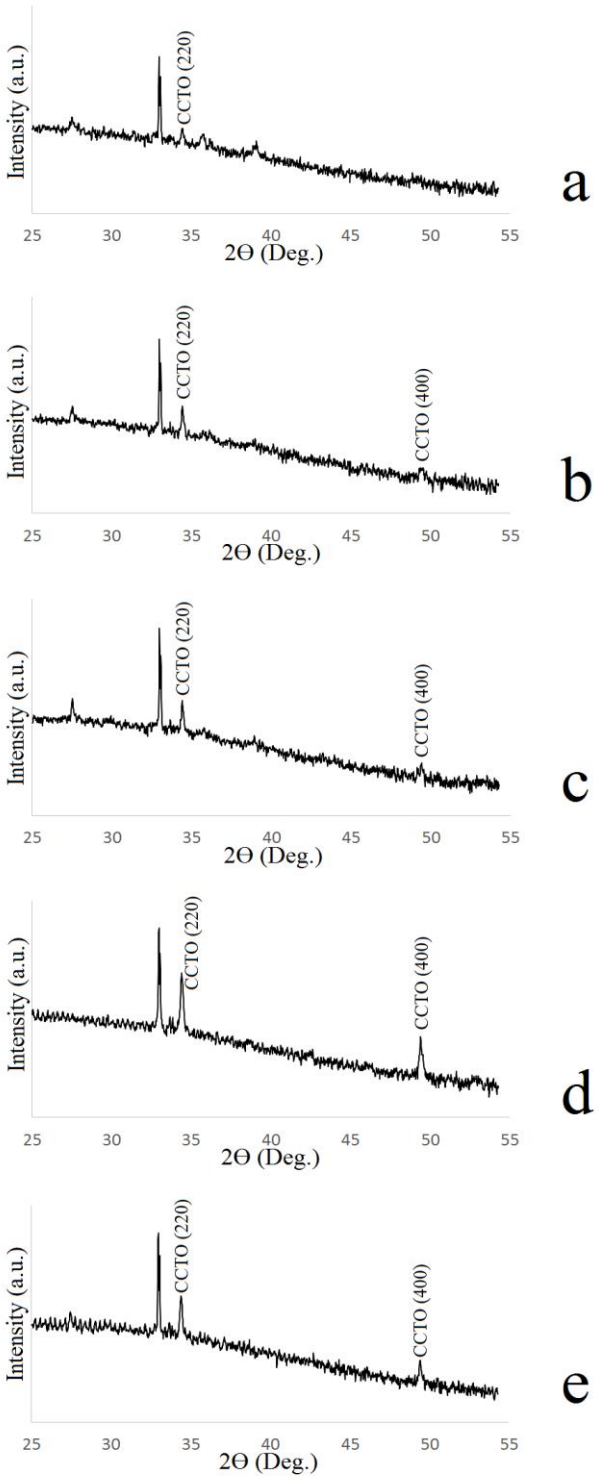

Figure 3.14: XRD measurement on Si/CCTO samples annealed at 900°C for: a. 10minutes, b. 20 minutes, c. 40 minutes, d. 1 Hour, e. 2 Hour

Ellipsometry measurement shows that a single spin deposition results in 29-30nm thick CCTO film on the Si substrate. The polycrystalline structure of the sample can be observed in SEM measurement illustrated in figure 3.15.

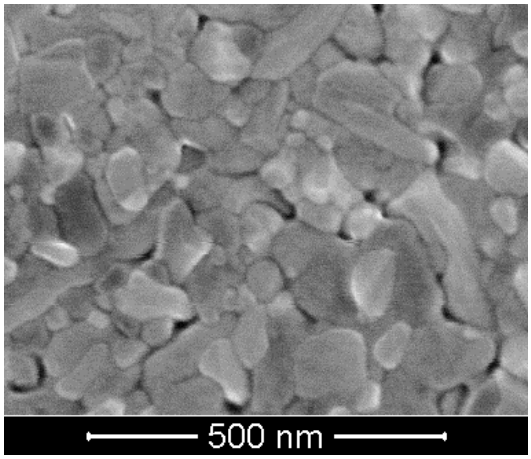

Figure 3.15: SEM measurement on polycrystalline CCTO deposited on Si

In order to improve the printing quality, the contrast and brightness of this image is modified

EDAX measurements, as illustrated in figure 3.16, shows the differences from ideal stoichiometric values.

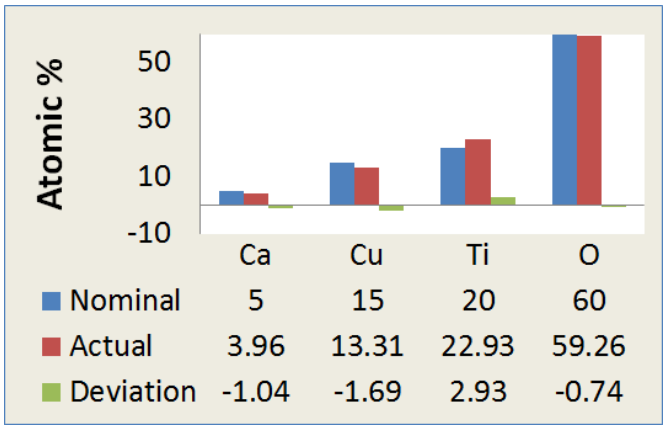

Figure 3.16: EDAX measurement results on polycrystalline CCTO deposited on Si

The sample was spin coated with LNO using the spin coating recipe explained above. The sample after pyrolysis was annealed at 450°C. XRD measurement results for Si/CCTO/LNO structure is illustrated in Figure 3.17.

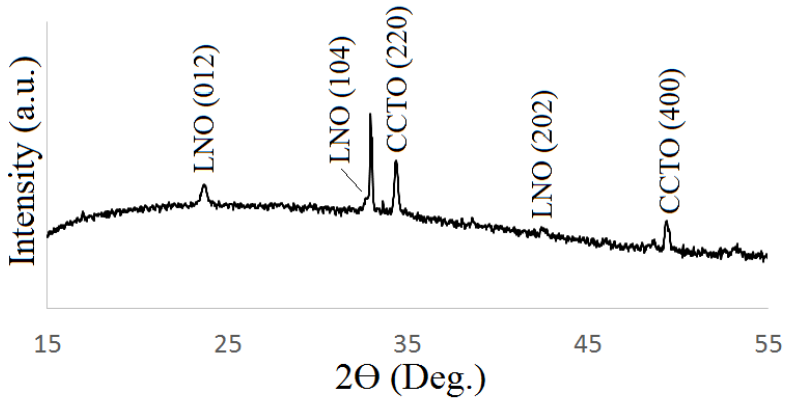

Figure 3.17: XRD measurement on Si/CCTO/LNO sample

XRD measurement results show the formation of polycrystalline LNO with a preferred orientation of (012). The summary of Si/CCTO/LNO fabrication process is illustrated in figure 3.18.

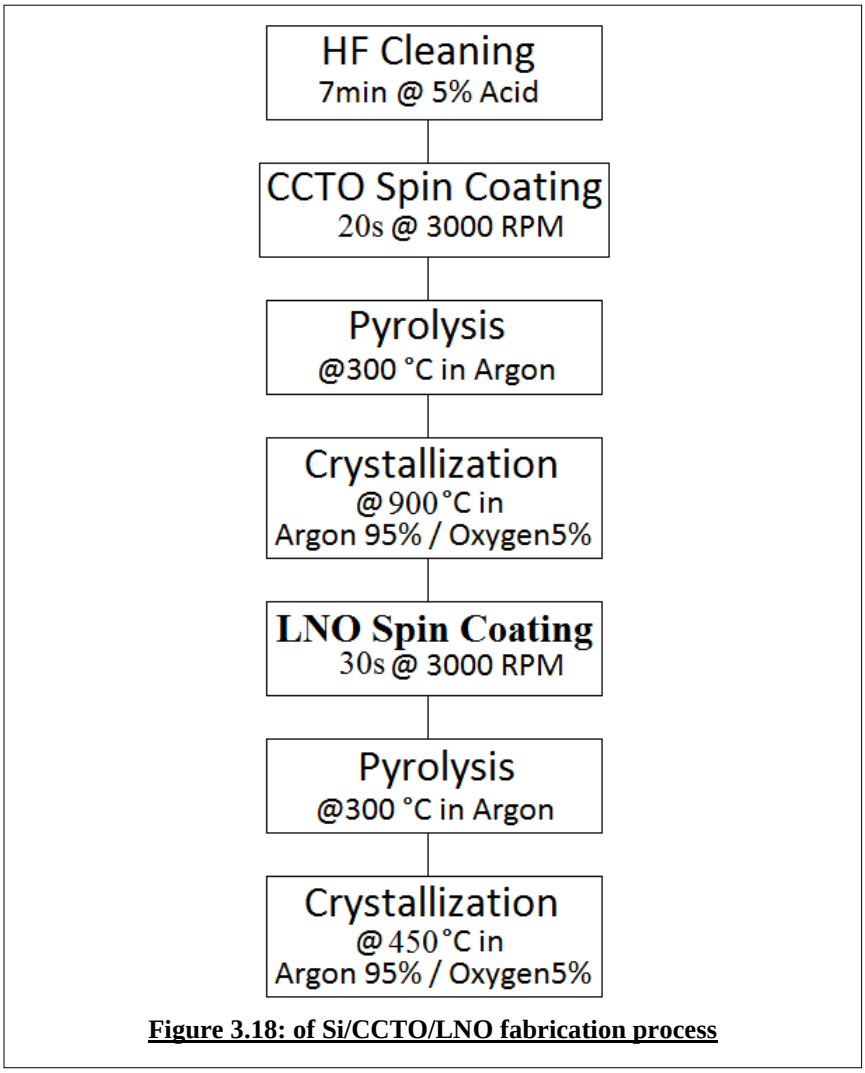

Figure 3.18: of Si/CCTO/LNO fabrication process

The result of the C-V characterization, illustrated in figure 3.17, shows the capacitance variation with the applied DC voltage.

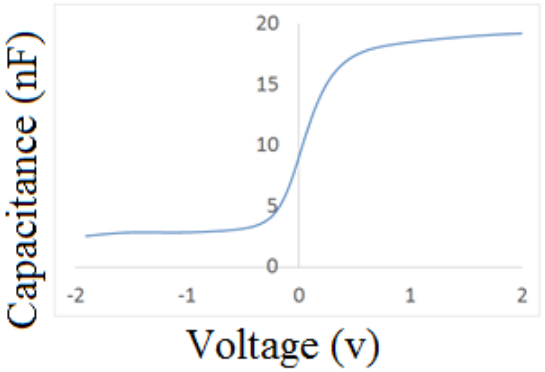

Figure 3.19: C-V measurement on Si/CCTO/LNO sample

To study the effect of CCTO and LNO film thickness ratio on the frequency stability of the Si/CCTO/LNO structure, three samples are made with 30nm CCTO film and 15nm, 60nm, and 120nm LNO layer. Thick LNO layers are made repeating the spin coating and solvent evaporation by annealing at 120°C for 5 minutes. LNO thickness is verified using ellipsometry. Capacitance-frequency measurements in figure 3.18 show the effect of LNO layer thickness on the capacitance minima position. The result shows a decrease in the frequency of the capacitance minima with increasing the thickness of the LNO film.

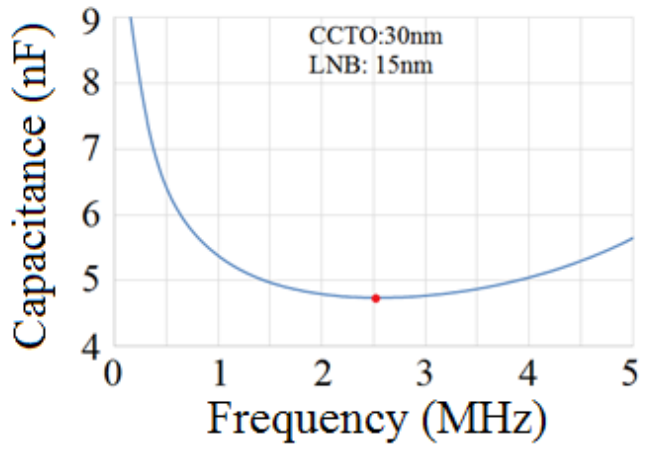

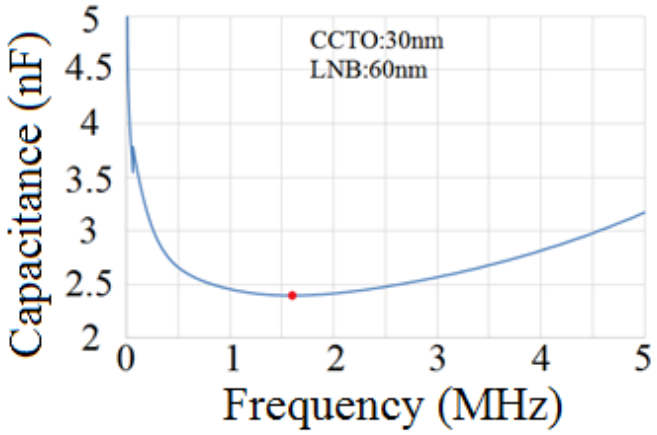

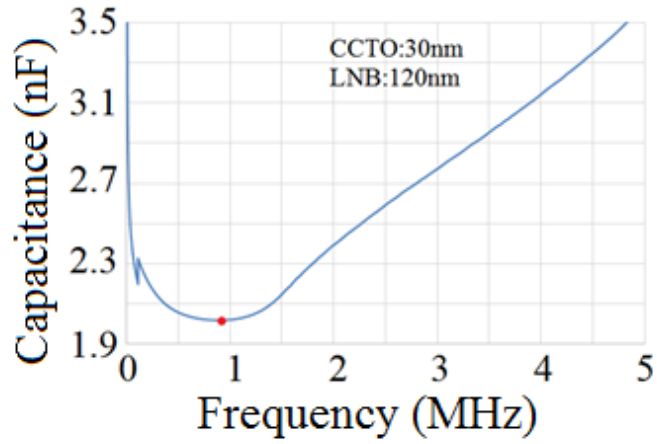

Figure 3.20: Capacitance measurement on CCTO/LNO structure

CHAPTER IV. CCTO/LNO UV TUNED CAPACITOR

4.1 Introduction

Tuning the dielectric constant of CCTO by manipulating the structure of grains and boundaries including varying the calcination or annealing temperature [71-73], sintering conditions [74-76], using additive materials [77-79], and employing novel sintering techniques including laser [80] and microwave [81-82]. Masingboon et. al. reported the variation of the dielectric properties of polycrystalline CCTO under UV light irradiation [83] are known. They reported an approximate 10% (at 100kHz) variation in the dielectric constant of polycrystalline CCTO under exposure of a 405nm laser with the intensity of 0.2 W/cm^2. An anomalous variation of dielectric constant under UV exposure can be employed for fabrication of dynamically tunable capacitors. Development of oxygen-vacancy induced states results in an induced metallicity at the surface of the material. This provides an increase in the conductivity of the CCTO under UV exposure via the chemical reaction [84]:

$$O \text{ (neutral)} \rightarrow V_o^{2+} \text{ (Oxygen Vacancy)} + 0.5\ O_2$$

Surface oxygen vacancies resulted from UV laser exposure explains the capacitance variation in CCTO layer. Semiconducting grain and insulating grain boundaries create an Internal Barrier Layer Capacitor (IBLC) that dominates the total film capacitance due to its small thickness [85].

The use of CCTO material as a UV tunable capacitor or UV detector has two challenges: temperature dependence and frequency dependence will limit the applications

of the fabricated device. At temperatures below 300°C, the increase in the dielectric constant of the CCTO with increasing temperature has been reported in many experimental studies on bulk and thin film CCTO [86-90]. The dielectric change as a function of temperature variation is comparable with the sensitivity of the CCTO-based tunable capacitors to UV light. It significantly affects the performance of the device.

The dielectric constant of the CCTO is a function of measurement frequency. Below 300°C, increasing the frequency up to 100kHz, decreases the dielectric constant of the CCTO [86, 90]. The frequency dependent UV sensitivity of CCTO-based capacitors is also reported in reference [83]. The capacitance, measured at 1kHz and 10 kHz, increases with UV exposure. The results are different at higher frequencies. A decrease in the capacitance under UV exposure at the measurement frequency of 100kHz was observed.

This chapter describes a mechanism to reduce the frequency and temperature dependence of the CCTO-based UV tunable capacitors employing an LNO layer. In reference [86], increasing the frequency from 100kHz to 1MHz above room temperature results an increase in the dielectric constant of the CCTO. This behavior is different for lower frequencies where the dielectric constant decreases with the frequency. At frequencies above 100kHz, the sensitivity of the CCTO capacitor to UV light is different that its behavior at lower frequencies. These two behaviors as a function of frequencies higher than 100kHz are different from the behavior of LNO.

The dielectric constant of LNO is decreasing with the increase of the frequency [91-93]. A combination of LNO and CCTO capacitors if selected with proper thickness

ratio can compensate the frequency dependence of the CCTO. The dielectric constant of the LNO is temperature dependent [91-94]. Close to room temperature, the dielectric constant of the LNO shows a very low dependence on the temperature variation especially in higher frequencies [91-94]. This can be used to compensate for a large temperature dependence of CCTO dielectric constant at high frequencies. The UV exposure can affect the dielectric constant of the LNO. An increase in the dielectric constant of the LNO has been reported by Makram et. al. [95].

4.2 PLD Deposition of CCTO/LNO Structure

Fabrication of CCTO/LNO for optical applications requires the deposition of high-quality films with precise thickness. To achieve a single crystal CCTO/LNO heterostructure, pulsed laser deposition technique is employed. Si substrates are used for the experiments. A thin layer of STO was deposited on Si as described in reference [96]. The deposition of CCTO films with preferred (100) orientation on (100) STO substrate has been reported by Feng et. al [97]. They employed the chemical solution deposition technique to deposit CCTO film. The sample after spin coating was transferred into a furnace preheated at 500°C for 10-minute pyrolysis step, followed by annealing at 850°C for 2 hours for crystallization.

There are reports on unsuccessful experiments on the direct deposition of CCTO on STO substrate using the PLD technique. W. Si et. al. [98] explained that a large lattice mismatch between CCTO (cubic, a/2=3.68 Å) and STO (cubic, a=3.905 Å) is the reason for an incorrect phase. A film consisted of more than one orientation of CCTO on the STO substrate deposited using PLD. They solved the issue using an $LaAlO_3$ (LAO)

buffer layer. There are several other reports on the deposition of epitaxial CCTO on LAO Using PLD [99-101]. Based on the literature, the process to fabricate CCTO/LNO hetero-structure starts with the deposition of LAO on Si/STO substrate. Epitaxial growth of (001) LAO on (001) STO employing the pulsed laser deposition technique has been reported [102-104].

The growth of LAO on PZT/STO was optimized by comparing different recipes. The direct growth of LAO on PZT/STO at 800°C results in extra phases. This was mitigated by depositing LAO at a lower temperature followed by post growth annealing at a higher temperature (800°C). The optimized recipe found for LAO growth was deposition at 400°C in 100 mTorr O_2 atmosphere using 2.7 J/cm^2 10Hz laser followed by post growth anneal of the sample at 800°C in 100 mTorr O_2 atmosphere for 20 minutes. The XRD measurement in figure 4.1 illustrates the difference between the LAO growth at high temperature and lower temperature with post-annealing at high temperature. The sample grown at high temperature shows more than one LAO phase while the sample grown at lower temperature with post-annealing at high temperature exhibits single crystal LAO with (001) orientation.

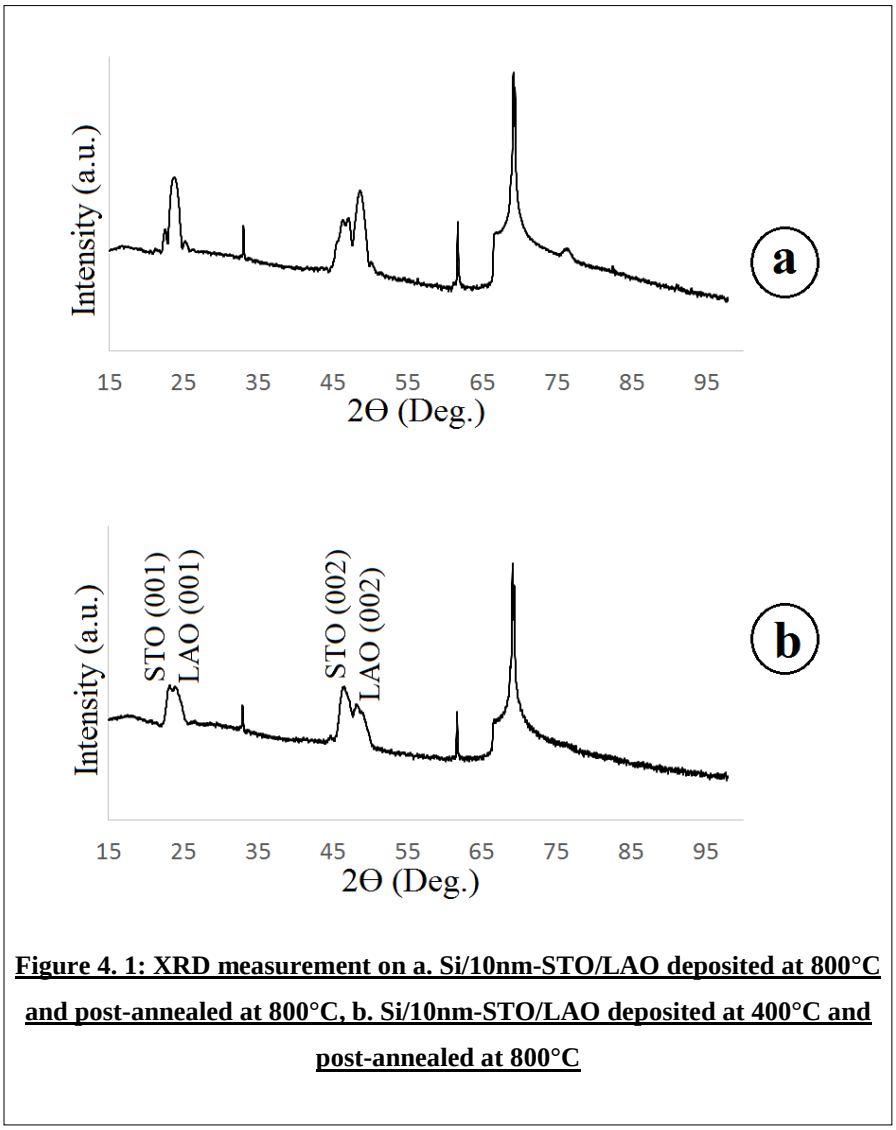

Figure 4. 1: XRD measurement on a. Si/10nm-STO/LAO deposited at 800°C and post-annealed at 800°C, b. Si/10nm-STO/LAO deposited at 400°C and post-annealed at 800°C

The growth of CCTO on Si/STO/LAO was optimized by exploring different recipes. The optimized recipe found for CCTO growth was deposition on 700°C in 100 mTorr O_2 atmosphere using 2.7 J/cm^2 10Hz laser. Then, post-annealing the sample at 700°C in 100 mTorr O_2 atmosphere for 30 minutes. The XRD measurement (figure 4.2) illustrates the formation of epitaxial CCTO with (001) orientation. The results show STO (001) and (002) peaks, LAO (001) and (002) peaks, and CCTO (002) and (004) peaks in addition to substrate (Si) peaks.

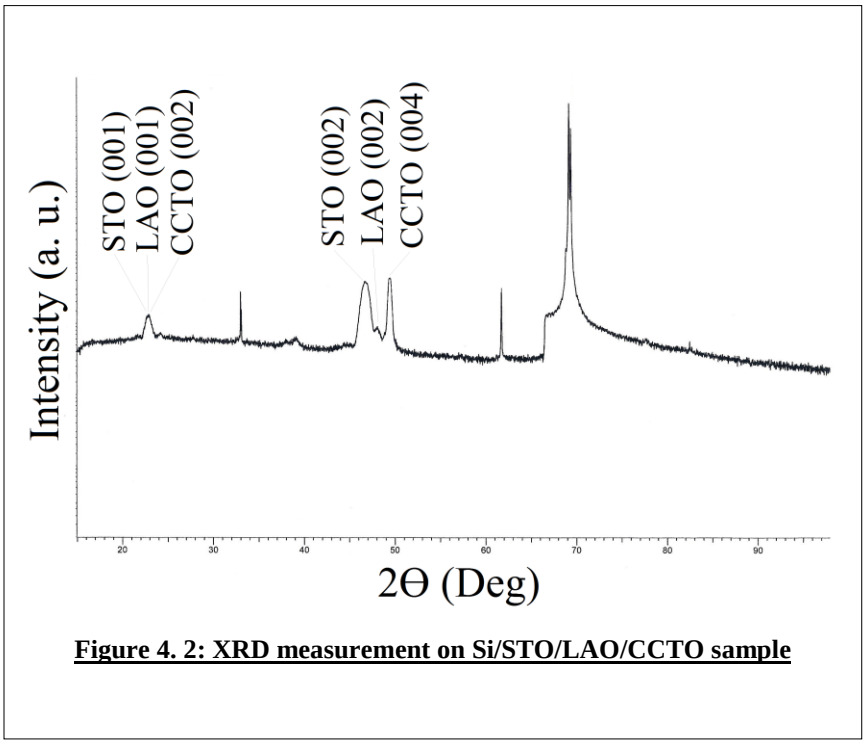

Figure 4. 2: XRD measurement on Si/STO/LAO/CCTO sample

Si/STO/LAO/CCTO sample was employed for electrical measurements and experiments to study the effect of UV exposure on CCTO capacitance. To perform the experimental study, Pt bottom electrodes were deposited by sputtering, and ITO top electrodes were deposited on top of the CCTO by PLD. The growth of ITO on Si/STO/LAO/CCTO was optimized by exploring the use of different recipes. The best recipe found for ITO (Sn/In + Sn = 10 %) growth was: deposition at 300°C in 10 mTorr O_2 atmosphere using 1.3 J/cm^2 10Hz laser. This was followed post-annealing the sample at 300°C in 10 mTorr O_2 atmosphere for 10 minutes. Petukhov et. al. [105] also reported an improvement in electrical conductivity of the ITO grown with the PLD technique when annealing at temperatures above 300°C in oxygen pressures in the range of 5–10 mTorr. The figure 4.3 illustrates the structure of the fabricated device for electrical measurements.

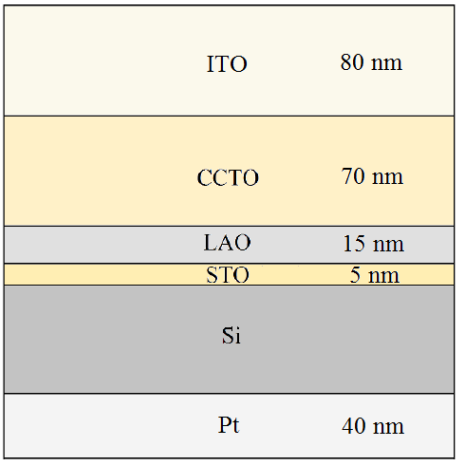

Figure 4. 3: The structure of fabricated 40nm-Pt/Si/5nm-STO/15nm-LAO/70nm-CCTO/80nm-ITO device for electrical measurements

The figure 4.4 shows the capacitance measurement for this sample in the frequency range of 100Hz-1MHz. The frequency-stable capacitance minima for this sample is about 150kHz. The sample was exposed to a 405nm laser with the intensity of 25mW/cm^2. This wavelength was chosen by considering the bandgap of ITO, which is about 3.8-4.2 eV [106-109] and the photon energy of 3.06 eV for a 405nm laser. ITO will transmit most of the laser light. As shown in figure 4.4, the sample shows an anomalous dielectric change under UV exposure. This experiment is performed at room temperature of 23°C.

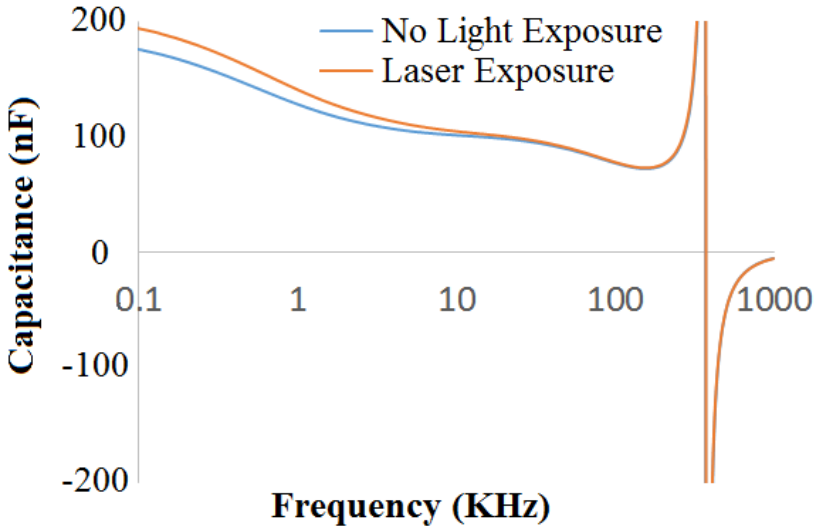

Figure 4. 4: Room temperature capacitance measurement on the fabricated 40nm-Pt/Si/5nm-STO/15nm-LAO/70nm-CCTO/80nm-ITO device in dark ambient and under laser exposure

To understand the light sensitivity of epitaxial CCTO, the percentage increase in the capacitance of the device under laser exposure is plotted in figure 4.5. The measurement was performed at the proximity of the frequency-stable capacitance minima.

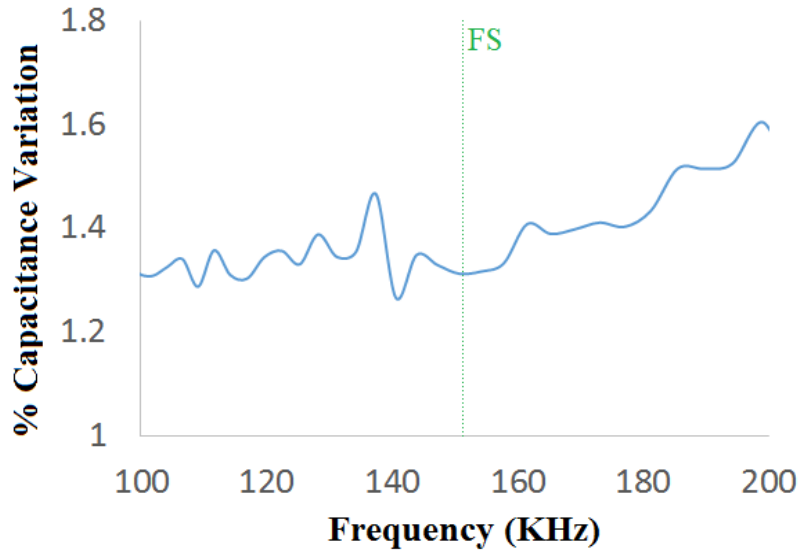

Figure 4. 5: Percentage increase in the capacitance of the fabricated 40nm-Pt/Si/5nm-STO/15nm-LAO/70nm-CCTO/80nm-ITO device under laser exposure

The fabricated device shows about 1.3% capacitance increase at 100kHz under exposure of a 405nm laser with the intensity of 25mW/cm^2. This result is comparable with the sensitivity of polycrystalline CCTO. An increase of up to 10% in the capacitance at frequencies of 100kHz was observed in the polycrystalline CCTO under exposure of a 405nm laser with the intensity of 200mW/cm^2 [83].

The effect of the ambient temperature on the performance of this device can be observed by comparing the capacitance at room temperature with the capacitance at the elevated temperature of 50°C. The results of this experiment are shown in figure 4.6 and is measured in the dark.

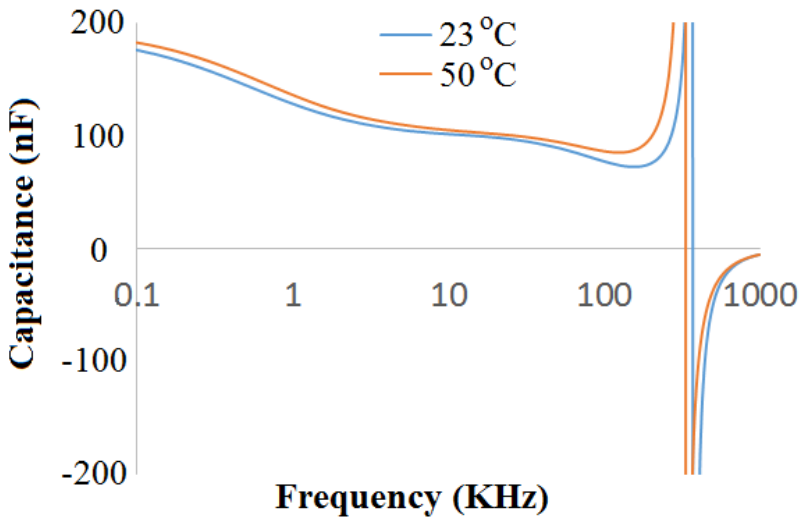

Figure 4. 6: Capacitance measurement on the fabricated 40nm-Pt/Si/5nm-STO/15nm-LAO/70nm-CCTO/80nm-ITO device in dark ambient at room temperature and elevated temperature

To understand the temperature sensitivity of the fabricated device, the percentage increase in the capacitance of the device per °C temperature increase is plotted in figure 4.7. The measurement was performed at the proximity of the frequency-stable capacitance minima.

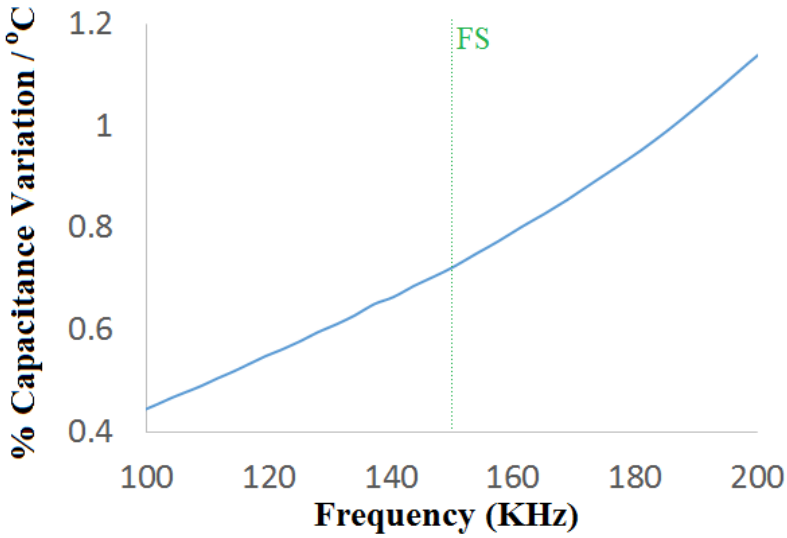

Figure 4. 7: Percentage increase in the capacitance of the fabricated 40nm-Pt/Si/5nm-STO/15nm-LAO/70nm-CCTO/80nm-ITO device per °C temperature increase

This result shows a high-temperature sensitivity for the fabricated device when compared to its light sensitivity values. For an example, just 1°C temperature variation in the ambient, results about 35% measurement error in capacitance variation at 100kHz under the exposure of a 405nm laser with the intensity of 25mW/cm^2. The temperature effect becomes more challenging knowing the fact that the light sensitivity of the capacitor is changing with temperature. The result is a decrease in the light sensitivity of the device with increasing the temperature. The measurement was performed at the proximity of the frequency-stable capacitance minima.

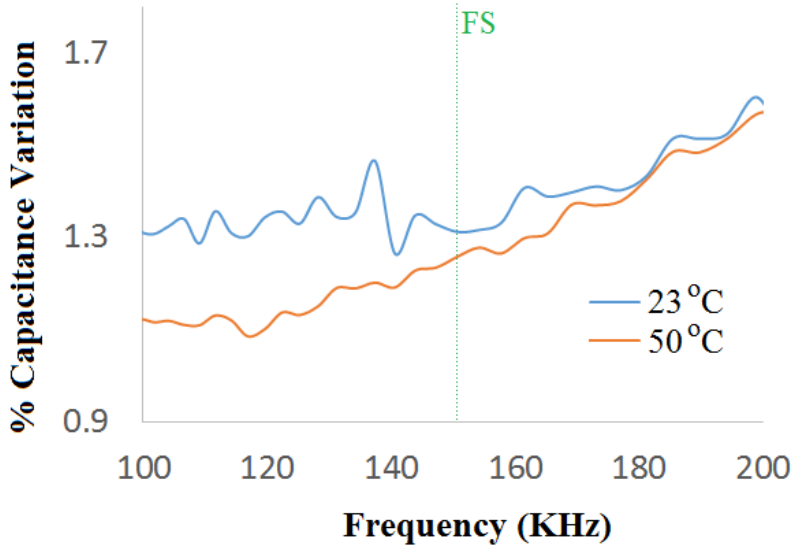

Figure 4. 8: Percentage increase in the capacitance of the fabricated 40nm-Pt/Si/5nm-STO/15nm-LAO/70nm-CCTO/80nm-ITO device under laser exposure in different temperatures

The growth of LNO on Si/STO/LAO/CCTO was optimized by using different recipes. The best recipe found for LNO growth was deposition at 600°C in 100 mTorr O_2 atmosphere using 1.3 J/cm^2 10Hz laser. The sample was post-annealed at 600°C in 100 mTorr O_2 atmosphere for 30 minutes. The XRD measurement in figure 4.9 illustrates the formation of epitaxial LNO with (001) orientation. The results show STO (001) and (002) peaks, LNO (012) and (024) peaks, and CCTO (002) and (004) peaks in addition to substrate (Si) peaks. The LAO peaks, because of the low thickness of LAO layer compared to LNO, are not clearly observed in this measurement.

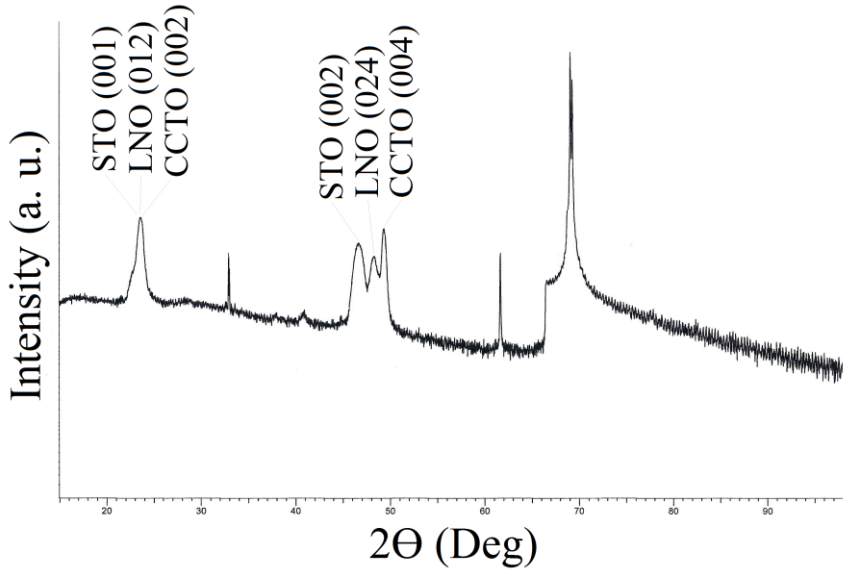

Figure 4. 9: XRD measurement on Si/STO/LAO/CCTO/LNO sample

The TEM measurement in the figure 4.10 illustrates a sharp CCTO/LNO interface. The EDS scan shows that there is no intermixing at the hetero-interface.

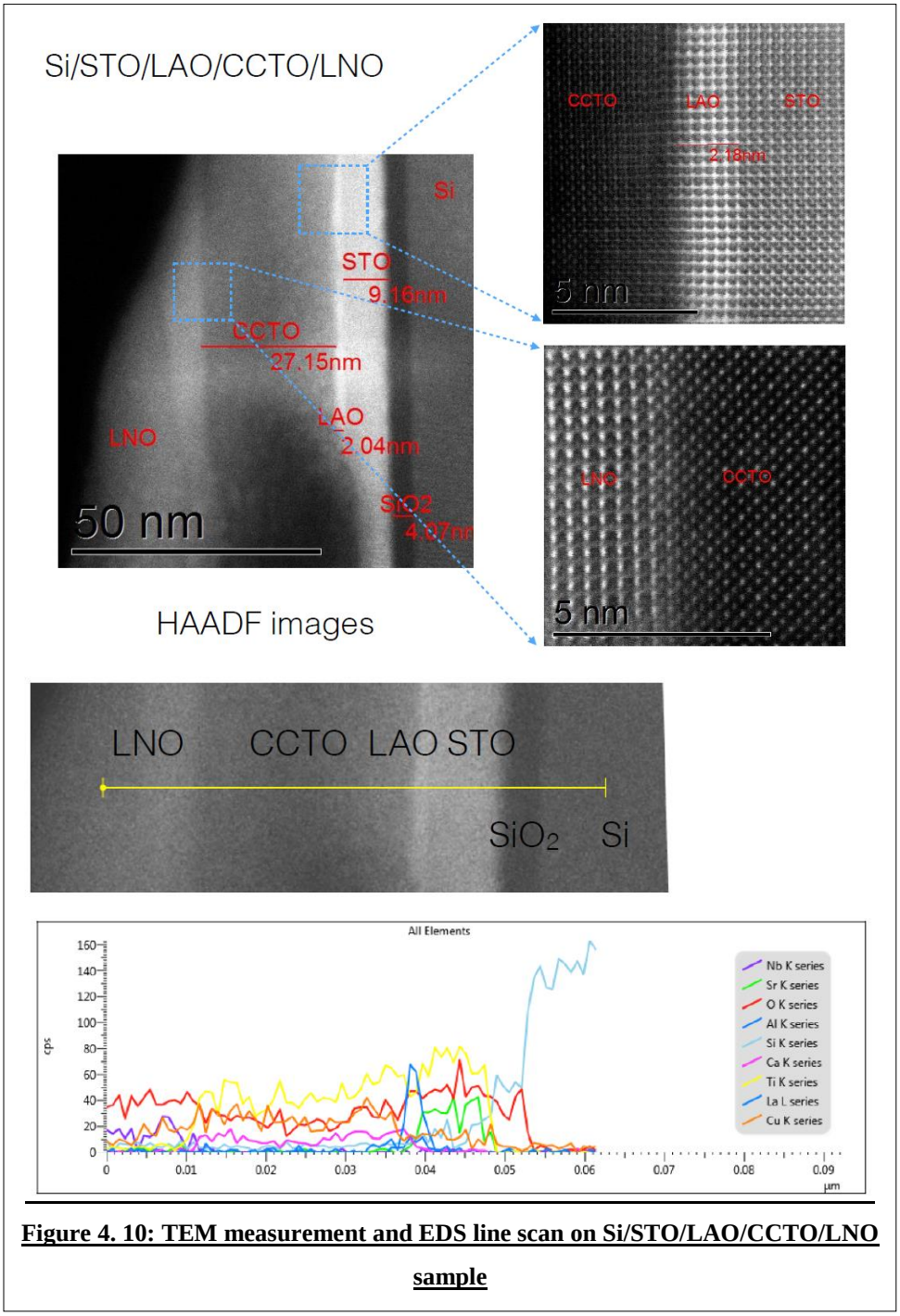

Figure 4. 10: TEM measurement and EDS line scan on Si/STO/LAO/CCTO/LNO sample

The Si/STO/LAO/CCTO/LNO sample was employed for electrical measurements and experiments to study the effect of UV exposure on CCTO/LNO capacitance. Pt bottom electrodes are deposited by sputtering, and ITO top electrodes are deposited on

top of the CCTO by PLD. ITO (Sn/In + Sn = 10 %) was deposited on 300°C in 10 mTorr O_2 atmosphere using 1.3 J/cm^2 10Hz laser followed post growth annealing at 300°C in 10 mTorr O_2 atmosphere for 10 minutes. Figure 4.11 illustrates the structure of the fabricated device for electrical measurements.

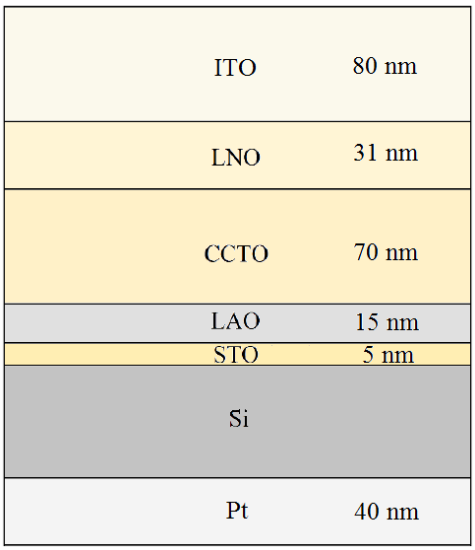

Figure 4. 11: The structure of fabricated 40nm-Pt/Si/5nm-STO/15nm-LAO/70nm-CCTO/31nm-LNO/80nm-ITO device for electrical measurements

Figure 4.12 shows the capacitance measurement on this sample in the frequency range of 100Hz-1MHz. The frequency-stable capacitance minima for this sample is about 180kHz. The sample was exposed to a 405nm laser with the intensity of 25mW/cm^2. As shown in figure 4.12, the sample shows an anomalous dielectric change under UV exposure. This experiment is performed at 23°C.

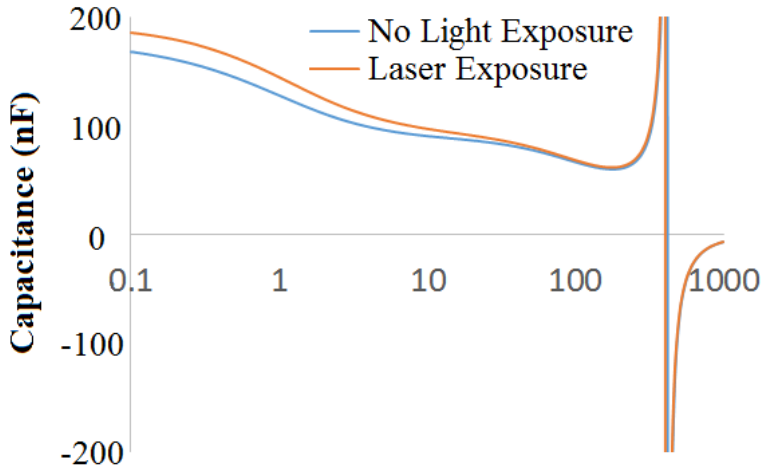

Figure 4. 12: Room temperature capacitance measurement on the fabricated 40nm-Pt/Si/5nm-STO/15nm-LAO/70nm-CCTO/31nm-LNO /80nm-ITO device in dark ambient and under laser exposure

To have a better understanding of the light sensitivity of epitaxial CCTO, the percentage increase in the capacitance of the device under laser exposure is plotted in figure 4.13. The measurement was performed at the proximity of the frequency-stable capacitance minima.

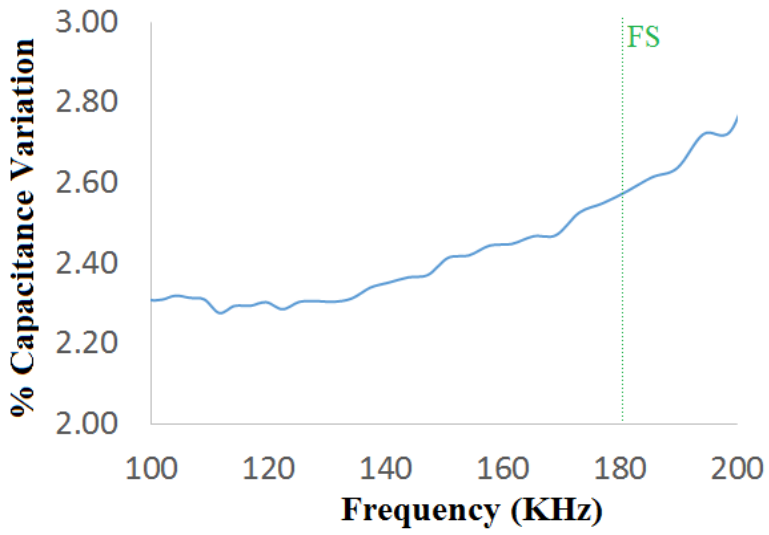

Figure 4. 13: Percentage increase in the capacitance of the fabricated 40nm-Pt/Si/5nm-STO/15nm-LAO/70nm-CCTO/31nm-LNO /80nm-ITO device under laser exposure

The CCTO/LNO capacitor shows about two times more sensitivity to the laser exposure at the frequency-stable region when compared with the percentage increase in the capacitance of CCTO under UV exposure.

The effect of the ambient temperature on the performance of this device can be observed by comparing the capacitance at room temperature and the capacitance at the elevated temperature of 50°C. This experiment, as shown in figure 4.14, is performed in the dark.

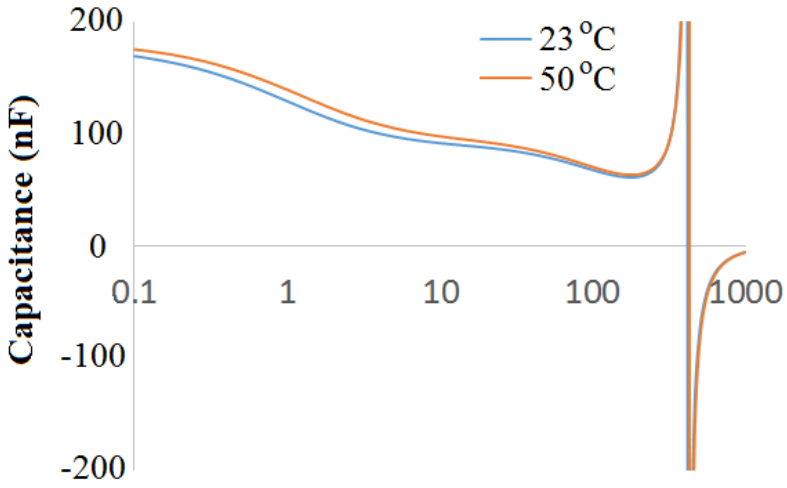

Figure 4. 14: Capacitance measurement on the fabricated 40nm-Pt/Si/5nm-STO/15nm-LAO/70nm-CCTO/31nm-LNO /80nm-ITO device in dark ambient at room temperature and elevated temperature

To understand the temperature sensitivity of the fabricated device, the percentage increase in the capacitance of the device as a function of °C temperature increase is plotted in figure 4.15. The measurement was performed at the proximity of the frequency-stable capacitance minima.

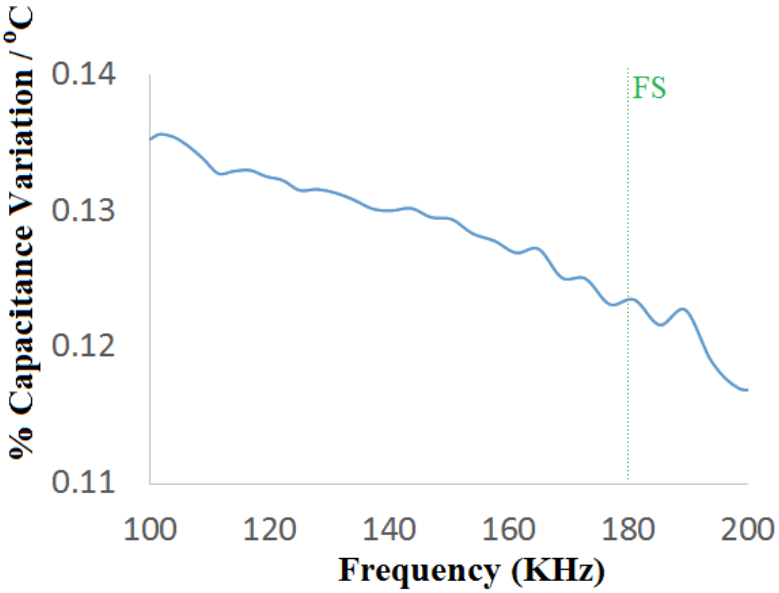

Figure 4. 15: Percentage increase in the capacitance of the fabricated 40nm-Pt/Si/5nm-STO/15nm-LAO/70nm-CCTO/31nm-LNO /80nm-ITO device per °C temperature increase

The CCTO/LNO capacitor shows about six times less sensitivity to the temperature variation at the frequency-stable region when compared with the percentage increase in the capacitance of CCTO. The light sensitivity of the CCTO/LNO capacitor at the proximity of the frequency stabled area, as shown in figure 4.16, is almost independent of the temperature variation.

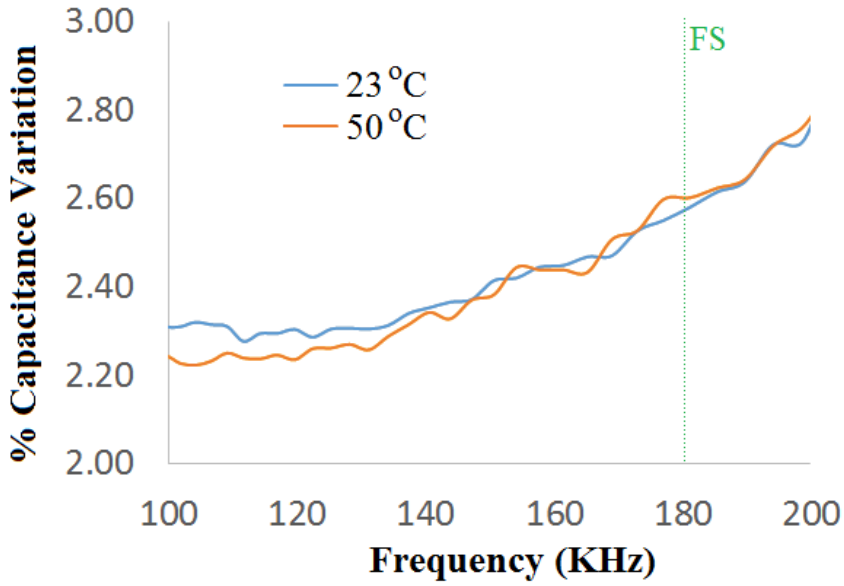

Figure 4. 16: Percentage increase in the capacitance of the fabricated 40nm-Pt/Si/5nm-STO/15nm-LAO/70nm-CCTO/31nm-LNO /80nm-ITO device under laser exposure in different temperatures

CHAPTER V. PULSED LASER DEPOSITION OF PZT ON Si

5.1. Introduction

Techniques employed for PZT deposition, include: Sol-gel [110-113] deposition, Ink Jet Printing [114], Sputtering [115-118], Chemical Vapor Deposition [119-122] (CVD), and Pulsed Laser Deposition (PLD) [123-125]. PLD is a cost-effective, high quality film deposition of a variety of complex compounds including PZT. PLD deposition is based on target material vaporization in plasma plume and its stoichiometric transfer to the substrate. PLD is more challenging when depositing materials that include volatile elements such as lead. A significant decrease in the lead content is achieved by increasing the temperature of the substrate above 630°C [126, 127]. The most common way to compensate for this issue is using a PZT target with more Pb content. Lead depletion in PLD deposition of PZT has been reported in 2010 [128, 129]. Mukherjee et. al. reported a decrease in the Pb ratio of the PZT target when the laser flux was increased. They observed a saturation in the Pb content at fluxes above $3J/cm^2$. The Zr and Ti ratios remain almost constant in their experiments.

This chapter reports the issue of Pb depletion in PLD deposition of PZT under a wide range (10mT-400mT) of oxygen background pressure. The chapter also shows a mechanism to control the Zr/Ti ratio of the PZT film using the pressure of the oxygen during the deposition.

Zr/Ti or Zr/Zr+Ti ratio are important parameters affecting the electrical properties of PZT. Yokoyama et. al [130] explained the effect Zr/Zr+Ti ratio on the remnant

polarization and coercive field of the deposited PZT films. Lonkar et. al. [131] reported that the decrease in the Zr/Ti ratio results in the increase of the dielectric constant and a decrease in the dielectric losses. They observed variation of the piezoelectric charge constant and piezoelectric voltage constant with the change of the Zr/Ti ratio. In this chapter the electrical properties of PZT films deposited using the oxygen pressure as a control parameter for Zr/Zr+Ti ratio are compared.

5.2. Deposition of PZT using PLD Technique

PZT target with the chemical compound of $Pb_{1.1}Zr_{0.53}Ti_{0.47}O_3$ manufactured by PLASMA-MATERIALS is used in this study. As illustrated in figure 5.1, The XRD measurement on the clean (mechanically polished) PZT target shows the polycrystalline PZT with minor ZrO_2 and PbO phases.

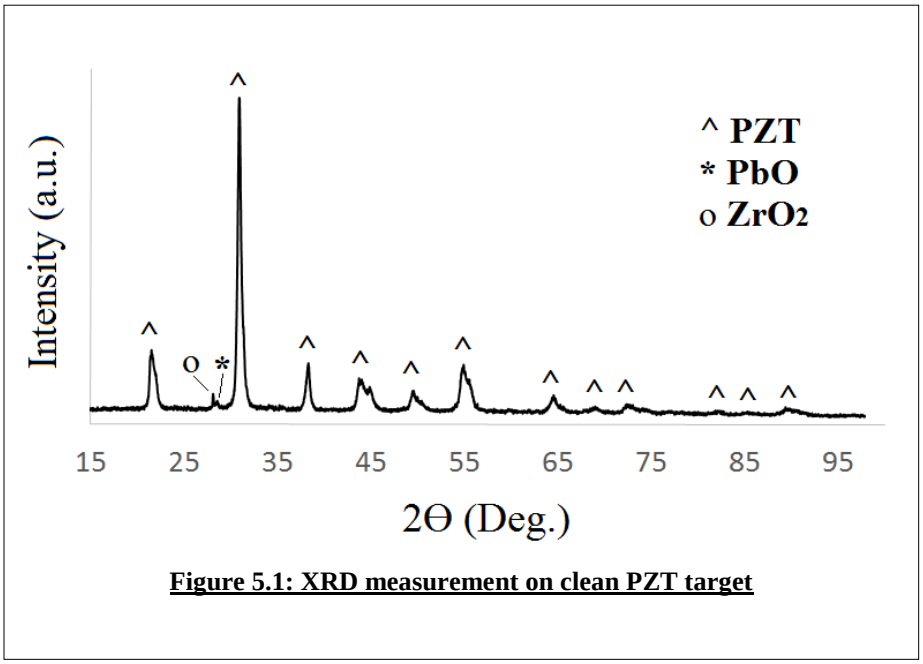

Figure 5.1: XRD measurement on clean PZT target

EDAX analysis of the target material also showed the differences from ideal stoichiometric values (see Figure 5.2).

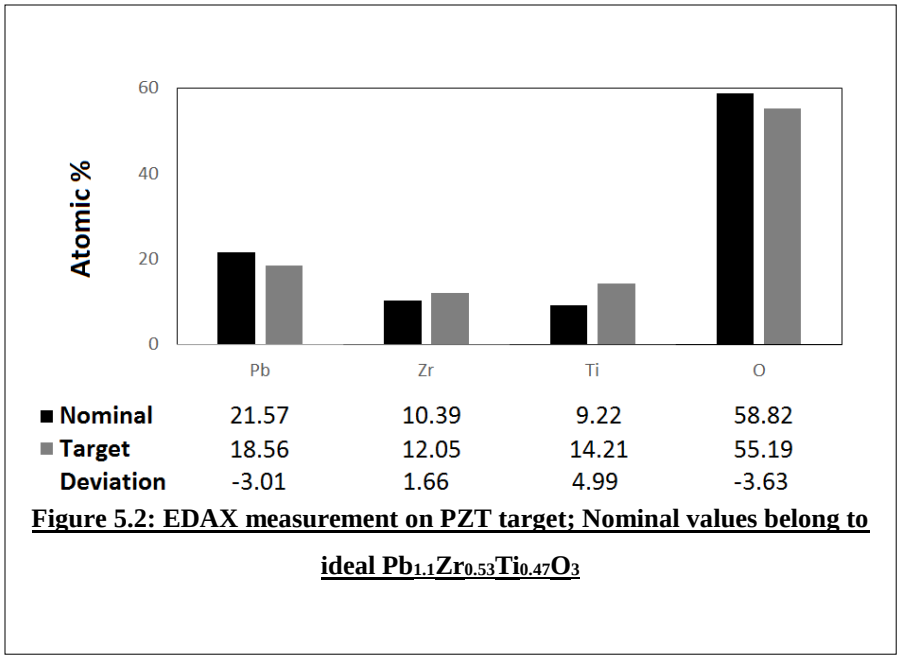

	Pb	Zr	Ti	O
Nominal	21.57	10.39	9.22	58.82
Target	18.56	12.05	14.21	55.19
Deviation	-3.01	1.66	4.99	-3.63

Figure 5.2: EDAX measurement on PZT target; Nominal values belong to ideal $Pb_{1.1}Zr_{0.53}Ti_{0.47}O_3$

When the target is exposed to the Nanosecond UV laser, the color of the PZT target surface is changed to dark gray, and the structure of its surface is modified. The XRD measurement of the target, as shown in the figure 5.3, shows the presence of Pb, ZrO_2, and PbO after exposure to 10Hz, 1j/cm^2 laser beam for 10 minutes in O_2 (Figure 5.3.a) and Ar (Figure 5.3.b) atmosphere with the pressure of 100mT. The measurement clearly shows that the ratio of the PbO to Pb is increased in the presence of O_2.

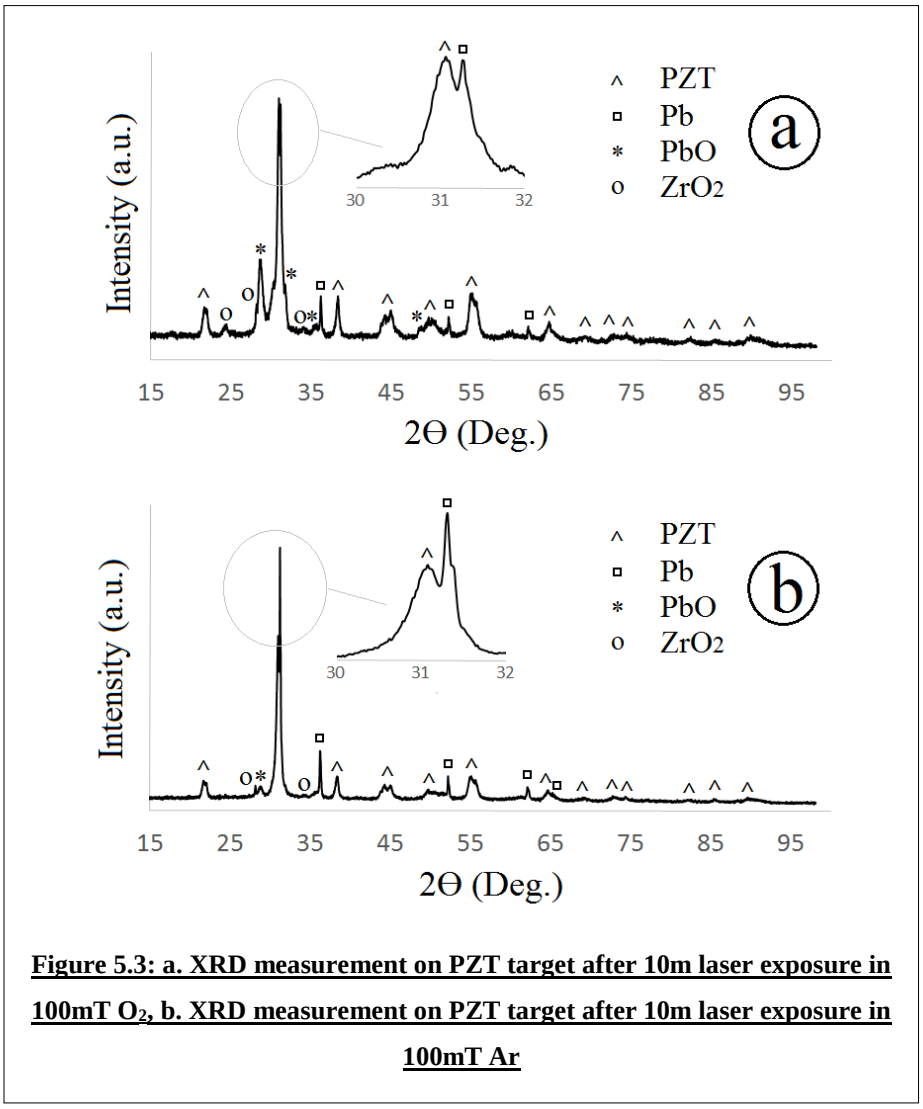

Figure 5.3: a. XRD measurement on PZT target after 10m laser exposure in 100mT O_2, b. XRD measurement on PZT target after 10m laser exposure in 100mT Ar

The XRD results predicted that the deposited PZT films have Pb and Zr depletion. To verify this prediction, the PZT films grown using different laser energy are analyzed with EDAX. 200nm of PZT film is deposited on HF-cleaned Si wafer at the temperature of 100°C. The experiments were carried out in an oxygen atmosphere of 100mT. This can potentially be an issue with using an O_2 exposed PZT target for the initial growth of PZT thin films using PLD.

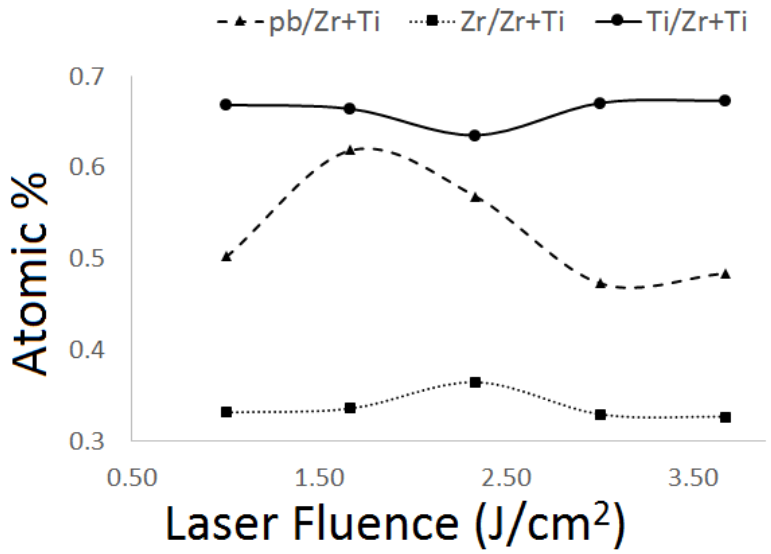

Figure 5.4: EDAX measurement on PZT target, PZT film grown under exposure of 248nm 10Hz laser with different fluxes

The EDAX measurements of figure 5.4 clearly show maxima for Pb/Zr+Ti ratio about 1.7 J/cm^2. The lead content is saturating at fluxes above 3J/cm^2. Zr/Zr+Ti and Ti/Zr+Ti ratios have a small variation in different laser fluxes.

Figure 5.5 below illustrates the variation of Pb/Zr+Ti, Zr/Zr+Ti, and Ti/Zr+Ti of deposited PZT films employing 1.7 J/cm^2 laser at different oxygen pressures.

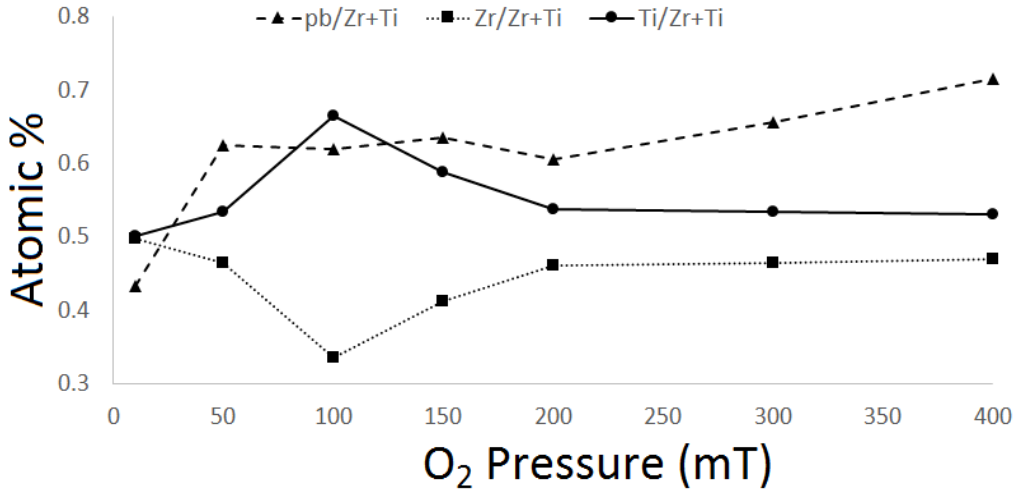

Figure 5.5: EDAX measurement on PZT films grown using 248nm, 10Hz 1.7 J/cm^2 laser at different oxygen pressures

In an oxygen ambient above 200mT, the Pb/Zr+Ti content is increased with an increase in the pressure. The Zr/ Zr+Ti and Ti/ Zr+Ti ratio is almost uniformFor oxygen pressure below 200mT, the Zr/ Zr+Ti and Ti/ Zr+Ti ratio is changing with the change of the atmosphere pressure. The Pb/ Zr+Ti ratio is almost the same from 50mT to 200mT. Two important facts can be concluded from this observation: (i) An increase in the oxygen pressure is required to deposit PZT films with high lead content [128,129]. The EDAX measurement results as illustrated in Figure 5.6 indicates the similarity between the elements of the film grown in 400mT O_2 and the target. (ii) The Zr/Ti or Zr/Zr+Ti ratio which is an important parameter affecting the electrical properties of PZT [130-131] can be tuned by oxygen pressure when pressure is below 200mT.

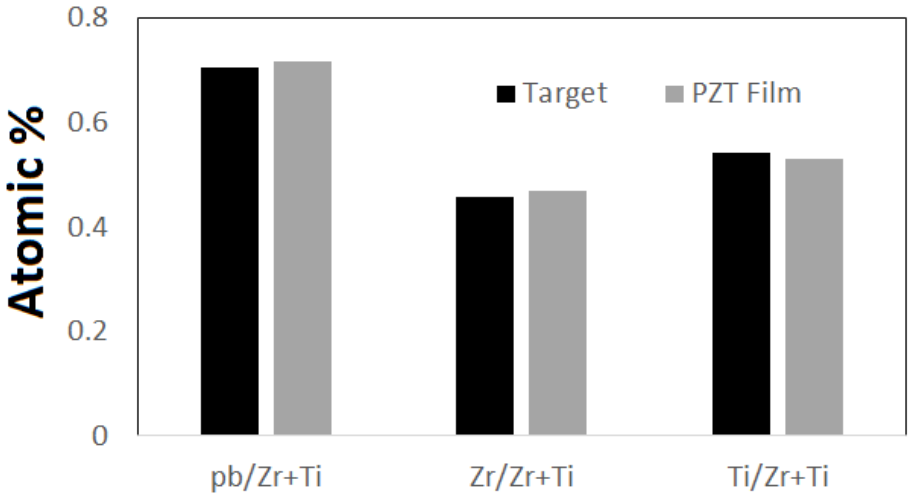

Figure 5.6: EDAX measurement comparing the PZT target and the PZT film grown on 400mT oxygen atmosphere using 1.7 J/cm^2 laser.

To verify the tunability of the PZT properties, three samples were prepared using the identical growth parameters except oxygen pressure. XRD measurements as shown in figure 5.8, illustrate the formation of (001) PZT on the Si/5nm-STO/30nm-SRO substrate. Single crystalline SRO with (001) orientation, as shown in figure 5.7.a, was deposited in the oxygen atmosphere with the pressure of 300mT using 10Hz laser with the flux of 1.7 J/cm^2. The high angle XRD measurement on the 40nm single crystalline PZT (001) deposited on SRO layer is illustrated in figure 5.7.b. The tunability of the PZT lattice constant varying the oxygen pressure is verified using the oxygen pressure of 100mT (Figure 5.7.c), 125mT (Figure 5.7.d), and 150mT (Figure 5.7.e). Combining the EDAX measurement results shown in figure 5.6 with the reported results on the lattice constant of the PZT as a function of Zr/Zr+Ti ratio [131], an approximate lattice constant (a) variation of 3.96Å-4.02Å is expected.

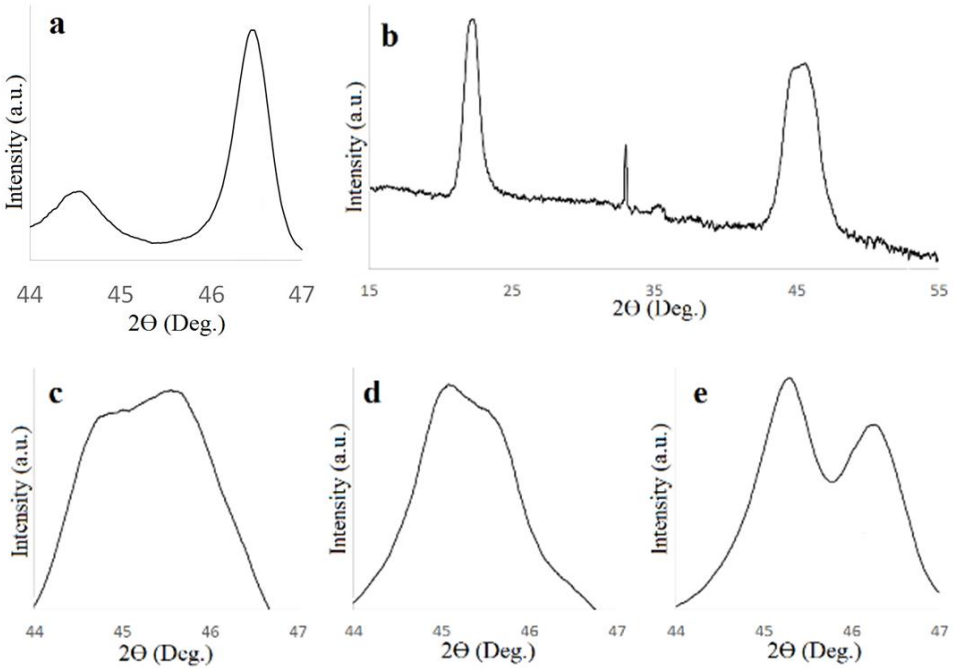

Figure 5.7: a. XRD measurement on: a. Si/5nm-STO/30nm-SRO sample, b. Si/5nm-STO/30nm-SRO/40nm-PZT sample grown in oxygen pressure of 100mT, c. Si/5nm-STO/30nm-SRO/40nm-PZT sample grown in oxygen pressure of 100mT, d. Si/5nm-STO/30nm-SRO/40nm-PZT sample grown in oxygen pressure of 125mT, e. Si/5nm-STO/30nm-SRO/40nm-PZT sample grown in oxygen pressure of 150mT.

Capacitance and P-E measurements were carried out on four Si/STO/PZT samples with 40nm PZT films deposited using 10Hz, 248nm 1.7 J/cm^2 laser in Oxygen ambient with the pressure of 125mT, 150mT, 175mT, and 200mT employing Pt electrodes.

The capacitance measurement was carried out at 1kHz. The results show a decrease in the dielectric constant by increasing the pressure of the oxygen during the growth. The loss factor, Tan δ, is also increasing with the increase of the O_2 pressure. The

relative dielectric constant, as shown in figure 5.8, can be controlled in the range of 29-130 when changing the oxygen pressure from 200mT-125mT.

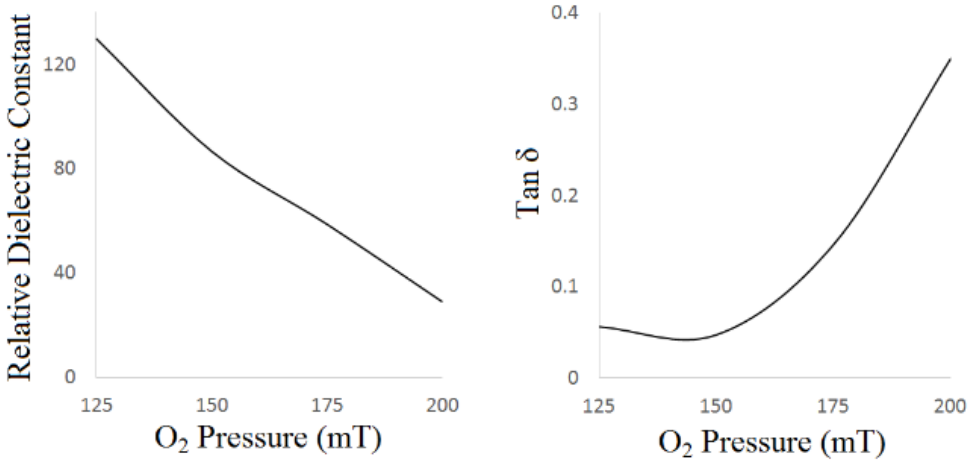

Figure 5.8: Tuning the relative dielectric constant and Tan δ in PZT films grown on different oxygen pressures

The P-E measurements as shown in figure 5.9 are carried out using two top Pt electrodes. The results show a wider hysteresis loop at higher oxygen pressure. The P-E measurement shows an increase in the P_r value when increasing the oxygen pressure during the PZT growth. The P_r can be tuned in the range of 6.6 μC/cm^2 to 42.2 μC/cm^2 varying the oxygen pressure from 125mT to 200mT. Figure 5.9.e illustrates the P_r/P_{sat} value that is increasing when increasing the oxygen pressure.

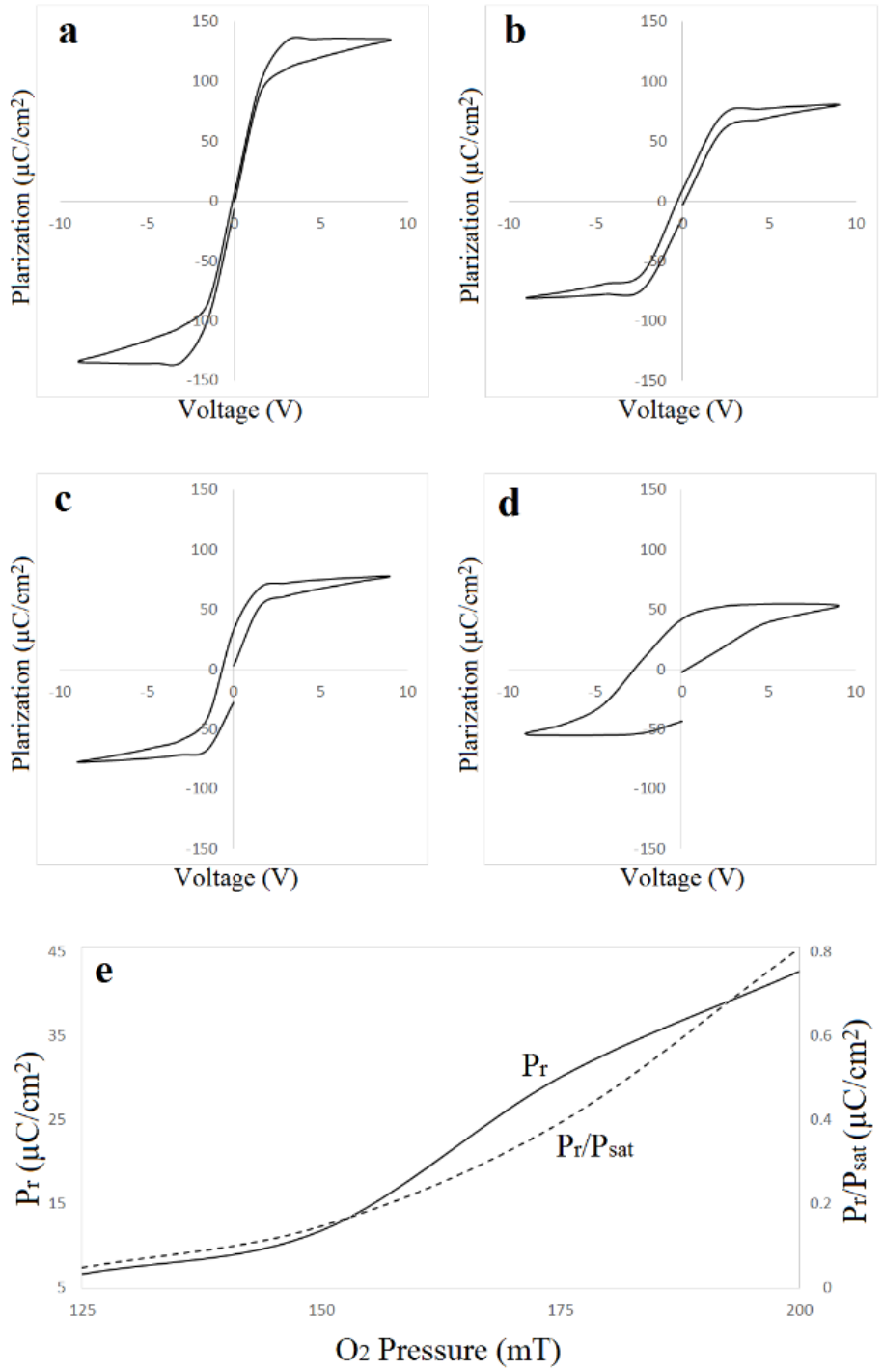

Figure 5. 9: P-E measurement on PZT films deposited on Si/STO substrate using 10Hz, 248nm 1.7 J/cm^2 laser in Oxygen ambient with pressure of a. 125mT, b. 150mT, c. 175mT, d. 200mT, e. Pr and Pr/Psat value versus the Oxygen pressure.

CHAPTER VI. DEPOSITION OF FERROELECTRIC THIN FILMS ON III-V SEMICONDUCTORS

6.1 Introduction

Deposition of PZT thin films on Silicon/$SrTiO_3$ (Si/STO) structures has been reported [132]. Epitaxial STO layer deposited on the single crystal Si substrate with (001) orientation is used as a virtual substrate for PZT growth. Integration of ferroelectric materials with high mobility substrates including III-V semiconductors represents a useful research topic. Improving the electrical properties of semiconductor/ dielectric/ ferroelectric structures for device applications is the purpose of this research. The deposition of PZT on a GaAs substrate with a thin layer of STO buffer was found to be problematic due to the diffusion of gallium and arsenic atoms and their reaction with lead atoms at the interface. Arscott et al. [133] reported a sol–gel derived PZT thin films fabricated on a platinized GaAs substrate. A silicon nitride barrier layer was used to isolate the PZT from the GaAs. Rapid Thermal Processing (RTP) technique was employed to minimize the gallium and arsenic diffusion.

In this chapter several mechanisms to prevent the gallium and arsenic diffusion into the STO layer are investigated. The deposition of single crystalline PZT on GaAs/STO substrate employed these mechanisms. Sol-Gel spin coating and thermal annealing, and pulsed laser deposition techniques are used for PZT deposition.

6.2 Spin Coating Deposition of PZT on GaAs

In PZT spin coating process, after spin coating and solvent evaporation step, the film requires a pyrolysis step at 400˚C where the PZT film is still amorphous. Annealing

the sample at 500˚C results in pyrochlore $Pb_2Ti_2O_6$ PZT phase. The transition from pyrochlore to perovskite phase occurs at higher temperatures; at 600˚C PZT exhibits in the perovskite phase [134]. A similar process was employed for deposition of PZT on GaAs/STO structure. The spin coating process as shown in Figure 6.1 was carried out in a 25˚C argon atmosphere.

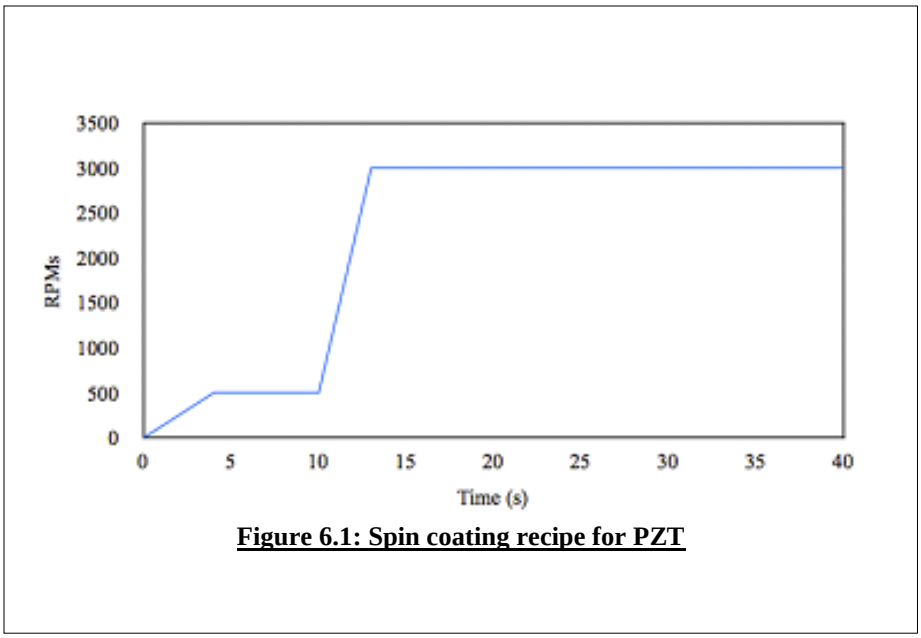

Figure 6.1: Spin coating recipe for PZT

The sample was then annealed in Argon/Oxygen (95/5) atmosphere at 600˚C for 30 minutes after pyrolysis in pure argon gas.

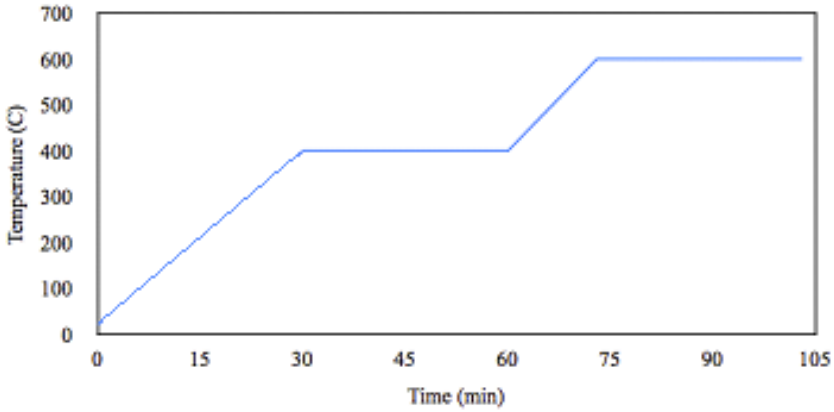

Figure 6.2: Annealing recipe for PZT

Experimental results show that deposition of PZT on GaAs/STO structure is more challenging than deposition on Si/STO substrates. Practically, annealing the sample at any temperature above 400˚C destroys the surface. The sample after annealing has a very rough surface with cracks. The XRD measurement shows some weak PZT phases with preferred (001) and (221) orientation.

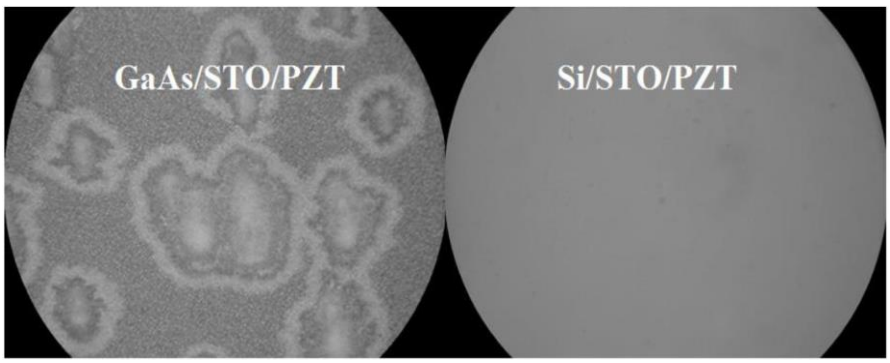

Figure 6.3: Optical microscope image from the surface of Si/10nm-STO/50nm-PZT and GaAs/10nm-STO/50nm-PZT deposited with spin coating and annealing using the same recipe

Rapid thermal annealing can minimize the As and Ga diffusion during the annealing process. So, it enables the growth of PZT on GaAs/STO substrate. The same spin coating recipe as shown in figure 6.1 is employed to deposit PZT film on GaAs/STO substrate. The sample is then annealed in an RTA process. The temperature raised to 600°C with the rate of 30°C/s; then the sample is kept at that temperature for 30 minutes. XRD measurement result as shown in figure 6.4 illustrates the formation of single crystalline PZT with the preferred orientation of (001).

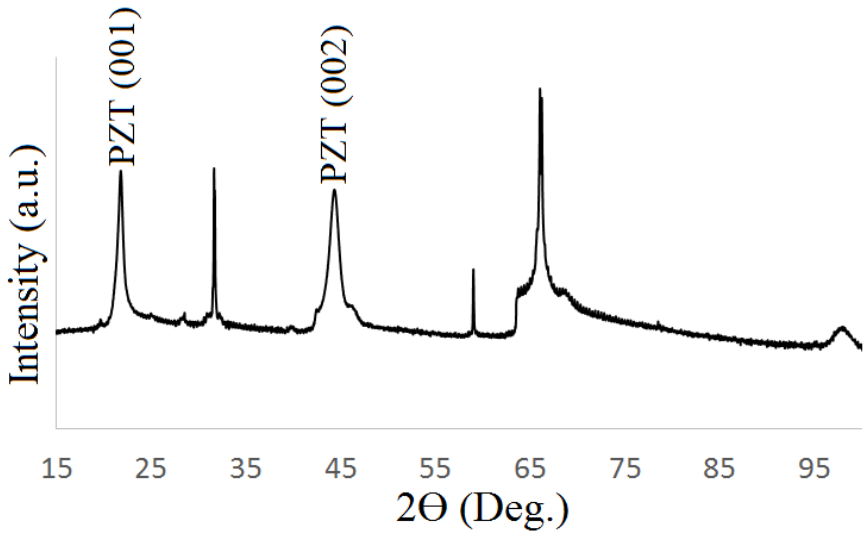

Figure 6.4: XRD measurement on GaAs/5nm-STO/50nm-PZT sample deposited using spin coating and RTA

The ferroelectricity behavior of PZT film deposited on GaAs/STO substrate with spin coating and RTA process is verified using P-E measurement technique.

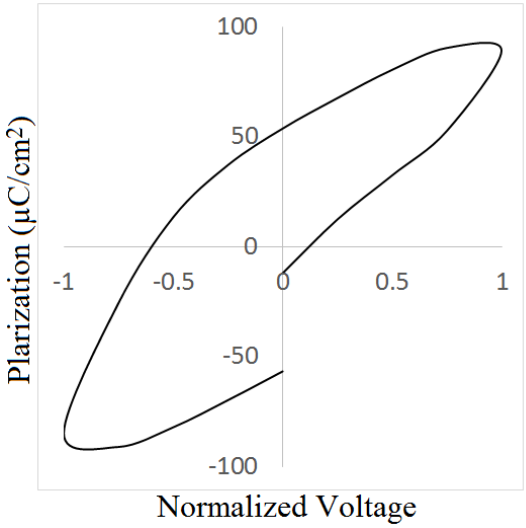

Figure 6.5: P-E measurement on GaAs/5nm-STO/50nm-PZT sample deposited using spin coating and RTA

RTA process affects the surface roughness of the PZT film. As shown in AFM measurement result below, the film deposited by this method has a roughness (Ra) of 22.8nm. This high roughness value limits the application of the device.

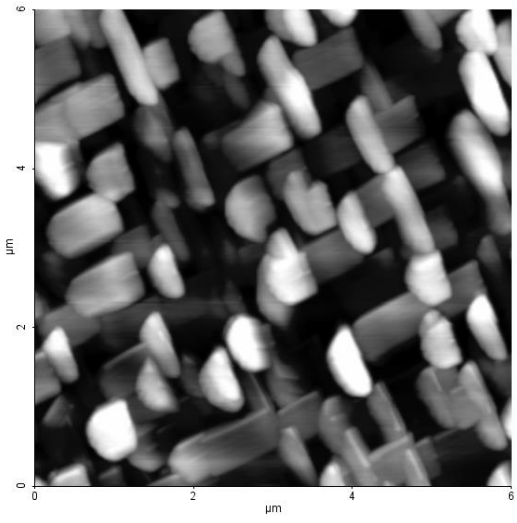

Figure 6.6: AFM measurement on GaAs/5nm-STO/50nm-PZT sample deposited using spin coating and RTA

6.3 Pulsed Laser Deposition of PZT on GaAs

In this section the deposition of PZT on GaAs/STO substrate employing two different techniques: using the buffer layer and direct deposition is explained. The STO film with a thickness below 10nm, deposited by MBE, is called thin STO. The STO films with a thickness above 10nm, which were deposited by PLD on top of thin STO films are named thick STO.

6.3.1. Deposition of PZT on GaAs/STO Using a Thick STO layer

As with spin coating, in pulsed laser deposition, direct deposition of PZT on a GaAs substrate with a thin layer of STO buffer is not possible due to the diffusion of gallium and arsenic atoms and their reaction with lead atoms. The XRD measurement results as shown in figure 6.7 compares the results for deposition of PZT on Si/STO and GaAs/STO substrates. For both growths, all deposition parameters were the same. The sample temperature is 600°C during the deposition using 1.7 J/cm^2 laser at oxygen atmosphere with the pressure of 100mT. The process was then completed with a 10minute post-annealing step at oxygen atmosphere with the pressure of 100mT. The PZT film grown on Si/STO substrate shows single crystal PZT with (001) orientation. However, the PZT film grown on GaAs/STO substrate shows no PZT peak in the 2Ɵ scan.

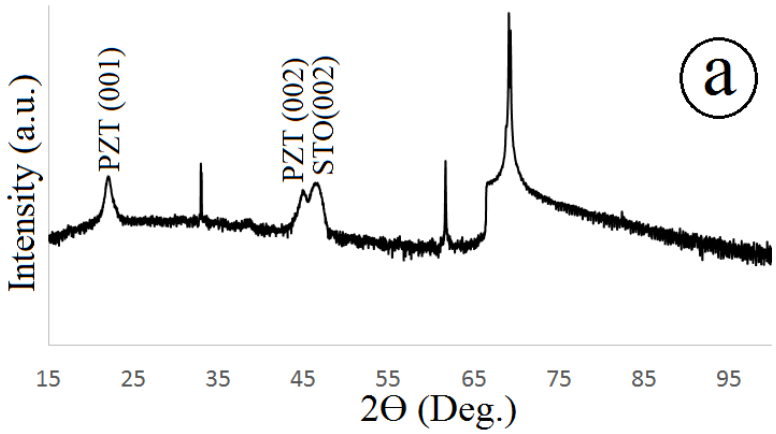

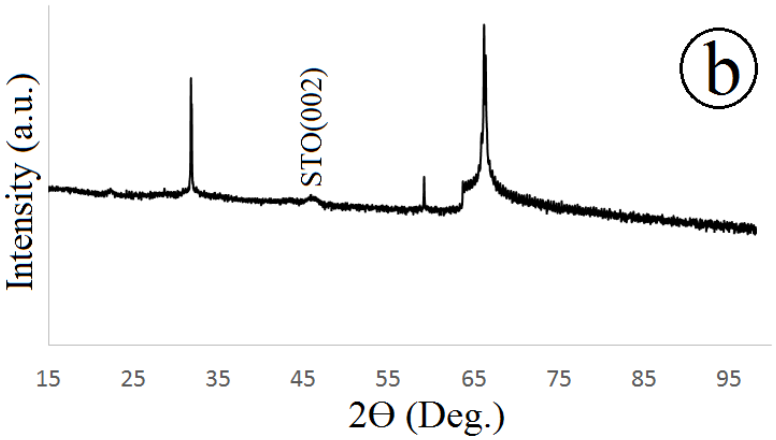

Figure 6.7: XRD measurement on a. Si/10nm-STO/25nm-PZT, b. GaAs/5nm-STO/25nm-PZT

The TEM results as shown in figure 6.8 illustrates the formation of non-crystallized PZT with a thin layer of gallium oxide formed below the STO layer.

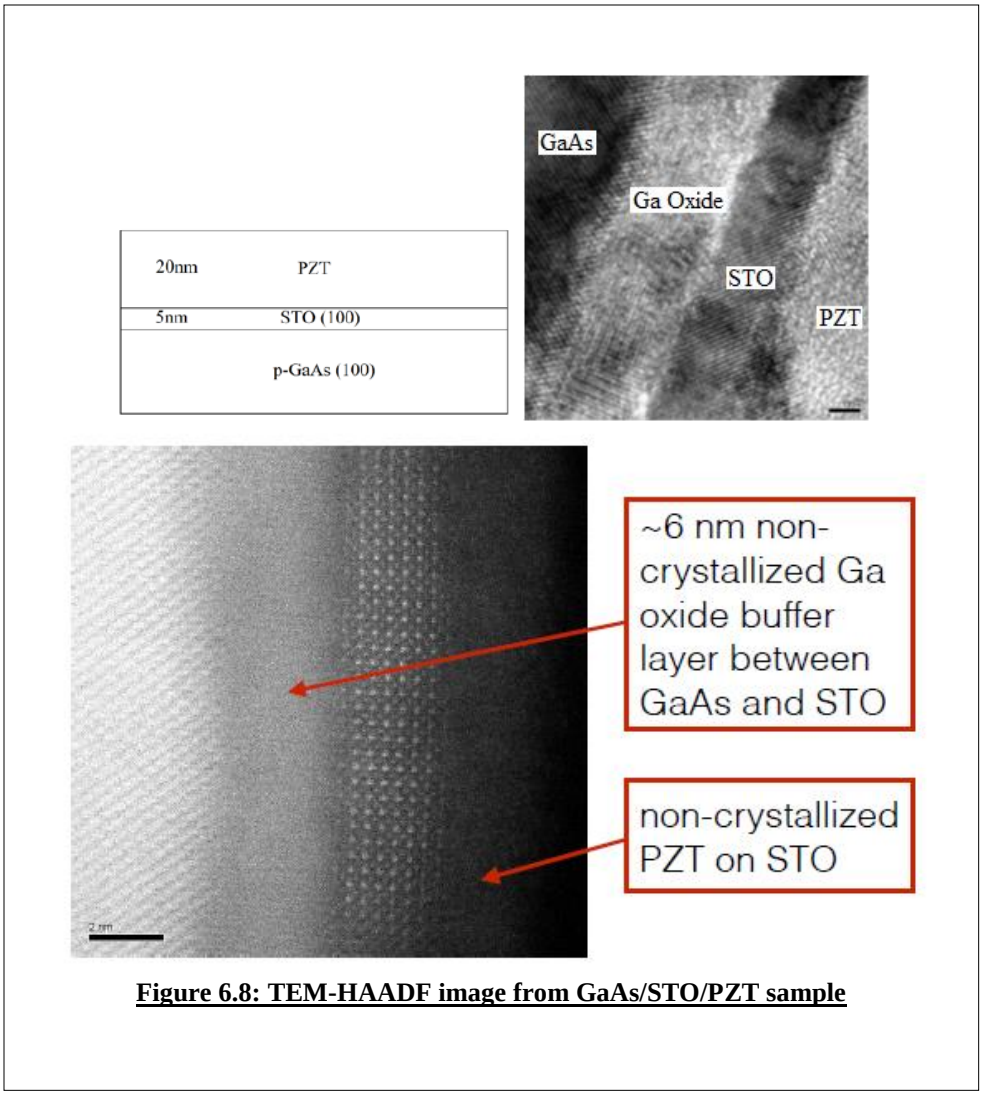

Figure 6.8: TEM-HAADF image from GaAs/STO/PZT sample

The diffusion of gallium and arsenic atoms and their reaction with lead atoms can be eliminated using a thicker layer of STO. To verify this fact, GaAs/STO substrates with different STO thicknesses were used to grow PZT. In this experiment, an extra layer of STO was deposited on top of the GaAs/5nm-STO substrates using PLD just perior to PZT deposition. To find the optimum parameters for STO deposition using PLD technique, several experiments are carried out using GaAs/STO substrates. The pressure of oxygen was the key parameter affecting the deposition of high-quality STO using PLD system. As shown in figure 6.9, the deposition of STO on GaAs/STO substrate in an

ambient with high O_2 pressure (100mT) results in more than one STO phase. The issue was solved using a lower oxygen pressure ($1x10^{-4}$T). For STO growth, the 60nm film was grown using a substrate temperature of 600°C and 2.7 J/cm^2 10Hz laser.

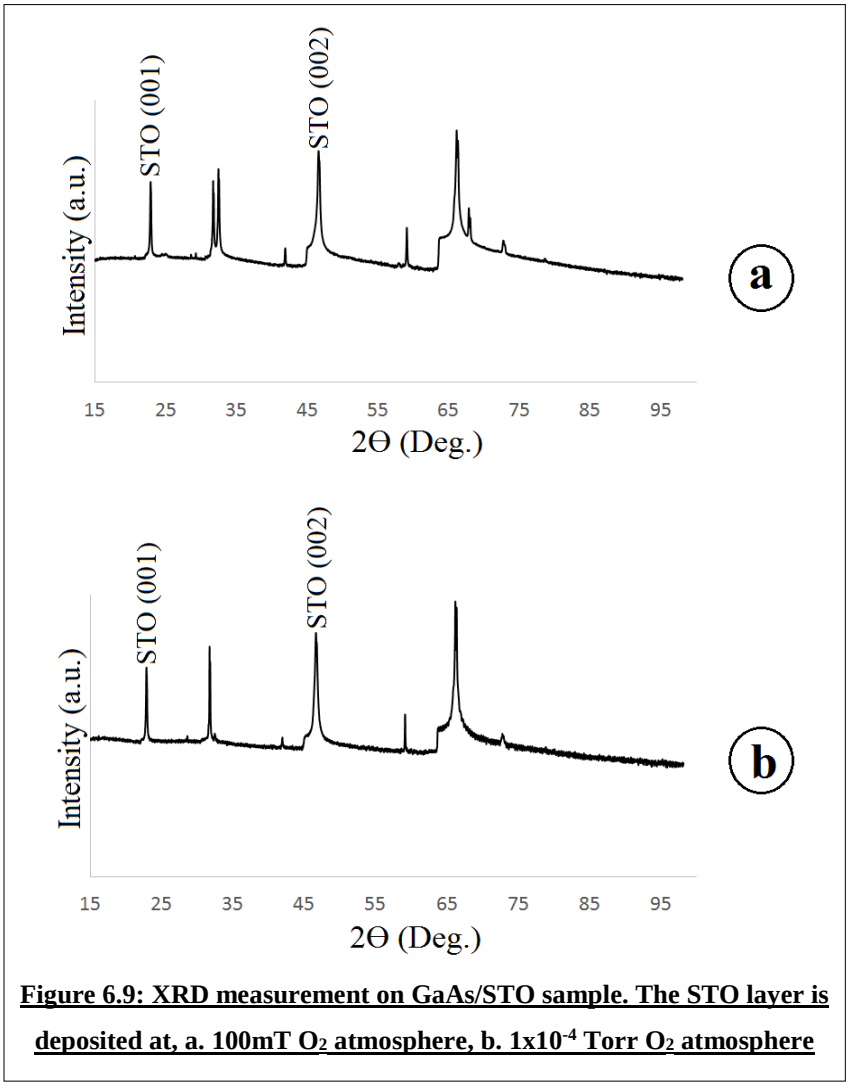

Figure 6.9: XRD measurement on GaAs/STO sample. The STO layer is deposited at, a. 100mT O_2 atmosphere, b. $1x10^{-4}$ Torr O_2 atmosphere

The optimum recipe found for STO growth was a deposition at 600°C in $1x10^{-4}$ Torr O_2 atmosphere using 2.7 J/cm^2 10Hz laser followed by post growth annealing at 600°C in $1x10^{-4}$ Torr O_2 atmosphere for 10 minutes. This recipe was then used to deposit different thickness of STO to be used for PZT deposition. Figure 6.10 illustrates the effect of STO thickness on the deposition of single crystalline PZT.

The experimental study shows that when a thin layer of STO was used, the PZT film has weaker XRD peaks for PZT (001) and (002). Increasing the STO thickness above 23nm, a single crystalline PZT film can be deposited on the substrate as seen the sharp (001) and (002) PZT peaks in figure 6.10. However, a Semiconductor-Dielectric-Ferroelectric structure with a thick dielectric layer is not practically useful for device applications. The ferroelectricity behavior of PZT film deposited on GaAs/Thick-STO/PZT was verified using P-E measurement technique.

The diffusion of gallium and arsenic atoms and their reaction with lead atoms can also be eliminated employing another buffer layer such as $LaAlO_3$ (LAO) or $La_{1-x}Sr_xMnO_3$ (LSMO).

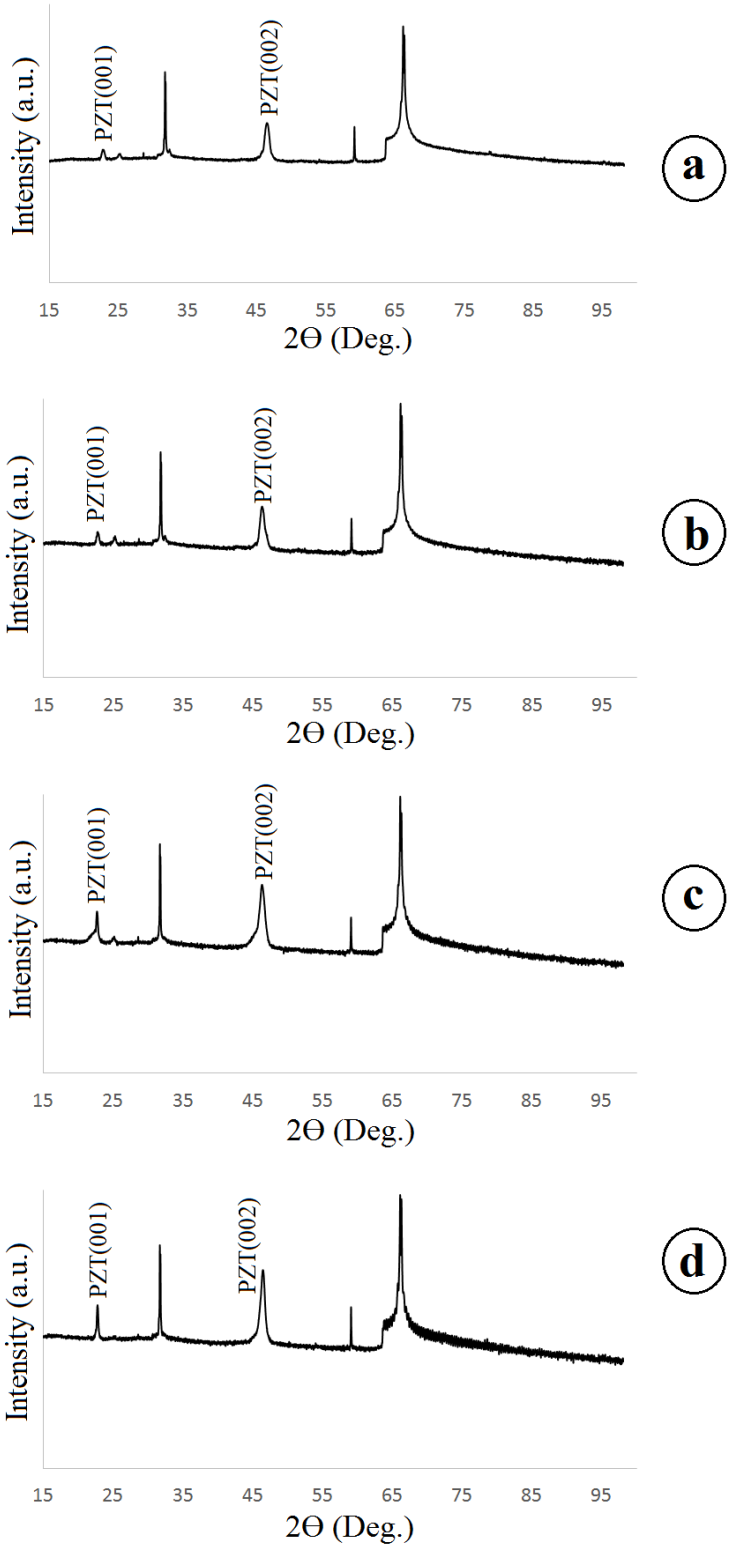

Figure 6.10: XRD measurement on a. GaAs/10nm-STO/25nm-PZT, b. GaAs/13nm-STO/25nm-PZT, c. GaAs/17nm-STO/25nm-PZT, d. GaAs/23nm-STO/25nm-PZT

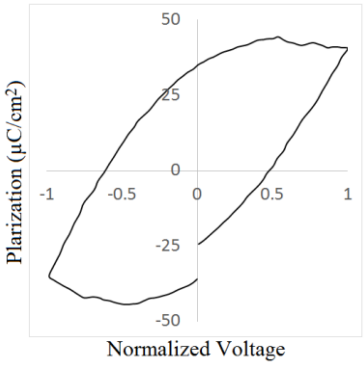

Figure 6.11: P-E measurement on GaAs/23mn-STO/25nm-PZT

6.3.2. Deposition of PZT on GaAs/STO Using an LAO Buffer layer

The growth of LAO on PZT/STO was carried out using different recipes. The direct growth of LAO on PZT/STO at 600°C results in extra phases. The issue can be solved depositing LAO in a lower temperature followed by a post growth annealing in higher temperature. The best recipe found for LAO growth was a deposition at 400°C in 100 mTorr O_2 atmosphere using 2.7 J/cm^2 10Hz laser followed by post growth annealing at 600°C in 100 mTorr O_2 atmosphere for 20 minutes. The XRD measurement shown in figure 6.12 illustrates the difference between the LAO growth at high temperature and lower temperature with post-annealing at high temperature. The LAO film deposited at lower temperature followed by a post growth annealing at higher temperature exhibits (001) and (002) peaks while the LAO film deposited at high temperature exhibits other phases.

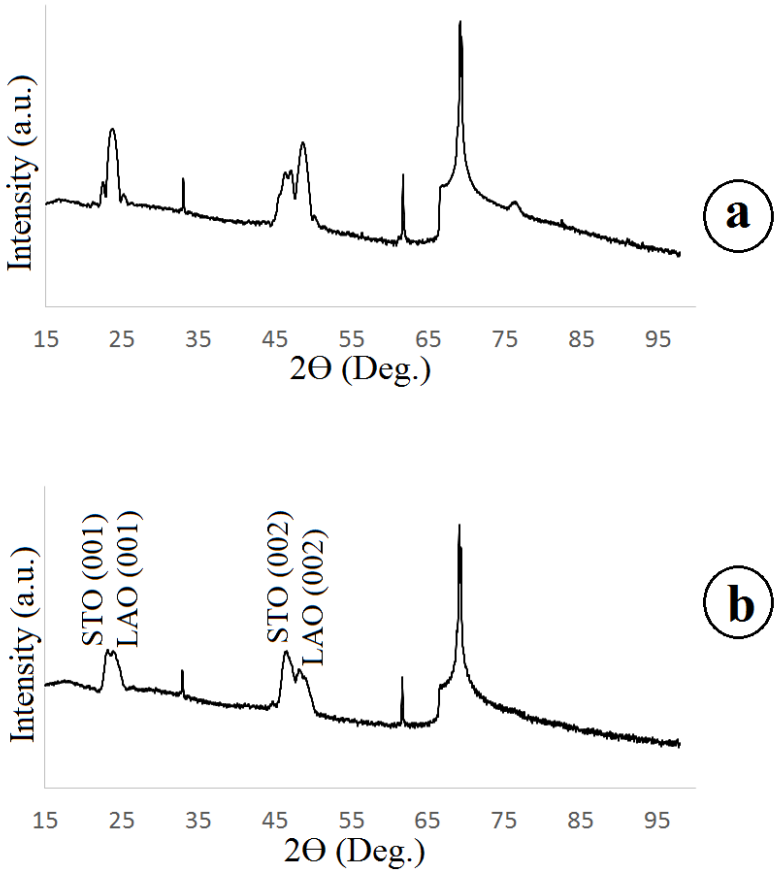

Figure 6. 12: XRD measurement on a. Si/10nm-STO/LAO deposited at high temperature, b. Si/10nm-STO/LAO deposited at 400°C and post-annealed at high temperature

The XRD measurement on GaAs/STO/LAO/PZT sample is illustrated in figure 6.13. The experimental study shows that an LAO layer with over 6nm thickness can prevent the Ga and As diffusion. The XRD measurement shows single crystalline PZT growth for 6nm and 30nm LAO layer. However, decreasing the LAO layer to 4.2nm results in PZT peaks with less intensity. There is no PZT peak observed when 3nm LAO was used.

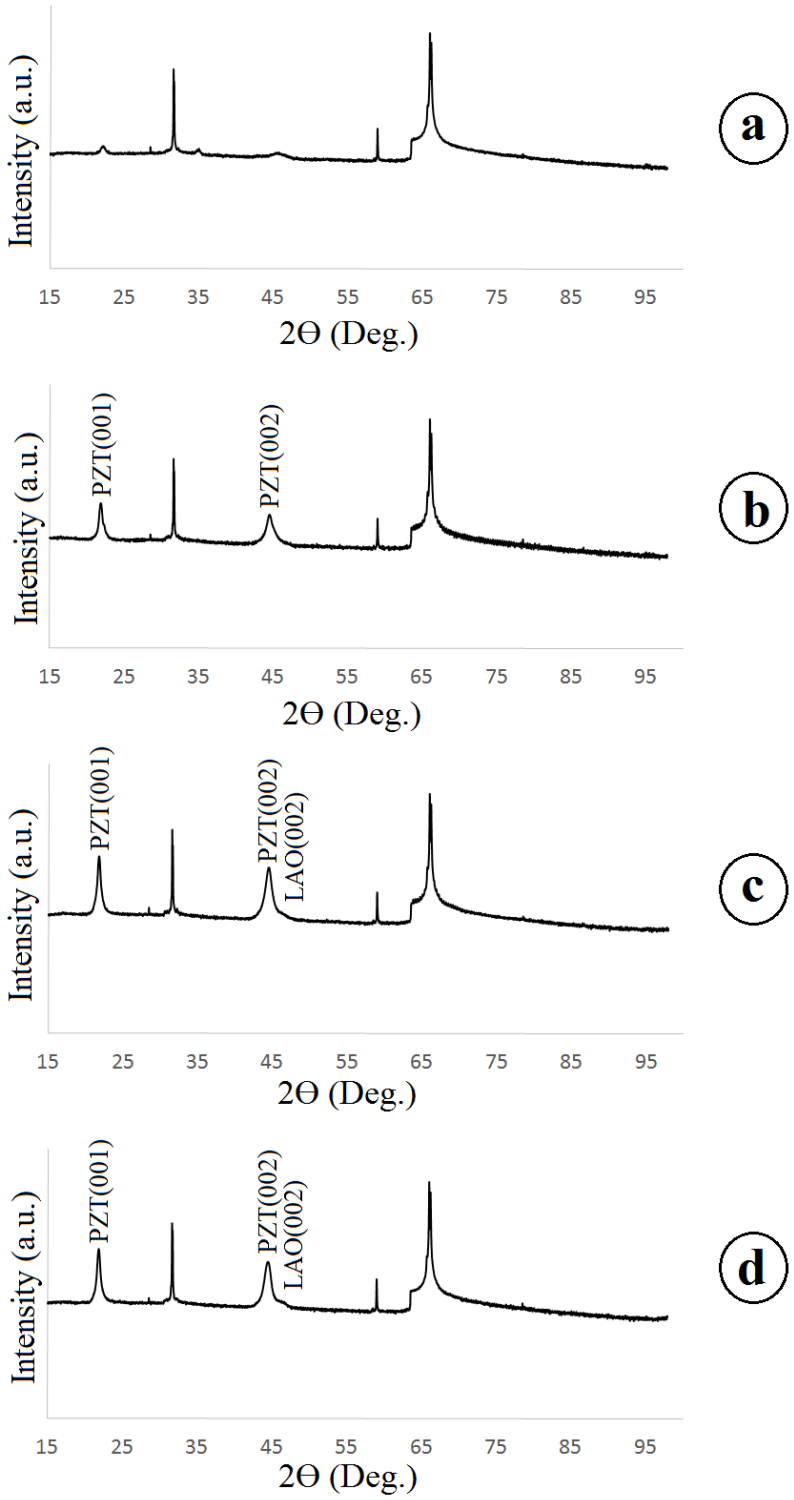

Figure 6. 13: XRD measurement on a. GaAs/5nm-STO/3nm-LAO/25nm-PZT, b. GaAs/5nm-STO/4.2nm-LAO/25nm-PZT, c. GaAs/5nm-STO/6nm-LAO/25nm-PZT, d. GaAs/5nm-STO/30nm-LAO/25nm-PZT

The TEM measurement result as shown in figure 6.14 illustrates a sharp STO/LAO interface. The structure also has a thin layer of gallium oxide at the GaAs/STO interface.

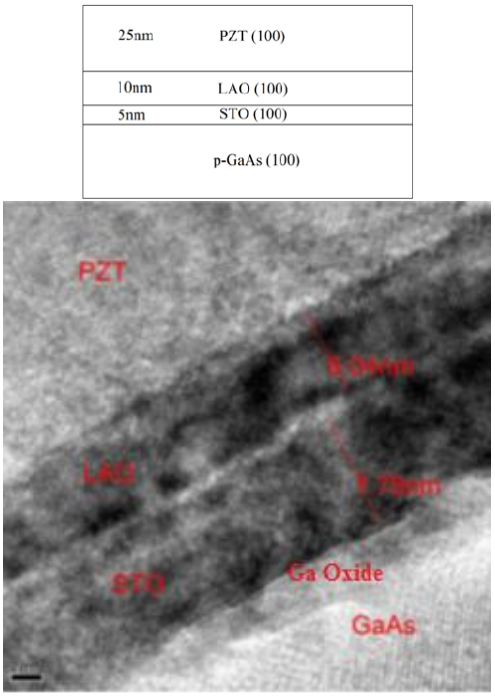

Figure 6. 14: TEM-HAADF image

The ferroelectricity behavior of PZT film deposited on GaAs/STO/LAO substrate was verified using P-E measurement technique.

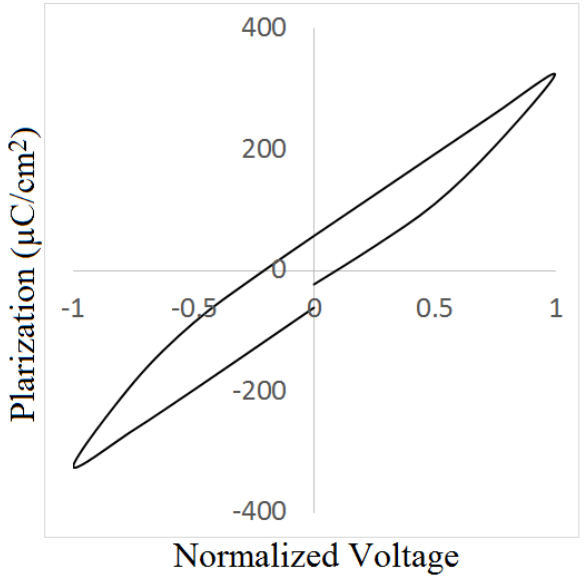

Figure 6.15: P-E measurement on GaAs/5nm-STO/30nm-LAO/25nm-PZT sample

6.3.2. Deposition of PZT on GaAs/STO Using a LSMO Buffer layer

The growth of LSMO on PZT/STO was developed using various recipes. The optimized recipe found for LSMO growth was deposition on 600°C in 100 mTorr O_2 atmosphere using 1.3 J/cm^2 10Hz laser followed by post growth annealing at 600°C in 100 mTorr O_2 atmosphere for 20 minutes.

The XRD measurement on GaAs/STO/LSMO/PZT sample is illustrated in figure 6.16. The experimental study shows that an LSMO layer with over 48nm thickness can prevent the Ga and As diffusion. The XRD measurement shows single crystalline PZT growth for 48nm and 60nm LSMO layer. However, decreasing the LSMO layer to 43nm results in no PZT peaks.

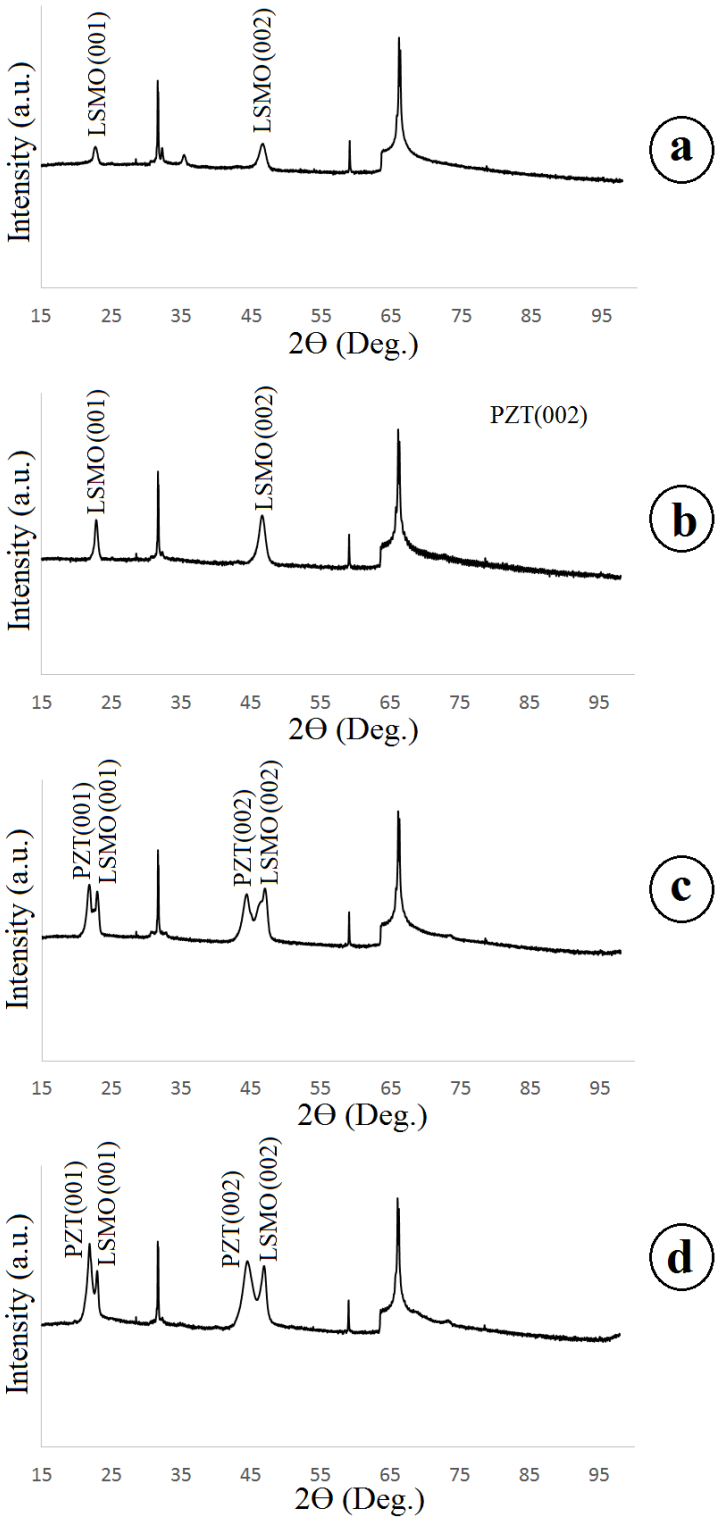

Figure 6. 16: XRD measurement on a. GaAs/5nm-STO/12nm-LSMO/25nm-PZT, b. GaAs/5nm-STO/ 43nm-LSMO/25nm-PZT, c. GaAs/5nm-STO/48nm-LSMO /25nm-PZT, d. GaAs/5nm-STO/60nm-LSMO /25nm-PZT

The TEM measurement result as shown in figure 6.17 illustrates a sharp STO/LSMO interface. The structure also has a thin layer of Gallium oxide under STO layer.

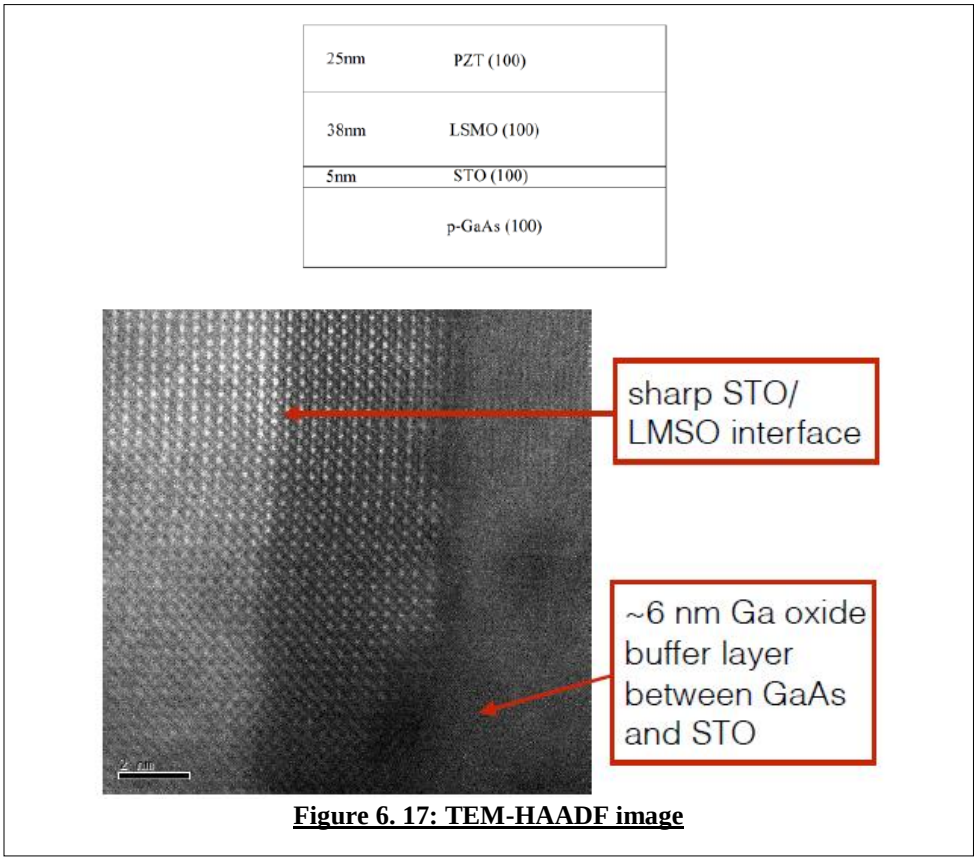

Figure 6. 17: TEM-HAADF image

The ferroelectricity behavior of PZT film deposited on GaAs/STO/LSMO substrate is verified using P-E measurement technique.

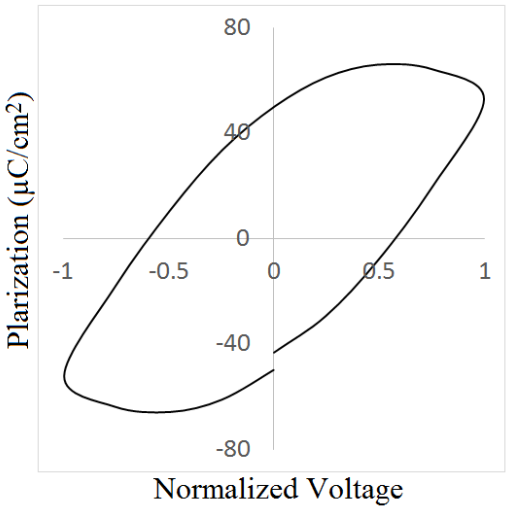

Figure 6. 18: P-E measurement on GaAs/5nm-STO/60nm(3000P)-LSMO /25nm-PZT sample

6.3.4. Direct Deposition of PZT on GaAs/STO

To investigate the deposition of PZT directly on GaAs/5nm-STO structure the deposition was carried out in an argon atmosphere using a pressure of 100 mT. The temperature of the sample was 600°C during the 40m deposition. The sample was then post-annealed in the vacuum for 20m. It was expected that the absence of O_2 will not solve the issue of Ga and As diffusion. However, this experiment was set up to compare the results with the ambient atmosphere to provide more data for understanding the chemical reactions. Surprisingly the result was promising. The XRD measurement result as shown in figure 6.19 illustrated a single crystalline PZT with (001) and (002) peaks.

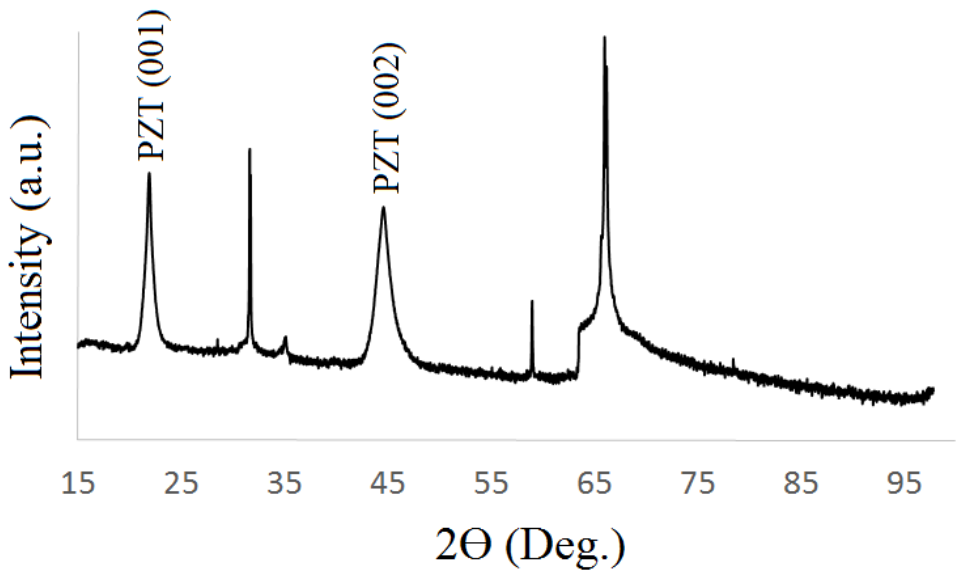

Figure 6. 19: XRD measurement on GaAs/STO/PZT sample grown on Argon atmosphere

As shown in figure 6.20, the result of this experiment was not reproducible. The XRD measurement result exhibits no strong PZT peak.

After all growth parameters were carefully verified, and the experiment was repeated several times, no PZT peak was observed. To investigate the measurement tolerance, the experiment was repeated with minor change in the growth parameters including temperature, pressure, and laser energy. The result was no PZT phase being present. Further investigation noted that before the first experiment, the PZT target has not been used for several weeks. The possibility of a chemical reaction on PZT target during that period was concluded from this fact. The research was then focused on the behavior of the PZT target under UV laser exposure, resulting an extensive study on PZT deposition using PLD technique as explained in the previous chapter.

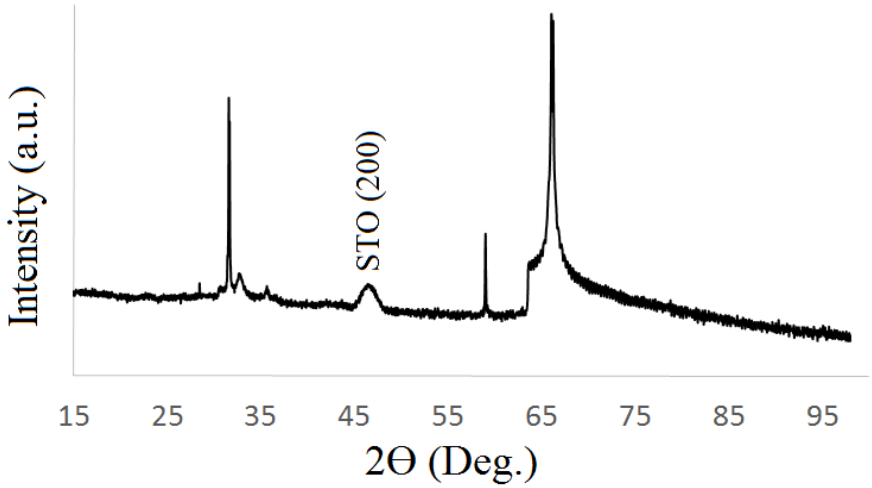

Figure 6. 20: XRD measurement on GaAs/STO/PZT sample grown on Argon atmosphere

A strong lead phase on the surface of the target was found to be the main reason preventing the growth of PZT on GaAs/STO structure. As explained in the previous chapter, after exposure to the laser, a thin layer of Pb is formed on the target surface. Because of the high absorption of lead for UV light, when this target is employed for PZT deposition on the GaAs substrate, the material transferred to the substrate in first few seconds of the deposition, is lead. Lead atoms can chemically react with Gallium and Arsenic atoms that are diffused to the surface of the sample or vice versa.

The use of a mechanically cleaned target enables the growth of the PZT on GaAs/STO sample. Figure 6.21 illustrates the XRD measurement result of deposition of PZT films on GaAs/STO substrate in the oxygen atmosphere with the pressure of 100mT using 10Hz laser with the fluence of 1.7 J/cm^2. The PZT target used for this experiment is mechanically polished and has a clean surface.

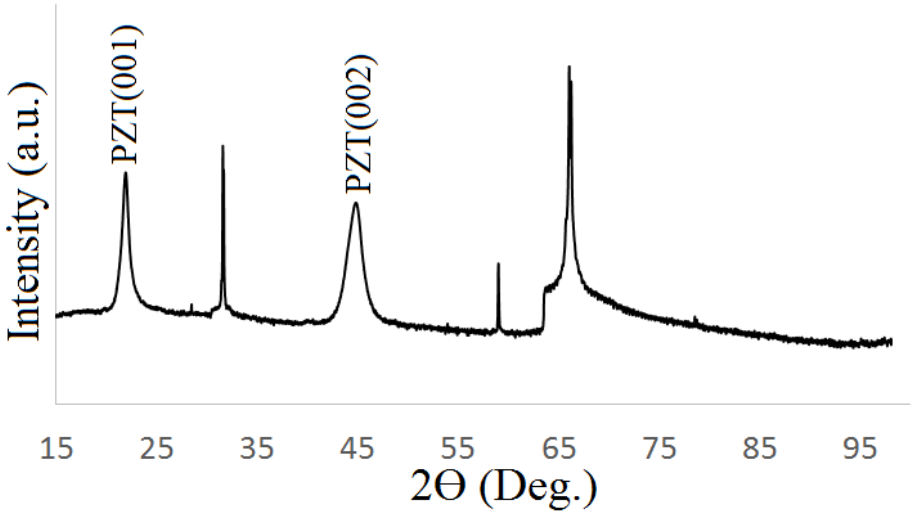

Figure 6. 21: XRD measurement on GaAs/STO/PZT sample. PZT film is deposited using 1 J/cm^2 Laser, in O_2 atmosphere with pressure of 100mT using a mechanically cleaned target

The ferroelectricity behavior of PZT film deposited on GaAs/STO substrate using a mechanically cleaned target is verified using P-E measurement technique.

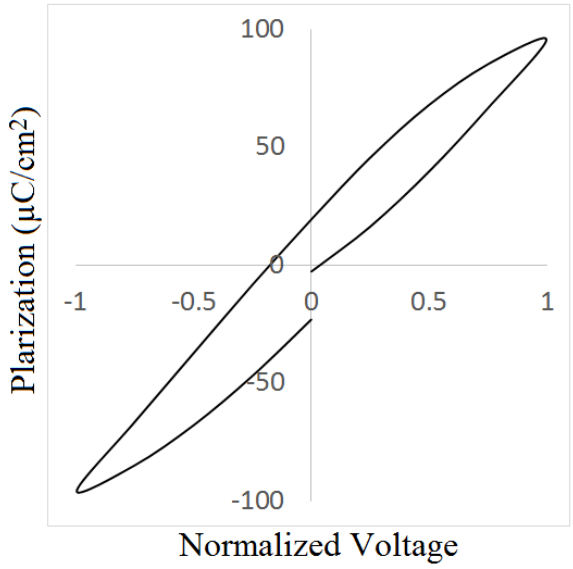

Figure 6. 22: P-E measurement on GaAs/STO/PZT sample. PZT film is deposited using 1 J/cm^2 Laser, in O_2 atmosphere with pressure of 100mT using a mechanically cleaned target

A mechanically cleaned target can be used once for PZT film deposition. After several minutes of laser exposure on the target, the formation of the lead on the target surface prevents subsequent growths using the same target. The process to remove the target from the vacuum chamber, mechanical cleaning, and returning the target is highly time-consuming. The idea of integrating a system to clean the target mechanically after each deposition is not also easy to implement because of the risk of contamination spread all over the chamber. So, other alternative solutions are investigated.

Annealing the target is another alternative method to prevent the formation of lead on the surface of the target. Annealing the target in air minimizes the Pb phases and converts it to PbO. For this the target was placed in a furnace. The XRD measurements for the PZT target after annealing in 400°C for 30 minutes is illustrated in figure 6.23.

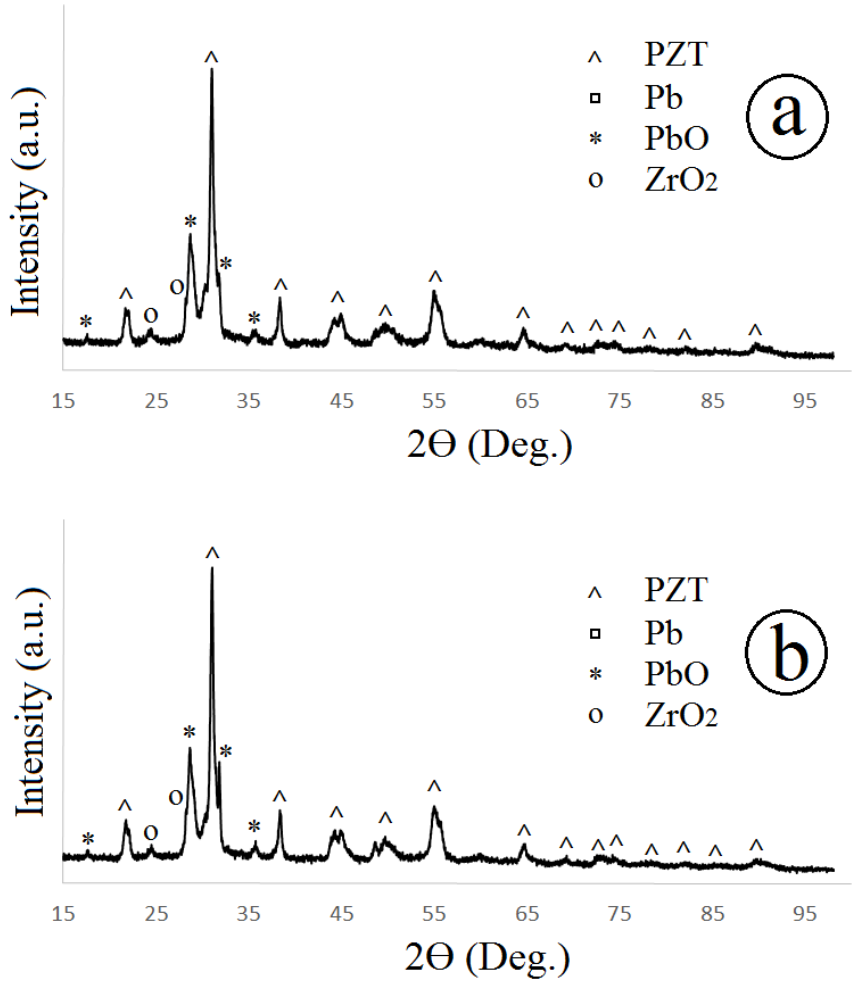

Figure 6. 23: a. XRD measurement on PZT target after 10m laser exposure in 100mTorr O_2 and annealing in 400°C for 30 minutes b. XRD measurement on PZT target after 10m laser exposure in 100mTorr Ar and annealing in 400°C for 30 minutes

The use of the annealed target to deposit PZT in PLD chamber results in single crystalline PZT film with (001) orientation as shown in figure 6.24.

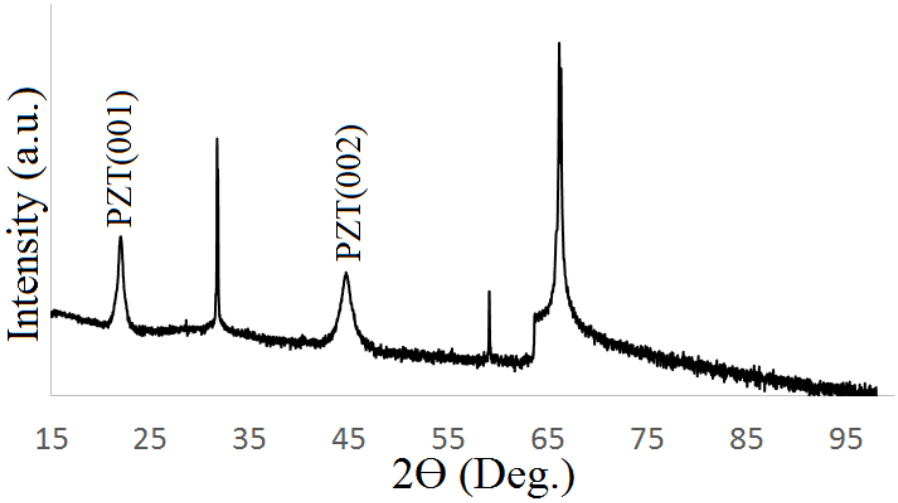

Figure 6. 24: XRD measurement on GaAs/STO/PZT sample. PZT film is deposited using 1 J/cm^2 Laser, in O_2 atmosphere with pressure of 100mT using an annealed target

The ferroelectricity behavior of PZT film deposited on GaAs/STO substrate using an annealed target was verified using P-E measurement technique.

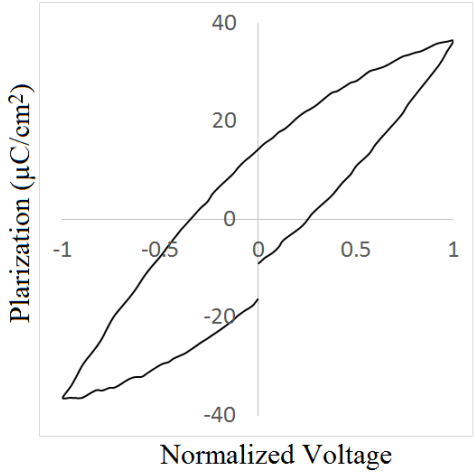

Figure 6. 25: P-E measurement on GaAs/STO/PZT sample. PZT film is deposited using 1 J/cm^2 Laser, in O_2 atmosphere with pressure of 100mT using an annealed target

The idea of using a built-in heater for the PZT target can enable the growth of PZT film on multi-substrates without the requirement to removing the target from the vacuum chamber. The dimension and structure of our PLD chamber are not conducive for a target heater installation. So, the surface heating using a high power UV laser was investigated. As shown in figure 6.26, a 6W 450nm laser diode was installed on one of the chamber windows. The continuous laser beam was focused on the target surface, providing the fluence of 75 W/cm^2. This energy is sufficient to remove most of the Pb from the target surface. To sweep the focused laser beam on the surface of the target, a servo motor was employed to guide the beam over the target. Rotating the target during this process, the laser beam covers the whole area of the target.

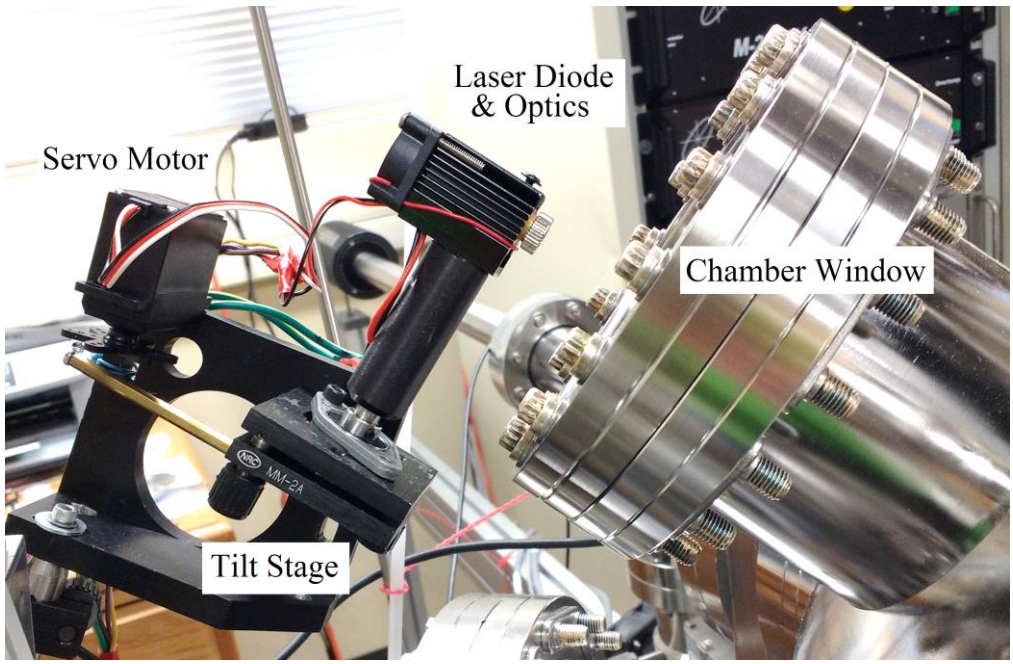

Figure 6. 26: 6W 450nm laser diode installed on PLD chamber window

In order to improve the printing quality, the contrast and brightness of this image is modified

The XRD measurement result on the target after exposure to the 10Hz 1.7 J/cm^2 laser for 30 minutes in an oxygen atmosphere with the pressure of 300mT, followed by exposure to 450nm laser, shows no strong Pb phase.

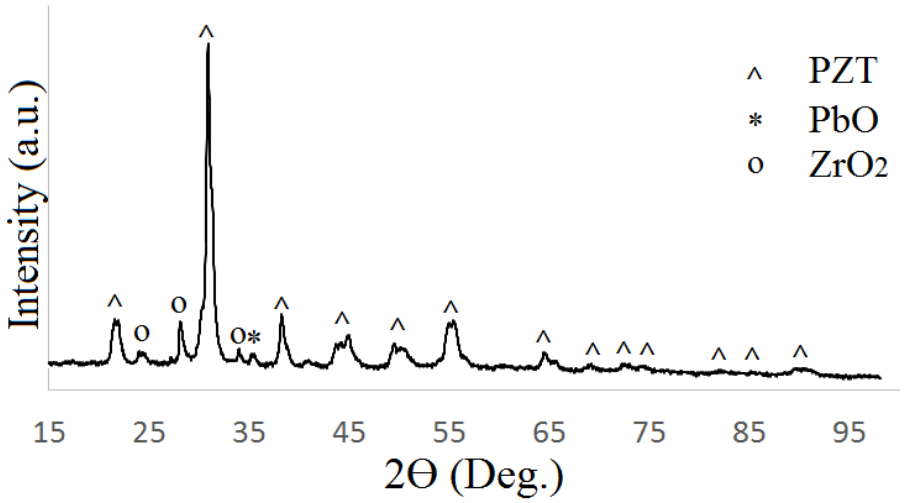

Figure 6. 27: XRD measurement on PZT target exposed to 450nm laser

The use of this target for PZT deposition, as shown in XRD measurement below, results in single crystalline PZT film with (001) orientation.

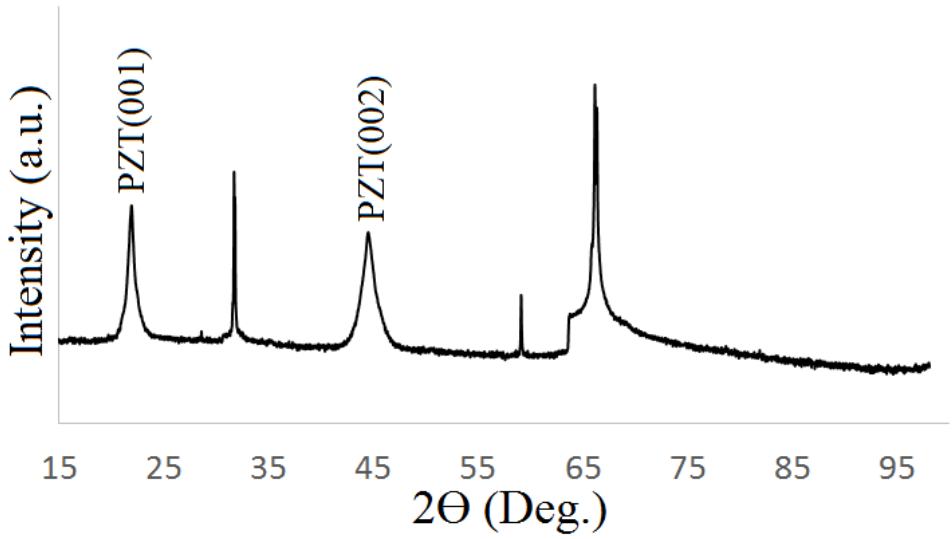

Figure 6. 28: XRD measurement on GaAs/STO/PZT sample. PZT film is deposited using 2.7 J/cm^2 Laser, in O_2 atmosphere with pressure of 100mT using a laser cleaned target

The ferroelectricity behavior of PZT film deposited on GaAs/STO substrate using a laser cleaned target is verified using P-E measurement technique (Figure 6.29.a). Atomic Force Microscope (AFM) equipped with Piezoelectric Force Microscope (PFM) is also employed to measure the piezoelectric responses of the film. AFM topography measurement, as illustrates in figure 6.29.b, shows the roughness (R_a) value of 2.33nm. PFM out-of-plane (OP) amplitude (Figure 6.29.c) and OP-phases (Figure 6.29.d) were measured for +10V polarized, -10V polarized, and non-polarized regions. The polarization voltage was chosen 10V for saturation of polarization.

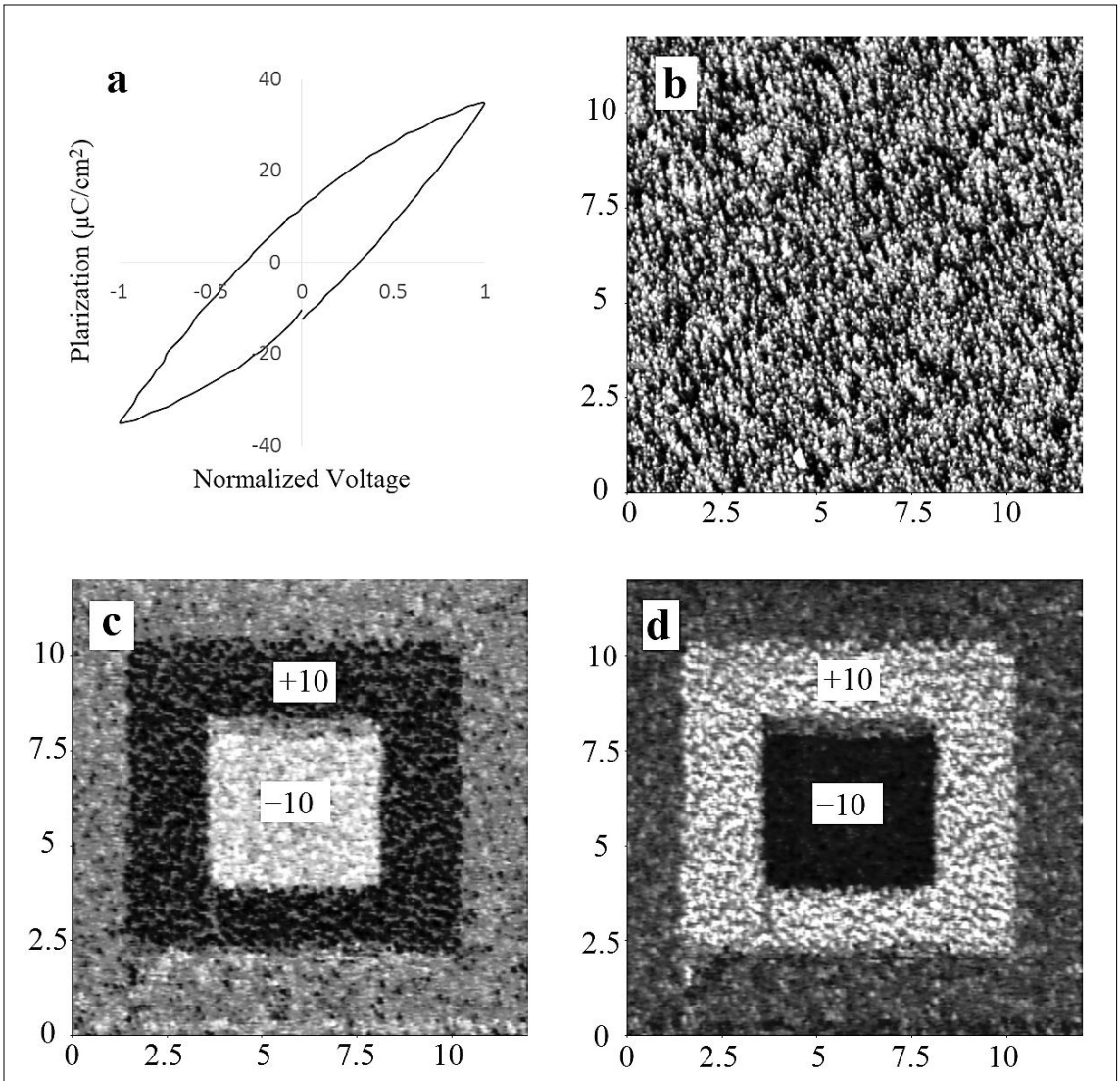

Figure 6. 29: A. P-E measurement on GaAs/STO/PZT sample. PZT film is deposited using 2.7 J/cm^2 Laser, in O_2 atmosphere with pressure of 100mT using a laser cleaned target, b. AFM topography measurement, dimensions are µm, c. PFM OP-phase, dimensions are µm, d. PFM OP-amplitude, dimensions are µm

In order to improve the printing quality, the contrast and brightness of this image is modified

EDAX measurement as shown in figure 6.30 illustrates the effect of mechanical polishing and 405nm laser exposure on the compound of deposited PZT films.

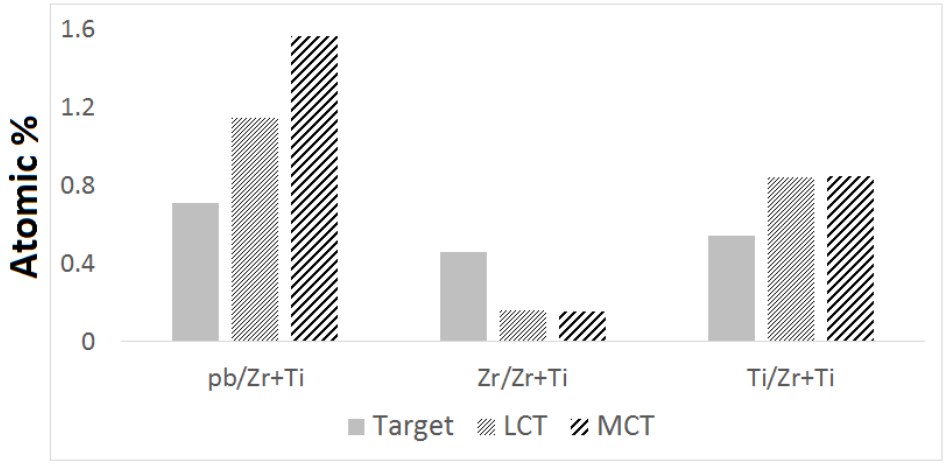

Figure 6. 30: EDAX measurement comparing the compound of PZT target (Target) with the PZT film deposited using mechanically cleaned target (MCT) and laser cleaned target (LCT)

The EDAX measurement shows Zr deficiency on the deposited film using laser cleaned target and mechanically cleaned target. To keep the compound of PZT film similar to the target, the deposition process can be started using a mechanical cleaning process or a 405nm laser exposure. Then, the normal deposition in continued using the optimum condition as explained in the previous chapter.

CHAPTER VII. CONCLUSION AND RECOMMENDATION FOR FURTHER RESEARCH

This chapter presents an overall conclusion on the performed research and results, followed by suggestions for future work on this research topic.

7.1. Results and Conclusion

Semiconductor structures, because of their high electron mobility properties, provide a platform for novel electronic devices. Oxide materials possess unique functionalities which when combined with semiconductors will enable a variety of novel device applications. They have properties that include high dielectric constant, ferromagnetism, and ferroelectricity. This research was mainly focused on two ferroelectric materials: LNO and PZT.

The frequency dependence is an important drawback for the functionality of ferroelectric-based varicaps. The presented research investigated the effect of frequency on the capacitance and loss factor of LNO-based varicaps. A process to improve the frequency dependence of the LNO capacitor employing a thin layer of CCTO dielectric has been explained. Si/LNO/CCTO heterostructure fabricated using a cost-effective spin coating and thermal annealing process, shows over 15 times better frequency stability in comparison with Si/LNO structure in the range of 3.25-3.5MHz. The research also explains how the crystal properties of the CCTO thin film can be improved annealing the sample at higher temperatures. So, the structure has been changed to Si/CCTO/LNO to allow for annealing the Si/CCTO structure at 900°C before the deposition of LNO. The

research shows the effect of CCTO/LNO thickness ratio on the frequency stability of Si/CCTO/LNO heterostructure.

The presented study shows that the application of CCTO/LNO heterostructure is not limited to the varicap and stable capacitor application. This novel structure can also be used in UV tuned capacitors and capacitive UV detectors. The frequency and temperature dependence of conventional CCTO-based UV tuned capacitors were investigated in this research. The study shows how the temperature and frequency dependence of epitaxial CCTO-based UV tuned capacitors were minimized using epitaxial CCTO/LNO heterostructure. The fabricated CCTO/LNO heterostructure showed about two times more sensitivity to the laser exposure at the frequency stabled region comparing with the CCTO-based capacitor. On the other hand, the CCTO/LNO structure was almost six times less sensitive to the temperature variations at the frequency stabled region compared to the CCTO-based capacitor.

Challenging subjects behind the deposition of PZT ferroelectrics using PLD technique was addressed in this dissertation. The results show when depositing materials including volatile elements such as lead, the stoichiometry of the deposited film in PLD procedure can be affected by deposition parameters. The research reported the optimum condition for stabilizing the Pb content of the deposited PZT while the Zr/Ti ratio varies by the oxygen pressure. A significant variation in the Zr/Zr+Ti ratio was employed to deposit PZT films with different crystal structures and electrical properties. The relative dielectric constant of the deposited film, when using the PZT target with the chemical compound of $Pb1.1Zr_{0.53}Ti_{0.47}O_3$, was controlled in the range of 29-130 when changing

the oxygen pressure from 200mT-125mT. The remnant polarization was tuned in the range of 6.6 μC/cm^2 to 42.2 μC/cm^2 varying the oxygen pressure from 125mT to 200mT.

The deposition of PZT ferroelectrics on GaAs substrate was addressed in this research. The issue of gallium and arsenic diffusion and their reaction with lead atoms were mitigated using a buffer layer as well as employing a rapid thermal annealing process. The extensive study on the deposition of PZT ferroelectrics using PLD technique resulted in a better understanding of the behavior of PZT target under the exposure of high power UV laser. It has been observed that the free lead atoms, formed on the surface of the PZT target after laser exposure, was the main reason preventing the direct growth of PZT on GaAs/STO substrate. The study showed that employing a novel modified pulsed laser deposition technique, allows for direct deposition of PZT films on GaAs/STO substrate.

7.2. Recommendation for Future Research

7.2.1. High Frequency Behavior of CCTO/LNO Structure

The CCTO/LNO heterostructure fabricated by employing spin coating, and the thermal annealing process was used as a frequency stabilized varicap. The experimental study showed amazing very good frequency stability for Si/LNO/CCTO and Si/CCTO/LNO structures around the frequency of several MHz. However, the application of this structure in higher radio frequencies is not verified yet. The design and fabrication of CCTO/LNO capacitors, stabilized in much higher frequencies, can be an interesting research topic to employ this structure in RF-electronics.

7.2.2. Negative capacitance in CCTO/LNO hetro-structures

The CCTO/LNO heterostructures fabricated by employing PLD process showed a high-quality epitaxial CCTO/LNO interface. A high-quality ferroelectric/dielectric structure is also important for its negative capacitance behavior. Ferroelectric materials have negative capacitance value in a specific range of charge, around where charge equals zero. This unstable state can be biased using a dielectric capacitor [135]. Consider a positive capacitor (C_p) and a negative capacitor (C_n) in series connection. Using the series capacitors equation, the series combination of these two capacitors has a capacitance larger than either C_p or C_n. We know that: $C = dq/dv$, so, in comparison with individual capacitors, less voltage is required to produce the same amount of charge on the series combination. Integrating this interesting fact with the current Field Effect Transistors (FET) technology can improve the sub-threshold slope of the transistor. Using a lower voltage to provide the same charge to switch the FET channel results in new FETs for low-voltage low-power applications.

Considering the Curie temperature of both CCTO and LNO, the negative capacitance behavior of CCTI/LNO is supposed to happen in an elevated temperature much higher than the room temperature. Such a structure is probably not proper for transistor applications. However, considering the stability of CCTO and LNO at high temperatures, this structure can be used as a high-temperature ultrasonic transducer. It is predicted that the degradation of transducer performance, due to the effect of the high temperature on piezoelectricity effect of the LNO, can be compensated by the negative capacitance effect. Selecting a proper functionality temperature, the voltage in the

CCTO/LNO interface can be boosted, resulting in a stronger signal delivered to the piezoelectric material.

7.2.3. Modified PLD System for Deposition of Other Oxides

The effect of free lead atoms, formed on the surface of the PZT target after laser exposure, was the main reason preventing the direct growth of PZT on GaAs/STO substrate. The issue was solved by converting the lead to PbO in two ways: annealing the target at 400°C or employing a second laser source for heating the target surface. Investigating the use of this mechanism for deposition of other oxide materials can be an interesting research topic.

APPENDIX SECTION

APPENDIX A: ACRONYMS AND PHYSICAL QUANTITIES

PLD	Pulsed Laser Deposition
XRD	X-Ray Diffraction
SEM	Scanning Electron Microscopy
EDX	Energy-Dispersive X-ray Spectroscopy
TEM	Transmission Electron Microscopy
AFM	Atomic-Force Microscopy
STO	$SrTiO_3$
LAO	$LaAlO_3$
CCTO	$CaCu_3Ti_4O_{12}$
LNO	$LiNbO_3$
LSMO	Lanthanum Strontium Manganite
ITO	Indium Tin Oxide
SRO	Sr_2RuO_4
λ	Wavelength
EDS	Energy-Dispersive X-ray Spectroscopy
PFM	Piezo-response Force Microscopy
P_r	Remnant Polarization

REFERENCES

[1] https://en.wikipedia.org/wiki/Semiconductor_industry.

[2] J. Valasek, Phys. Rev. 29, 478 (1921).

[3] Hidemi Takasu, Ferroelectric memories and their applications, Microelectronic Engineering, Volume 59, Issues 1–4, November 2001, Pages 237-246, ISSN 0167-9317.

[4] Woo Young Kim, Hee Chul Lee, Low-voltage nonvolatile multi-bit memory fabricated by the patterning and transferring of ferroelectric polymer film, Organic Electronics, Volume 19, April 2015, Pages 1-6, ISSN 1566-1199.

[5] Pi-Chun Juan, Jyh-Liang Wang, Tsang-Yen Hsieh, Cheng-Li Lin, Chia-Ming Yang, Der-Chi Shye, The physical and electrical characterizations of Cr-doped $BiFeO_3$ ferroelectric thin films for nonvolatile memory applications, Microelectronic Engineering, Volume 138, 20 April 2015, Pages 86-90, ISSN 0167-9317.

[6] S.Y. Wang, F. Guo, X. Wang, W.F. Liu, J. Gao, Tuning the resistive switching memory in a metal–ferroelectric–semiconductor capacitor by field effect structure, Applied Surface Science, Volume 356, 30 November 2015, Pages 898-904, ISSN 0169-4332.

[7] Azzedin D. Es-Sakhi, Masud H. Chowdhury, Silicon-on-Ferroelectric Insulator field effect transistor (SOFFET): Partially depleted structure for sub-60 mV/decade applications, Materials Science in Semiconductor Processing, Volume 39, November 2015, Pages 596-605, ISSN 1369-8001.

[8] Dominik Martin, Ekaterina Yurchuk, Stefan Müller, Johannes Müller, Jan Paul, Jonas Sundquist, Stefan Slesazeck, Till Schlösser, Ralf van Bentum, Martin Trentzsch, Uwe Schröder, Thomas Mikolajick, Downscaling ferroelectric field effect transistors by using ferroelectric Si-doped HfO_2, Solid-State Electronics, Volume 88, October 2013, Pages 65-68, ISSN 0038-1101.

[9] Y.-L. Sun, D. Xie, J.-L. Xu, X.-M. Li, C. Zhang, R.-X. Dai, X. Li, X.-J. Meng, and H.-W. Zhu, “Tunable transport characteristics of double-gated graphene field-effect transistors using P(VDF-TrFE) ferroelectric gating,” Carbon, vol. 96, pp. 695–700, 2016.

[10] Z.H. Liu, C.T. Pan, C.K. Yen, L.W. Lin, J.C. Huang, C.A. Ke, Crystallization and mechanical behavior of the ferroelectric polymer nonwoven fiber fabrics for highly durable wearable sensor applications, Applied Surface Science, Volume 346, 15 August 2015, Pages 291-301, ISSN 0169-4332.

[11] Alexander Aman, Soeren Majcherek, Marc-Peter Schmidt, Soeren Hirsch, Microwave Sensor for Mechanical Stress Measurement Based on Ferroelectric Graphene Nanosheet Composites, Procedia Engineering, Volume 87, 2014, Pages 124-127, ISSN 1877-7058.

[12] Lionel Cima, Denis Remiens, Ferroelectric active sensors, Sensors and Actuators A: Physical, Volume 119, Issue 1, 28 March 2005, Pages 120-127, ISSN 0924-4247.

[13] Seung Tae Choi, Jong Oh Kwon, François Bauer, Multilayered relaxor ferroelectric polymer actuators for low-voltage operation fabricated with an adhesion-mediated film transfer technique, Sensors and Actuators A: Physical, Volume 203, 1 December 2013, Pages 282-290, ISSN 0924-4247.

[14] Uri Kushnir, Oded Rabinovitch, Advanced piezoelectric–ferroelectric stack actuator, Sensors and Actuators A: Physical, Volume 150, Issue 1, 16 March 2009, Pages 102-109, ISSN 0924-4247.

[15] K.P. Jayachandran, J.M. Guedes, H.C. Rodrigues, Ferroelectric materials for piezoelectric actuators by optimal design, Acta Materialia, Volume 59, Issue 10, June 2011, Pages 3770-3778, ISSN 1359-6454.

[16] Y. Corredores, A. Le Febvrier, X. Castel, R. Sauleau, R. Benzerga, S. Députier, M. Guilloux-Viry, A. Mekadmini, N. Martin, G. Tanné, Study of ferroelectric/dielectric multilayers for tunable stub resonator applications at microwaves, Thin Solid Films, Volume 553, 28 February 2014, Pages 109-113, ISSN 0040-6090.

[17] Su Sheng, Xiu-Zhang Wang, Hong-Ri Liu, Chao Jiang, C.K. Ong, Design of a hybrid ferroelectric thin film varactor for tunable microwave applications, Thin Solid Films, Volume 585, 30 June 2015, Pages 1-4, ISSN 0040-6090.

[18] M. Pilossof, M. Einat, Lifetime extension of ferroelectric cathodes for microwave tubes, Nuclear Instruments and Methods in Physics Research Section A: Accelerators, Spectrometers, Detectors and Associated Equipment, Volume 636, Issue 1, 21 April 2011, Pages 8-12, ISSN 0168-9002.

[19] Aharon J. Agranat, Lavi Secundo, Noam Golshani, Meir Razvag, Wavelength-selective photonic switching in paraelectric potassium lithium tantalate niobate, Optical Materials, Volume 18, Issue 1, October 2001, Pages 195-197, ISSN 0925-3467.

[20] Feng Ji, Baigang Zhang, Enbang Li, Haifeng Li, Rui Zhou, Tieli Zhang, Peng Wang, Jianquan Yao, Theoretical study of the electro-optic effect of aperiodically poled lithium niobate in a Q-switched dual-wavelength laser, Optics Communications, Volume 262, Issue 2, 15 June 2006, Pages 234-237, ISSN 0030-4018.

[21] Tomiki Ikeda, Osamu Tsutsumi, Takeo Sasaki, Liquid crystal photonics: optical switching and image storage by means of nematic liquid crystals and ferroelectric liquid crystals, Synthetic Metals, Volume 81, Issues 2–3, 15 August 1996, Pages 289-296, ISSN 0379-6779.

[22] De-Gui Sun, Zhifu Liu, Yingyan Huang, Seng-Tiong Ho, David J. Towner, Bruce W. Wessels, Performance simulation for ferroelectric thin-film based waveguide electro-optic modulators, Optics Communications, Volume 255, Issues 4–6, 15 November 2005, Pages 319-330, ISSN 0030-4018.

[23] Zhai Jiwei, Yao Xi, Zhang Liangying, The optical waveguide characteristics of highly orientated sol–gel derived polycrystalline ferroelectric PZT thin films, Ceramics International, Volume 27, Issue 5, 2001, Pages 585-589, ISSN 0272-8842.

[24] F. Caccavale, C. Sada, F. Segato, Yu.N. Korkishko, V.A. Fedorov, T.V. Morozova, Active waveguides in ferroelectric crystals by ion exchange, Journal of Non-Crystalline Solids, Volume 245, Issues 1–3, 1 April 1999, Pages 135-140, ISSN 0022-3093.

[25] Yongmin. Lee, J. Gourlay, W.J. Hossack, I. Underwood, A.J. Walton, Modelling of binary phase modulation in surface stabilized ferroelectric liquid crystal spatial light modulators, Microelectronics Journal, Volume 35, Issue 2, February 2004, Pages 193-201, ISSN 0026-2692.

[26] J.P Sharpe, N Sungar, N Macaria, Observation of stochastic resonance using an optically addressed amorphous silicon/ferroelectric liquid crystal spatial light modulator, Optics Communications, Volume 114, Issues 1–2, 15 January 1995, Pages 25-29, ISSN 0030-4018.

[27] T.D. Wilkinson, D.C. O'Brien, R.J. Mears, Dynamic asymmetric binary holograms using a ferroelectric liquid crystal spatial light modulator, Optics Communications, Volume 109, Issues 3–4, 1 July 1994, Pages 222-226, ISSN 0030-4018.

[28] F. Yakuphanoglu, A. Tataroglu, Ahmed A. Al-Ghamdi, R.K. Gupta, Yusuf Al-Turki, Z. Serbetçi, Saad Bin Omran, Farid El-Tantawy, Ferroelectric $Bi_{3.25}La_{0.75}\omega O_{12}$ photodiode for solar cell applications, Solar Energy Materials and Solar Cells, Volume 133, February 2015, Pages 69-75, ISSN 0927-0248.

[29] Relva C Buchanan, Jie Huang, Pyroelectric and sensor properties of ferroelectric thin films for energy conversion, Journal of the European Ceramic Society, Volume 19, Issues 6–7, June 1999, Pages 1467-1471, ISSN 0955-2219.

[30] Michael Hoffmann, Uwe Schroeder, Christopher Künneth, Alfred Kersch, Sergej Starschich, Ulrich Böttger, Thomas Mikolajick, Ferroelectric phase transitions in nanoscale HfO_2 films enable giant pyroelectric energy conversion and highly efficient supercapacitors, Nano Energy, Volume 18, November 2015, Pages 154-164, ISSN 2211-2855.

[31] B. T. Matthias and J. P. Remeika, “Ferroelectricity in the Ilmenite Structure,” Phys. Rev. Physical Review, vol. 76, no. 12, pp. 1886–1887, 1949.

[32] R. S. Weis, T. K. Gaylord, "Lithium niobate: Summary of physical properties and crystal structure", Applied Physics A, August 1985, Volume 37, Issue 4, pp 191-203.

[33] Wen-Ching Shih, Tzyy-Long Wang, Li-Lun Hsu, Surface acoustic wave properties of aluminum oxide films on lithium niobate, Thin Solid Films, Volume 518, Issue 23, 30 September 2010, Pages 7143-7146, ISSN 0040-6090.

[34] D. E. Allen, B. Bertiger and W. Daily, A latent failure mechanism for surface acoustic wave components utilising lithium niobate: IEEE 18th Annual Proceedings, Reliability Physics 1980, Las Vegas, Nevada, p.213 (1980), Microelectronics Journal, Volume 13, Issue 1, January–February 1982, Page 42, ISSN 0026-2692.

[35] Collins, J.H. et al, High-performance lithium niobate acoustic surface wave transducers and delay lines: Applied Physics Letters, Vol 13, No 9 (1 November 1968) p 312 (976), Ultrasonics, Volume 7, Issue 2, April 1969, Page 140, ISSN 0041-624X.

[36] Abbas Mohimi, Tat-Hean Gan, Wamadeva Balachandran, Development of high temperature ultrasonic guided wave transducer for continuous in service monitoring of steam lines using non-stoichiometric lithium niobate piezoelectric ceramic, Sensors and Actuators A: Physical, Volume 216, 1 September 2014, Pages 432-442, ISSN 0924-4247.

[37] Gunnar Arvidsson, Fredrik Laurell, Non-linear optical wavelength conversion in Ti:LiNbO3 waveguides, Thin Solid Films, Volume 136, Issue 1, 1986, Pages 29-36, ISSN 0040-6090.

[38] Junqiang Sun, Hong Li, Yongshan Cheng, Jianglin Li, Tunable wavelength conversion of picosecond pulses based on cascaded sum- and difference-frequency generation in quasi-phase-matched $LiNbO_3$ waveguides, Optics Communications, Volume 281, Issue 23, 1 December 2008, Pages 5874-5883, ISSN 0030-4018.

[39] Chun Wang, Dissertation, Carnegie Mellon University, 2007.

[40] Smith, G. L., Pulskamp, J. S., Sanchez, L. M., Potrepka, D. M., Proie, R. M., Ivanov, T. G., Rudy, R. Q., Nothwang, W. D., Bedair, S. S., Meyer, C. D. and Polcawich, R. G. (2012), J. Am. Ceram. Soc., 95: 1777–1792.

[41] Dal-Hyun Do, Dissertation, UNIVERSITY OF WISCONSIN-MADISON, 2006

[42] Reza Moazzami, Chenminh Hu, William H. Shepherd, IEEE Transactions on Electron Devices, Vol. 39, No. 9, 1992.

[43] Kang, Tae Dong and Xiao, Bo and Avrutin, Vitaliy and Özgür, Ümit and Morkoç, Hadis and Park, Jun Woo and Lee, Ho Suk and Lee, Hosun and Wang, Xiaoyu and Smith, David. J., Journal of Applied Physics, 104, 093103 (2008).

[44] Fu-Ping Zhang, Jin-Mei Du, Yu-Sheng Liu, and Hong-Liang Hew, J. Am. Ceram. Soc., 90 [8] 2639–2641 (2007).

[45] Javad Gatabi, Kevin Lyon, Shafiqur Rahman, Manuel Caro, Juan Rojas-Ramirez, Joelson Cott-Garcia, Ravi Droopad, Byounghak Lee, Microelectronic Engineering, Volume 147, 1 November 2015, Pages 117-121.

[46] Skrobis K. J., Denton D. D., Skrobis A. V., Effect of early solvent evaporation on the mechanism of the spin-coating of polymeric solutions. Polym Eng Sci, 30: 193–196, 1990.

[47] Andreas Munch, Colin P. Please, Barbara Wagner, Spin coating of an evaporating polymer solution, PHYSICS OF FLUIDS 23, 2011.

[48] Niranjan Sahu, B Parija, S Panigarahi, Fundamental understanding and modeling of spin coating, Indian J. Phys. 83 (4) 493-502, 2009.

[49] Douglas B. Chrisey, Graham K. Hubler, Pulsed Laser Deposition of Thin Films, Wiley-Interscience, 1 edition, 1994.

[50] Nishida, T., Echizen, M., Gun, B., Kono, T., Tsuchikawa, T., Uchiyama, K., and Shiosaki, T.: 'Analysis of frequency conversion devices incorporating (Ba, Sr)TiO_3 nonlinear dielectric films', Institute of Electrical and Electronics Engineers Inc., 2007, pp. 193-194.

[51] Victor, A., Nath, J., Ghosh, D., Boyette, B., Maria, J.P., Steer, M.B., Kingon, A.I., and Stauf, G.T.: 'A voltage controlled oscillator using barium strontium titanate (BST) thin film varactor', 'Book A voltage controlled oscillator using barium strontium titanate (BST) thin film varactor' (IEEE, 2004), pp. 91-94.

[52] Kalkur, T.S., Jamil, A., and Cramer, N.: ‘Characteristics of voltage controlled oscillators implemented with tunable ferroelectric high-k capacitors’, in Editor (Ed.)^(Eds.): ‘Book Characteristics of voltage controlled oscillators implemented with tunable ferroelectric high-k capacitors’ (IEEE, 2007, edn.), pp. 364-367.

[53] Zhang, Y., and Kalkur, T.S.: ‘Adaptive RF power amplifier tuned with ferroelectric BST varactor’: ‘Book Adaptive RF power amplifier tuned with ferroelectric BST varactor’ (Electromagnetics Academy, 2011, pp. 999-1002.

[54] Ali, F., Gloeckler, R., Weigel, R., and Fischer, G.: ‘Efficiency enhancement of a tunable RF power amplifier by second harmonic manipulation using thin-film BST varactor’: ‘Book Efficiency enhancement of a tunable RF power amplifier by second harmonic manipulation using thin-film BST varactor’ (Institute of Electrical and Electronics Engineers Inc., 2010, pp. 434-436.

[55] Feng, Z., Fathelbab, W.M., Lam, P.G., Haridasan, V., Maria, J.-P., Kingon, A.I., and Steer, M.B.: ‘Narrowband Barium Strontium Titanate (BST) tunable bandpass filters at X-band’: ‘Book Narrowband Barium Strontium Titanate (BST) tunable bandpass filters at X-band’ (Institute of Electrical and Electronics Engineers Inc., 2009, edn.), pp. 1061-1064.

[56] Park, J.D., Sung, Y.J., Lee, S.H., and Kim, Y.S.: ‘Tunable bandstop filters using defected ground structure with active devices’: ‘Book Tunable bandstop filters using defected ground structure with active devices’ (IEEE, 2006, edn.), pp. 3.

[57] Chun, Y.-H., Hong, J.-S., Bao, P., Jackson, T.J., and Lancaster, M.J.: ‘BST-varactor tunable dual-mode filter using variable ZC transmission line’, IEEE Microwave and Wireless Components Letters, 2008, 18, (3), pp. 167-169.

[58] Mahmud, A., Kalkur, T.S., Jamil, A., and Cramer, N.: ‘A 1-GHz active phase shifter with a ferroelectric varactor’, IEEE Microwave and Wireless Components Letters, 2006, 16, (5), pp. 261-263.

[59] Kim, K.B., Yun, T.S., Lee, J.C., Chaker, M., Park, C.S., and Wu, K.: 'Integration of microwave phase shifter with BST varactor onto TiO_2/Si wafer', Electronics Letters, 2007, 43, (14), pp. 757-759.

[60] Pan, K.C., Jiang, H., Brown, D., Zhang, C.H., Patterson, M., and Subramanyam, G.: 'Frequency tuning of CPW bowtie antenna by ferroelectric BST thin film varactors': 'Book Frequency tuning of CPW bowtie antenna by ferroelectric BST thin film varactors' (Institute of Electrical and Electronics Engineers Inc., 2011, edn.), pp. 1-4.

[61] Cure, D., Weller, T.M., Price, T., Miranda, F.A., and Van Keuls, F.W.: 'Low-Profile Tunable Dipole Antenna Using Barium Strontium Titanate Varactors', IEEE Transactions on Antennas and Propagation, 2014, 62, (3), pp. 1185-1193.

[62] Scheele, P., Goelden, F., Giere, A., Mueller, S., and Jakoby, R.: 'Continuously tunable impedance matching network using ferroelectric varactors': 'Book Continuously tunable impedance matching network using ferroelectric varactors' (Institute of Electrical and Electronics Engineers Inc., 2005, edn.), pp. 603-606.

[63] Gonzalez-Rodriguez, E., Maune, H., Yuliang, Z., Lufei, S., Shah, I.A., Hofmann, K., Dahlhaus, D., and Jakoby, R.: 'Impact of group delay on tunable impedance matching networks based on Barium-Strontium-Titanate varactors': 'Book Impact of group delay on tunable impedance matching networks based on Barium-Strontium-Titanate varactors' (IEEE, 2012, edn.), pp. 5.

[64] Boser, O., and Newsome, V.: 'HIGH FREQUENCY BEHAVIOR OF CERAMIC MULTILAYER CAPACITORS', IEEE transactions on components, hybrids, and manufacturing technology, 1986, CHMT-10, (3), pp. 437-439.

[65] F. Li, M. K. Balazs, and S. Anderson, "Effects of Ambient and Dissolved Oxygen Concentration in Ultrapure Water on Initial Growth of Native Oxide on a Silicon (100) Surface," Journal of The Electrochemical Society J. Electrochem. Soc., vol. 152, no. 8, 2005.

[66] Simoes, A.Z., Zaghete, M.A., Stojanovic, B.D., Gonzalez, A.H., Riccardi, C.S., Cantoni, M., Varela, J.A.; Journal of the European Ceramic Society, Vol. 24, No. 6, 2004, pp. 1607–1613.

[67] X. Chen, "Crystallization characteristics of $LiNbO_3$ derived from sol-gel," J Mater Sci: Mater Electron Journal of Materials Science: Materials in Electronics, vol. 7, no. 1, 1996.

[68] V. Joshi, D. Roy, and M. L. Mecartney, "Low temperature synthesis and properties of lithium niobate thin films," Appl. Phys. Lett. Applied Physics Letters, vol. 63, no. 10, p. 1331, 1993.

[69] Cagin, E.: 'Integration of Functional Oxides With The Semiconductor Zinc Oxide', University of Michigan, 2010.

[70] V. S. Saji and H. C. Choe, "Chemical solution deposition of $CaCu_3Ti_4O_{12}$ thin film," Bulletin of Materials Science Bull Mater Sci, vol. 33, no. 3, pp. 203–207, 2010.

[71] Xinhua Huang, Yong Jiang, Kan Wu, "CCTO Giant Dielectric Ceramic Prepared by Reaction Sintering", The 7th World Congress on Particle Technology (WCPT7), Procedia Engineering 102 (2015) 468 – 474.

[72] Rainer Schmidt, Martin C. Stennett, Neil C. Hyatt, Jan Pokorny, Jesús Prado-Gonjal, Ming Li, Derek C. Sinclair, "Effects of sintering temperature on the internal barrier layer capacitor (IBLC) structure in $CaCu_3Ti_4O_{12}$ (CCTO) ceramics", Journal of the European Ceramic Society 32 (2012) 3313–3323.

[73] Lei Li, Zhi Wei Wang, Xiang Ming Chen, "Effects of sintering temperature and annealing atmosphere on microwave dielectric properties of $CaCu_3Ti_4O_{12}$, $Ba(Fe_{1/2}Nb_{1/2})O_3$ and $Sr(Fe_{1/2}Nb_{1/2})O_3$ ceramics", Materials Research Bulletin 67 (2015) 251–254.

[74] Rong Yu, Hao Xue, Zeliang Cao, La Chen, Zhaoxian Xiong, "Effect of oxygen sintering atmosphere on the electrical behavior of CCTO ceramics", Journal of the European Ceramic Society 32 (2012) 1245–1249.

[75] Pei Liu, Yuanming Lai, Yiming Zeng, Shuang Wu, Zihan Huang, Jiao Han, "Influence of sintering conditions on microstructure and electrical properties of $CaCu_3Ti_4O_{12}$ (CCTO) ceramics", Journal of Alloys and Compounds 650 (2015) 59e64.

[76] Zhi Yang, Yue Zhang, Rui Xiong, Jing Shi, "Effect of sintering in oxygen on electrical conduction and dielectric properties in $CaCu_3Ti_4O_{12}$", Materials Research Bulletin 48 (2013) 310–314.

[77] I. Norezan, A.K. Yahya and M.K. Talari, "Effect of $(Ba_{0.6}Sr_{0.4})TiO_3$ (BST) Doping on Dielectric Properties of CaCu3Ti4O12 (CCTO)", J. Mater. Sci. Technol., 2012, 28(12), 1137–1144.

[78] F. Amaral, M.A. Valente, L.C. Costa, "Dielectric properties of $CaCu_3Ti_4O_{12}$ (CCTO) doped with GeO_2", Journal of Non-Crystalline Solids 356 (2010) 822–827.

[79] Sudipta Goswami, A. Sen, "Low temperature sintering of CCTO using P_2O_5 as a sintering aid", Ceramics International 36 (2010) 1629–1631.

[80] L.M. Jesus, J.C.A. Santos, D.V. Sampaio, L.B. Barbosa, R.S. Silva, J.-C. M'Peko, "Polymeric synthesis and conventional versus laser sintering of $CaCu_3Ti_4O_{12}$ electroceramics: (micro)structures, phase development and dielectric properties, Journal of Alloys and Compounds 654 (2016) 482e490.

[81] Ranjit Kumar, M. Zulfequar, V.N. Singh, J.S. Tawale, T.D. Senguttuvan, "Microwave sintering of dielectric $CaCu_3Ti_4O_{12}$: An interfacial conductance and dipole relaxation effect", Journal of Alloys and Compounds 541 (2012) 428–432.

[82] Sabar D. Hutagalung, M. Ikhwan M. Ibrahim, Zainal A. Ahmad, "Microwave assisted sintering of $CaCu_3Ti_4O_{12}$", Ceramics International 34 (2008) 939–942.

[83] C. Masingboon, T. Eknapakul, S. Suwanwong, P. Buaphet, H. Nakajima, S.-K. Mo, P. Thongbai, P. D. C. King, S. Maensiri, and W. Meevasana, "Anomalous change in dielectric constant of $CaCu_3Ti_4O_{12}$ under violet-to-ultraviolet", Applied Physics Letters 102, 202903 (2013).

[84] Liang Fang, Mingrong Shen, "Effects of postanneal conditions on the dielectric properties of $CaCu_3Ti_4O_{12}$ thin films prepared on Pt/Ti/SiO_2/Si substrates", JOURNAL OF APPLIED PHYSICS VOLUME 95, NUMBER 11, 1 JUNE 2004.

[85] SUNG-YOON CHUNG1, IL-DOO KIM2 AND SUK-JOONG L. KANG3, "Strong nonlinear current–voltage behaviour in perovskite-derivative calcium copper titanate", nature materials, VOL 3, 2004.

[86] Yang Sun, "DIELECTRIC PROPERTIES OF $CaCu_3Ti_4O_{12}$ AND ITS RELATED MATERIALS", Thesis, University of Akron, 2006.

[87] Sanjesh Babu, Anil Govindan, "Dielectric Properties of $CaCu_3Ti_4O_{12}$ (CCTO) Prepared by Modified Solid State Reaction Method", International Review of Applied Engineering Research, Volume 4, Number 3 (2014), pp. 275-280.

[88] Chen Kai, Li Wei, Liu Yun Fei, Bao Peng, Lu Xiao Mei, ZHU Jin Song, Investigation of the size effect on the giant dielectric constant of $CaCu_3Ti_4O_{12}$ Ceramic, Chin. Phys. Lett., Vol. 21, No. 9, 2004.

[89] Arun Chamola, Hemant Singh, U.C. Naithani, Shubhash Sharma, Uday Prabhat, Pratiksha Devi, Anuradha Malik, Alok Srivastava, R.K. Sharma, "Structural, dielectric and electrical properties of Lead zirconate titanate and CaCu3Ti4O12 ceramic composite", Adv. Mat. Lett. 2011, 2(1), 26-31.

[90] Devendra P. Singha, Y.N. Mohapatraa, D.C. Agrawal, "Dielectric and leakage current properties of sol–gel derived calcium copper titanate (CCTO) thin films and CCTO/ZrO_2 multilayers", Materials Science and Engineering B 157 (2009) 58–65.

[91] Swati Shandilya, Monika Tomar, K. Sreenivas, and Vinay Gupta, "Purely hopping conduction in c-axis oriented $LiNbO_3$ thin films", JOURNAL OF APPLIED PHYSICS 105, 094105 2009.

[92] VINAY GUPTA, MONIKA TOMAR, P. BHATTACHARYA, K. SREENIVAS, R. S. KATIYAR, "The AC Conductivity and Dielectric Constant of (006) Textured LiNbO3 Films", Ferroelectric Letters, 32:125–130, 2005.

[93] Abhai Mansingh, Ajay Dhar, The AC conductivity and dielectric constanoft lithium niobate single crystals, J. Phys. D: Appl. Phys. l8 (1985) 2059-2071.

[94] B. S. Umarov, J. F. Vetelino, "Temperature dependence of the dielectric constant and I. R. reflection spectrum of $LiNbO_3$ by raman scattering", Solid State Communications, Vol. 36, pp. 465-468.

[95] Makram A. Fakhri, Y. Al-Douri, U. Hashim, Evan T. Salim, "Optical investigations of photonics lithium niobate", Solar Energy 120 (2015) 381–388.

[96] Ravi Droopad, Zhiyi Yu, Hao Li, Yong Liang, Corey Overgaard, Alex Demkov, Xiaodong Zhang, Karen Moore, Kurt Eisenbeiser, Mike Hu, Jay Curless, Jeff Finder, Development of integrated heterostructures on silicon by MBE, Journal of Crystal Growth, Volume 251, Issues 1–4, April 2003, Pages 638-644.

[97] Lixin Feng, Youwen Wang, Yueyue Yan, Guanghan Cao, Zhengkuan Jiao, "Growth of highly-oriented $CaCu_3Ti_4O_{12}$ thin films on $SrTiO_3$ (1 0 0) substrates by a chemical solution route", Applied Surface Science 253 (2006) 2268–2271.

[98] W. Si, E. M. Cruz, P. D. Johnson, P. W. Barnes, P. Woodward, and A. P. Ramirez, "Epitaxial thin films of the giant-dielectric-constant material $CaCu_3Ti_4O_{12}$ grown by pulsed-laser deposition", Applied Physics Letters 81, 2056 (2002).

[99] Y. Lin, Y. B. Chen, T. Garret, S. W. Liu, C. L. Chen, L. Chen, R. P. Bontchev, A. Jacobson, J. C. Jiang, E. I. Meletis, J. Horwitz, and H.-D. Wu, "Epitaxial growth of dielectric $CaCu_3Ti_4O_{12}$ thin films on (001) $LaAlO_3$ by pulsed laser deposition", Applied Physics Letters 81, 631 (2002).

[100] Kyuho Choy Naijuan Wu, Alex Ignatiev, "Dielectric Properties of $CaCu_3Ti_4O_{12}$ thin Films", 2002 IEEE.

[101] Y.L. Zhaoa, G.W. Pana, Q.B. Rena, Y.G. Caoa, L.X. Fenga, Z.K. Jiao, "High dielectric constant in $CaCu_3Ti_4O_{12}$ thin film prepared by pulsed laser deposition", Thin Solid Films 445 (2003) 7–13.

[102] M. Golalikhani, Q. Y. Lei, G. Chen, J. E. Spanier, H. Ghassemi, C. L. Johnson, M. L. Taheri, and X. X. Xi, "Stoichiometry of $LaAlO_3$ films grown on $SrTiO_3$ by pulsed laser deposition", JOURNAL OF APPLIED PHYSICS 114, 027008 (2013).

[103] Stefan Patrick Thiel, "Study of Interface Properties in $LaAlO_3/SrTiO_3$ Heterostructures ", Dissertation, University at Augsburg, 2009.

[104] Hiroki Sato, "Growth control of the electronic properties of the $LaAlO_3/SrTiO_3$ heterointerface", Thesis, University of Tokyo, 2010.

[105] I. A. Petukhov, A. N. Shatokhin, F. N. Putilin, M. N. Rumyantseva, V. F. Kozlovskii, A. M. Gaskov, D. A. Zuev, A. A. Lotin, O. A. Novodvorsky, and A. D. Khramova, "Pulsed Laser Deposition of Conductive Indium Tin Oxide Thin Films", Neorganicheskie Materialy, 2012, Vol. 48, No. 10, pp. 1147–1153.

[106] Kyurin Kim, Jun Hyuk Park, Hyunsoo Kim, Jong Kyu Kim, E. Fred Schubert, and Jaehee Cho, "Energy bandgap variation in oblique angle-deposited indium tin oxide", Applied Physics Letters 108, 041910 (2016).

[107] Zhou Xu, Peng Chen, Zhenlong Wu, Feng Xua, Guofeng Yang, Bin Liu, Chongbin Tan, Lin Zhang, Rong Zhang, Youdou Zheng, "Influence of thermal annealing on electrical and optical properties of indium tin oxide thin films", Materials Science in Semiconductor Processing, 26, 2014, 588-592.

[108] J.H. Park, C. Buurma, S. Sivananthan, R. Kodama, W. Gao, T.A. Gessert, "The effect of post-annealing on Indium Tin Oxide thin films bymagnetron sputtering method", Applied Surface Science 307 (2014) 388–392.

[109] P. Doggart, N. Bristow, and J. Kettle, "Optimisation of the material properties of indium tin oxide layers for use in organic photovoltaics", JOURNAL OF APPLIED PHYSICS 116, 103103 (2014).

[110] Brooks, K.G.; Kohli, M.; Taylor, D.V.; Maeder, T.; Reaney, I.; Kholkin, A.; Muralt, P.; Setter, N., in Applications of Ferroelectrics, 1996. ISAF '96., Proceedings of the Tenth IEEE International Symposium on, vol.2, no., pp.611-614 vol.2, 18-21.

[111] Brian Leclerc, Dissertation, Queen's University, 1999.

[112] IAN M. REANEY, DAVID V. TAYLOR, KEITH G. BROOKS, Journal of Sol-Gel Science and Technology 13, 813–820 (1998).

[113] T G Cooney and L F Francis, J. Micromech. Microeng. 6 (1996) 291–300.

[114] Stephen P. Bathurst, Thesis, MASSACHUSETTS INSTITUTE OF TECHNOLOGY, 2012.

[115] Yutaka Kokaze, Isao Kimura, Takehito Jimbo, Mitsuhiro Endo, Masahisa Ueda, Koukou Suu, ULVAC Tecjnical Journal, No 66E, 2007.

[116] Cui Yan, Yao Minglei, Zhang Qunying, Chen Xiaolong, Chu Jinkui, and Guan Le, International Journal of Polymer Science, Volume 2014, Article ID 574684.

[117] K.Yamakawa, O.Arisumi, K.Okuwada, K.Tsutsumi, T.Katata, in Applications of Ferroelectrics, 1998. ISAF 98. Proceedings of the Eleventh IEEE International Symposium on, pp.159-162, 1998.

[118] CHUNG-CHENG CHANG, JUNG-HUA WANG, MU-DER JENG, CHEN-CHOU LIN, KAU-HSIUNG CHEN, Proc. Natl. Sci. Counc. ROC(A), Vol. 24, No. 4, 2000. pp. 287-292.

[119] S. R. Gilbert, S. Hunter, D. Ritchey, C. Chi, D. V. Taylor, J. Amano, S. Aggarwal, T. S. Moise, T. Sakoda, S. R., Summerfelt, K. K. Singh, C. Kazemi, D. Carl, B. Bierman, Journal of Applied Physics 93, 1713 (2003).

[120] H. R. Kim, S. Jeong, C. B. Jeon, O. S. Kwon, C. S. Hwang, Y. K. Han, D. Y. Yang, and K. Y. Oh, "Metalorganic chemical vapor deposition of very thin $Pb(Zr,Ti)O_3$ thin films at low temperatures for high-density ferroelectric memory applications," Journal of Materials Research J. Mater. Res., vol. 16, no. 12, pp. 3583–3591, 2001.

[121] W. G. Lee and Y. J. Kwon, "Preparation of ferroelectric PZT thin films by plasma enhanced chemical vapor deposition using metalorganic precursors," Journal of Industrial and Engineering Chemistry, vol. 14, no. 1, pp. 89–93, 2008.

[122] C. S. Hwang and H. J. Kim, “Deposition of Pb(Zr,Ti)O3 Thin Films by Metal-Organic Chemical Vapor Deposition Using β-diketonate Precursors at Low Temperatures,” Journal of the American Ceramic Society, vol. 78, no. 2, pp. 329–336, 1995.

[123] P. Verardi, F. Craciun, and M. Dinescu, “Characterization of PZT thin film transducers obtained by pulsed laser deposition,” 1997 IEEE Ultrasonics Symposium Proceedings. An International Symposium (Cat. No.97CH36118).

[124] R. Wang, H. Kokawa, R. Maeda, DTIP 2006, Apr 2006, Stresa, Lago Maggiore, Italy.

[125] P. Verardi, M. Dinescu, and F. Craciun, “Pulsed laser deposition and characterization of PZT thin films,” Applied Surface Science, vol. 154-155, pp. 514–518, 2000.

[126] A. Zomorrodian, A. Messarwi, and N. Wu, “AES and XPS study of PZT thin film deposition by the laser ablation technique,” Ceramics International, vol. 25, no. 2, pp. 137–140, 1999.

[127] N. Shohata, S. Matsubara, Y. Miyasaka, and M. Yonezawa, “Epitaxial Growth of PbTiO3on MgAl2O4/Si Substrates,” Sixth IEEE International Symposium on Applications of Ferroelectrics, 1986.

[128] T. Dhakal, D. Mukherjee, R. H. Hyde, H. Srikanth, P. Mukherjee, and S. Witanachchi, “Enhancement in Ferroelectricity in V-Doped ZnO Thin Film Grown using Laser Ablation,” MRS Proc. MRS Proceedings, vol. 1199, 2009.

[129] Devajyoti Mukherjee, Dissertation, University of South Florida, 2010.

[130] Shintaro Yokoyama, Yoshihisa Honda, Hitoshi Morioka, Shoji Okamoto, Hiroshi Funakubo, Takashi Iijima, Hirofumi Matsuda, Keisuke Saito, Takashi Yamamoto, Hirotake Okino, Osami Sakata, Shigeru Kimura, Journal of Applied Physics 98, 094106 (2005).

[131] C.M. Lonkar, D.K. Kharat, H.H. Kumar, Sahab Prasad, Mrinal Ghosh, C.S. Kumbhar, Ceramics International 37 (2011) 3509–3514.

[132] Smith, S.M., Talin, A.A., Voight, S., Hooper, A., and Convey, D.: 'Effect of annealing temperature on physical properties of thin epitaxial PZT films on STO/Si substrates': 'Book Effect of annealing temperature on physical properties of thin epitaxial PZT films on STO/Si substrates' (SPIE-Int. Soc. Opt. Eng., 2002, edn.), pp. 1-8.

[133] S Arscotty, N Smithy, R Kurchaniaz, S J Milnez and R E Milesy; Sol–gel derived $Pb(Zr,Ti)O_3$ thin films on GaAs, Semicond. Sci. Technol. 13 (1998) 244–248.

[134] Kim, S.H., Kim, C.E., and Oh, Y.J.: 'Influence of Al_2O_3 diffusion barrier and $PbTiO_3$ seed layer on microstructural and ferroelectric characteristics of PZT thin films by sol-gel spin coating method', Thin Solid Films, 1997, 305, (1-2), pp. 321-326.

[135] Asif Islam Khan, Debanjan Bhowmik, Pu Yu, Sung Joo Kim, Xiaoqing Pan:

'Experimental evidence of ferroelectric negative capacitance in nanoscale

Heterostructures', Appl. Phys. Lett. 99, 113501 (2011); doi: 10.1063/1.3634072.